1-1-2019

Experimental and Numerical Study of a Synthetic Jet Ejector

Ziad Alaswad
University of Windsor

Experimental and Numerical Study of a Synthetic Jet Ejector

By

Ziad Alaswad

A Thesis
Submitted to the Faculty of Graduate Studies
through the Department of Mechanical, Automotive, and Materials Engineering
in Partial Fulfillment of the Requirements for
the Degree of Master of Applied Sciences
at the University of Windsor

Windsor, Ontario, Canada

2019

Experimental and Numerical Study of a Synthetic Jet Ejector

by

Ziad Alaswad

APPROVED BY:

_____

R. Balachandar
Department of Civil and Environmental Engineering

_____

A. Fartaj
Department of Mechanical, Automotive and Materials Engineering

_____

V. Roussinova, Co-Advisor
Department of Mechanical, Automotive and Materials Engineering

_____

G. Rankin, Co-Advisor
Department of Mechanical, Automotive and Materials Engineering

June 20, 2019

DECLARATION OF ORIGINALITY

I hereby certify that I am the sole author of this thesis and that no part of this thesis has been published or submitted for publication.

I certify that, to the best of my knowledge, my thesis does not infringe upon anyone's copyright nor violate any proprietary rights and that any ideas, techniques, quotations, or any other material from the work of other people included in my thesis, published or otherwise, are fully acknowledged in accordance with the standard referencing practices. Furthermore, to the extent that I have included copyrighted material that surpasses the bounds of fair dealing within the meaning of the Canada Copyright Act, I certify that I have obtained a written permission from the copyright owner(s) to include such material(s) in my thesis and have included copies of such copyright clearances to my appendix.

I declare that this is a true copy of my thesis, including any final revisions, as approved by my thesis committee and the Graduate Studies office, and that this thesis has not been submitted for a higher degree to any other University or Institution.

ABSTRACT

A traditional synthetic jet ejector is a combination of synthetic jet and mixing tube or shroud in which flow from the surroundings is entrained through the space between the jet and shroud and discharged from the end of a mixing tube. An objective of the current research is to evaluate the accuracy of a previous simplified numerical model using results from an improved numerical model and an experimental synthetic jet ejector water flow facility. The improved model gives a better representation of the primary jet velocity profile by accurately modeling the piston motion using the dynamic mesh option. Also, flow approaching the secondary inlet plane is considered in the new model by including the surrounding fluid in the solution domain. The model is used to show the shortcomings of certain assumptions made in the simplified model.

Experimentally, the phase-averaged velocity field within the shroud is determined using Particle Image Velocimetry. It is shown that the improved numerical model gives a more accurate prediction of the variation of phase-averaged volume flow rate throughout the cycle and the cycle averaged values than the previous simplified model. Also, the numerical and phase-averaged experimental flow field patterns show some similarities however, certain details of the profiles are quite different. Extremely high turbulence level or intense mixing is detected near the exit of the synthetic jet. This is thought to be responsible for the shorter flow development noticed in the experiments compared with the numerical solution.

DEDICATION

To

My Motherland, Palestine,

where I am still dreaming to visit,

and

to the most precious thing in my life,

my parents & my siblings

ACKNOWLEDGEMENTS

I am indebted to my supervisors, Dr. Gary Rankin and Dr. Vesselina Roussinova, for their distinguishing supervision and support. At many stages in the course of this research project I benefited from their suggestions and guidance, particularly so when exploring new ideas. Their positive outlook and confidence in my research inspired me and gave me confidence. Their careful editing contributed enormously to the production of this thesis.

A project of this nature, based on two different methods, is only possible with the help of many people. They too have played their part in the development of the study.

I would like to send my regards to my committee members, Dr. Ram Balachandar and Dr. Amir Fartaj, for their helpful suggestions and valuable time to review my thesis. A special thanks to Dr. Balachandar who gave me the chance to use his PIV equipment. I also would like to extend my thanks to Dr. Biswas for acting as the chair of my defence.

Special thanks go to Mr. Ken Ternoey for sponsoring and funding the construction process of the SJE. Furthermore, I would like to acknowledge and thank all technicians, especially Andrew Jenner, Bruce Durfy, Dean Poublon, Ram Barakat, Kevin Harkai and Matthew St. Louis, who helped me in learning to use the workshop machines and in developing my manufacturing and designing skills.

I want also to thank my colleagues and friends, Sichang, Abdullah, Hussein, Bader, Liza and Anthony, who supported me mentally and who shared their knowledge with me during this unique and difficult chapter in my life. Heart-felt acknowledgement goes to Tim Horton's for endless medium double-double and 7/11 for their Red Bulls!

TABLE OF CONTENTS

LIST OF TABLES

LIST OF FIGURES

LIST OF ABBREVIATIONS/SYMBOLS

BC	Boundary Condition
BDC	Bottom Dead Centre
CAD	Computer-Aided Design
CCD	Charge-Coupled Device
CFD	Computational Fluid Dynamics
CPU	Central Processing Unit
CV	Control Volume
DCC	Direct Cross-Correlation
DFT	Discrete Fourier Transform
DNS	Direct Numerical Simulation
ECE	Energy Cooling Efficiency
FBD	Free Body Diagram
FEA	Finite Element Analysis
FFT	Fast Fourier Transform
FOV	Field of View
IA	Interrogation Area
ID	Inner Diameter
ITTC	International Towing Tank Conference
LES	Large Eddy Simulation
LDV	Laser Doppler Velocimetry
Nd:YAG	Neodym-Yttrium-Aluminum-Garnet
OD	Outer Diameter

PISO	Splitting of Operators Scheme
PIV	Particle Image Velocimetry
PIV-STD	PIV Standardization
PTFE	Polytetrafluoroethylene
QUICK	Quadratic Upstream Interpolation for Convective Kinetics
RAM	Random Access Memory
SJ	Synthetic Jet
SJA	Synthetic Jet Actuator
SJE	Synthetic Jet Ejector
SST	Shear Stress Transport
TDC	Top Dead Centre
TSI	Thermal System Inc.
TSPC	Time Steps Per Cycle
TTL	Transistor-Transistor Logic
UDF	User Defined Function
VDC	Volts Direct Current
VOF	Volume of Fluid
VSJ	Visualization Society of Japan
ZNMF	Zero-Net Mass Flux

NOMENCLATURE

a	Acceleration
A	Surface Area of the Piston
A_a	Amplitude Acceleration
A_P	Primary Inlet Area
A_S	Secondary Inlet Area
B	Bias Error
C_e	Entrainment Coefficient
d	Synthetic Jet Orifice Diameter
D	Synthetic Jet Actuator Diameter
DC	Direct Current
De	Synthetic Jet Ejector Shroud Diameter
D_T	Tank Diameter/Width
f	Synthetic Jet Piston Driving Frequency
F_P	Piston Force
F_R	Bearing Force
g	Gravitational Acceleration
G	Gap between the OD of the Cavity and the ID of the Shroud
h_1	Height from the Orifice Exit to the Free Surface
H	Height of Water in a Tank
k	Integer between 1 and n
K_L	Coefficient Loss

L_e	Shroud Length
L_o	Stroke Length
$L_o/_d$	Dimensionless Stroke Length
LIF	Laser-Induced Fluorescence
m	Mass
M_e	Entrained Mass Flow Rate Up to Position x
M_j	Jet Mass Flow Rate at the Orifice
$M_S/_{M_P}$	Pumping Effectiveness
$\Delta M_e/_{\Delta x}$	Entrainment Rate
n	Number of Timesteps Per Cycle
P	Pressure
ΔP	Pressure Difference
Q_i	Period-Averaged Inlet Volume Flow Rate
Q_o	Period-Averaged Outlet Volume Flow Rate
Q_P	Period-Averaged Primary Volume Flow Rate
Q_S	Period-Averaged Secondary Volume Flow Rate
R	Synthetic Jet Orifice Radius
$RANS$	Reynolds-Averaged Navier-Stokes
Re	Reynolds Number
R_S	Synthetic Jet Ejector Shroud Radius
R_T	Tank Radius
s	Displacement of Piston inside the Actuator

S	Stokes Number
S_a	Amplitude Piston Displacement
St	Strouhal Number
tt	Synthetic Jet Actuator Cavity Thickness
$t_{95\%}$	t Distribution Value at 95 % Confidence Level
t/T	Dimensionless Time
Δt	Time Interval between Two Image Pairs in PIV Calculations
T	Synthetic Jet Piston Driving Period
TT	Synthetic Jet Ejector Shroud Thickness
ΔT	Timestep Size
U_{rms}	RMS Axial Velocity
U	Mean Velocity
$\overline{U}$	Time Integral Velocity over One Period
U_o	Characteristic Velocity
V_A	Velocity Amplitude
V_p	Orifice Area-Average Velocity
ω	Angular Velocity
W	Weight
x	Axial Distance from the Orifice Exit Plane
Δx	Meshing Cell Height

Greek Letters

ρ	Water Density
ρ_j	Water Jet Density at the Orifice
ρ_s	Density of the Surrounding Atmosphere
μ	Water Dynamic Viscosity
ω	Turbulence Frequency
ϑ	Water Kinematic Viscosity
σ	Random Error
ε	Rate of Dissipation of Turbulence

Chapter 1

INTRODUCTION

In fluid dynamics, a jet is defined as a stream of fluid that is projected through an opening under pressure into a surrounding medium. Air that comes out of a hairdryer is considered to be a submerged jet because the jet fluid is the same as the surrounding medium. On the other hand, water that comes out of the garden hose to the surrounding air is considered to be a non-submerged jet [1]. Jets that have an exit exposed to the atmosphere are called free jets. Free jets may also be unsteady and not only used for mixing but for other purposes, such as producing thrust. For unsteady jets, mean velocity and pressure change with time, while they are constant with time for steady jets [2]. A special case of unsteady jets is called a pulsating jet [3]. Pulsating jets have periodic pulsations superimposed on the mean flow [4,5]. Constraining a jet by adding a shroud or a mixing tube creates a confined jet [6]. The jet ejector is considered a special case of a confined jet that can involve steady or pulsating jet. In this chapter, Synthetic Jets (SJs) and Synthetic Jet Ejectors (SJEs) will be defined as well as the motivation and the scope of the thesis.

1.1 Synthetic Jets (SJs)

A synthetic jet (SJ) is a special case of a pulsating jet with zero mean flow. They are produced by the periodic vortices formed by alternating momentary ejection and suction of fluid through an orifice on one side of a cavity whose volume is changed by means of an oscillating mechanism [7]. An oscillating diaphragm or a piston can be used for the fluid suction and ejection processes. The diaphragm can be oscillated mechanically

[8] or using a piezoelectric wafer [9], and the jet flow is observed to become steady a short distance downstream of the orifice exit.

A Synthetic Jet Actuator (SJA) is a fluidic device that is used to produce synthetic jets. The SJA includes three main parts: chamber or cavity, orifice and an oscillating driver as shown in Figure 1.1. The movement of the oscillating driver causes the fluid to be periodically entrained into and then expelled from the chamber through the orifice to the atmosphere. Vortex rings can be generated around the orifice during the ejection phase of the cycle, under certain operating conditions, as illustrated by Holman et al. [10], and travel downstream from the orifice exit. The interaction of those vortex rings generates the SJ. The self-induced velocity of the vortex ring and its distance away from the actuator's orifice control the degree of interaction between the vortex and the reversed flow through the orifice, caused by the suction of the surrounding fluid [11]. Thus, the vortex ring will die out during the suction phase if its self-induced velocity is not high enough to move it away from the orifice exit. The jet flow becomes steady a short distance downstream of the orifice exit.

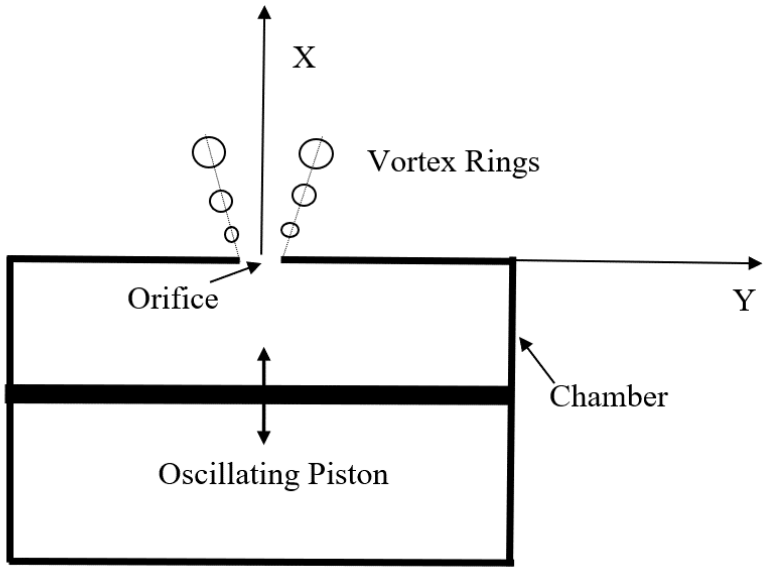

Figure 1.1 Synthetic Jet Formation

1.1.1 Advantages of the Synthetic Jet

The main advantage of a synthetic jet is that it has a zero-net mass flux (ZNMF) at the exit of the orifice. In other words, synthetic jets are formed completely from the working fluid within the surroundings in which they are generated. Thus, it transfers linear momentum to the surrounding flow without any external mass flow source or piping system [4]. Smith and Swift [12] have also concluded that synthetic jets entrain more fluid than continuous jets near the orifice exit due to their formation of vortices. Thus, the spread and the volume flux of synthetic jets have a greater increase in the axial flow direction than do continuous jets.

1.1.2 Synthetic Jet Applications

The advantages mentioned in the previous sub-section make synthetic jets a desirable and an affordable choice in different applications. In the case of aerodynamics, synthetic jets are injected into the boundary layer on airplane wings to reduce the pressure-

induced drag force by delaying the flow separation, as well as, shortening the length and the thickness of the wake [11,12]. Also, synthetic jets can increase energy cooling efficiency (ECE) by providing a high local heat transfer coefficient at a much lower flow rate [8, 13, 15]. Moreover, synthetic jets can be used in thrust vectoring by deflecting the mean flow of an engine jet from the centerline and manipulating the direction of thrust to control the altitude and angular velocity of the vehicle [18].

1.2 Synthetic Jet Ejector (SJE)

Simply, SJEs consist of two main parts: the shroud, or the mixing tube, and the SJA, as shown in Figure 1.2. In the case of SJEs, the primary steady jet in a steady jet ejector is replaced with a SJA, which creates a pressure difference between the fluid inside the shroud and the fluid outside the shroud [19]. Thus, a secondary flow is entrained through the gap between the actuator and the shroud as presented in Figure 1.2. Thereby, the main goal of the shroud is to mix both flows and direct them to the other end of the tube, where the total flow exits. Thus, SJEs can be thought of as a type of self-contained fluidic pump.

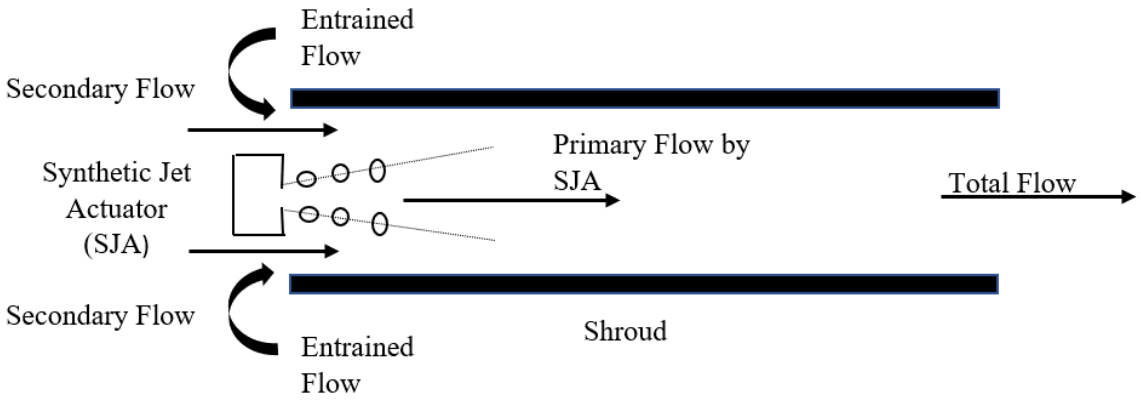

Figure 1.2 Schematic of SJE

1.3 Motivation and Scope

The present thesis is a contribution to the ongoing SJE research here at the University of Windsor. The experimental and numerical work included in this thesis is used to evaluate the simplified numerical model reported in a previous M.A.Sc. thesis [20] and used to estimate the optimum operating conditions.

The thesis is organized into six chapters. Chapter 2 starts with a discussion of dimensionless SJE parameters, followed by synthetic jet characteristics, synthetic jet parameters and a review of the literature that is pertinent to this study. Chapter 3 includes a description of the SJE test facility, the PIV measurement facility, experimental procedure, data reduction, and measurement uncertainty. The numerical model, boundary conditions, grid, timestep determination, turbulence modelling, and solution methods are explained in detail in Chapter 4. The results, including phase-averaged measurements and period-averaged measurements, and the comparisons between the experimental data and the simplified and the improved numerical models are presented in Chapter 5. Conclusions, recommendations and future work are given in Chapter 6.

Chapter 2

LITERATURE REVIEW

This chapter begins by discussing general information including some of the important dimensionless parameters previously used to characterize the flow of the synthetic jets and synthetic jet ejectors. Synthetic jet parameters that control the flow characteristics of synthetic jets formation are also discussed. The last section is devoted to a discussion of some of the previous numerical and experimental studies that have been reported in the literature regarding synthetic jets and synthetic jet ejectors.

2.1 Synthetic Jet Dimensionless Groups

The two most important dimensionless numbers that characterize the synthetic jet flow fields are the Reynolds number and the Strouhal number. Defining a length, time and velocity scale to be used in these numbers is necessary in order to non-dimensionalize the flow field. The Reynolds number for a steady jet is defined as,

$$Re_o = \frac{U_o d}{\vartheta} \tag{2.1}$$

where, U_o is the characteristic velocity, d is the orifice diameter and ϑ is the kinematic viscosity. If the Reynolds number falls below 50, when the characteristic velocity is defined using the amplitude jet exit velocity, the jet will not separate from the orifice edge, and the flow will become reversible with the ejection phase identical and opposite to the

suction phase [21]. The Strouhal number is based on oscillation frequency and the same velocity scale and is shown in Equation 2.2,

$$St_0 = \frac{fd}{U_o} \tag{2.2}$$

A large Strouhal number means that the actuator cycles several times before fluid elements pass through the orifice region, while, small a Strouhal number indicates that the fluid elements pass through the orifice region in one cycle. The square root of the product of Reynolds number and Strouhal number is known as the Stokes number, as given in Equation 2.3. In this study, the Stokes number is the ratio between the thickness of the unsteady boundary layer in the orifice ($\delta^2 = \vartheta f$) to the orifice diameter. The orifice is not strongly influenced by viscous effects if the Stokes number is large, while if the Stokes number is small, the orifice is mostly controlled by viscosity, and the jet can choke on the unsteady boundary layer [21].

$$S = \sqrt{\frac{f\ d^2}{\vartheta}} \tag{2.3}$$

2.1.1 Characteristic Velocity, U_o

For steady jets, the time-mean of the area-averaged instantaneous velocity at the orifice is selected to be characteristic velocity. A velocity scale is difficult to define for synthetic jets since it is unsteady and periodic, as mentioned in Chapter 1. In this case, the time-mean of the area-averaged instantaneous velocity at the orifice exit is equal to zero.

Many different methods have been used to define the characteristic velocity scale for the SJ within the last twenty years. Kral et al. [22] considered the maximum value of the jet instantaneous velocity as the characteristic velocity. Rizzetta et al. [23] used a peak-to-peak orifice velocity value as the velocity scale. Mallinson et al. [24] took the averaged velocity at some distance downstream from the orifice exit as the velocity scale. Utturkar et al. [25] considered the spatial and time-averaged exit velocity during the ejection phase. Smith & Glezer [9] only considered the mean-velocity over the ejection half of the period, since the jet phenomenon is controlled by the ejection phase. Cater & Soria [26] proposed a velocity scale that took into consideration the mean momentum flow.

Since this thesis is based on the evaluation of the optimum conditions from the simplified model [20] for the SJE, the same velocity scale is used in this thesis. This is the same velocity scale that was introduced by Smith & Glezer [9], and it defines the axial velocity for only the ejection half cycle averaged over the cycle, as shown in Equation 2.4

$$U_o = fL_o = \frac{1}{T}\int_0^{T/2} V_p(t)dt \qquad \textbf{(2.4)}$$

In Equation 2.4, f is the piston oscillation frequency, T is the piston oscillating period, $V_p(t)$ is the orifice area-average velocity which is a function of time and L_o is the stroke length. The stroke length is defined as,

$$\mathrm{L_o} = \int_0^{\mathrm{T}/2} \mathrm{V_p(t)dt} \qquad \textbf{(2.5)}$$

For sinusoidally varying uniform velocity,

$$V_p = V_A \sin(2\pi f t) \tag{2.6}$$

Thus, the stroke length and the velocity scale can be simplified as follows,

$$L_o = \frac{V_A}{\pi f} \tag{2.7}$$

$$U_o = \frac{V_A}{\pi} \tag{2.8}$$

2.1.2 Time-Averaged Quantities

For periodic flows, the time-averaged quantities are determined based on the net effect over a full cycle. For example, the period averaged velocity, $\overline{U}$, is defined as the time integral of the velocity value over one period, T, divided by the period, as follows,

$$\overline{U} = \frac{1}{T}\int_{t}^{T+t} V(t)dt \tag{2.9}$$

where time is denoted by t, and V is the area-averaged time-dependant flow velocity.

The number of time steps per cycle (TSPC) is denoted by n,

$$n = \frac{T}{\Delta T} \tag{2.10}$$

where ΔT is the timestep size. Thus, using the rectangular integration (Midpoint rule), the period area-averaged velocity can be estimated as follows,

$$\overline{U} = \frac{\sum_{k=1}^{n} V_k}{n} \tag{2.11}$$

where k is an integer having values 1 to n inclusive [20].

As mentioned in Chapter 1, the SJE shroud involves three different flows: the primary flow, which is generated by the actuator, the secondary flow, which is entrained into the shroud, and the outlet flow, which is a mixture of the primary and secondary flows that is directed out of the shroud. The time average of the primary volume flow rate over one period, period-averaged, is equal to zero because of continuity and the fact that the flow is incompressible. Thus, the period-averaged total volume flow rate equals to the period-averaged secondary volume flow rate. The period area-averaged velocity is used to calculate the period-averaged volume flow rate as shown in Equations 2.12, 2.13, 2.14 and 2.15. In Figure 2.1, the geometry of a simple axis-symmetric synthetic jet ejector is presented. The orifice diameter is defined by *d*, the actuator diameter by *D*, the shroud diameter by *De* and the shroud length by *Le*. Changing any of the above-mentioned dimensions can cause a change in the flow. The symmetry line is parallel to the x-axis. The center point of the orifice exit is considered to be the reference point in this study.

$$Q_{primary} = Q_P = \overline{U_P} * A_P = 0 \tag{2.12}$$

$$Q_{secondary} = Q_s = \overline{U_s} * A_s \tag{2.13}$$

$$Q_{inlet} = Q_i = Q_P + Q_s = Q_s \tag{2.14}$$

$$Q_{outlet} = Q_o = Q_s \tag{2.15}$$

Generally, when the time-averaged flow rate becomes independent of the number of cycles, the flow is considered to have reached a time-periodic steady state. For the present numerical study, the criterion for this condition is taken to be when the secondary inlet volume flow rate between two consecutive cycles is less than 0.5 %.

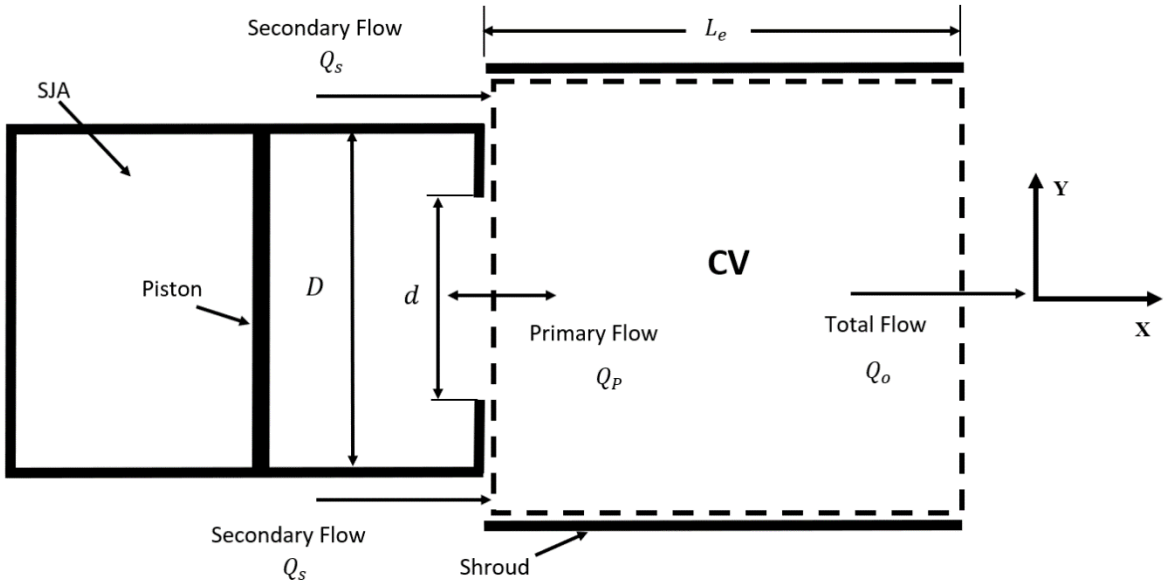

Figure 2.1 Geometric Definitions of SJE and Conservation of Mass over a CV

2.2 Synthetic Jet Ejector Characteristics

Synthetic Jets are created due to the periodic suction and ejection of fluid, by an oscillating driver, through an orifice. Due to boundary separation, the fluid that is pushed through the orifice rolls up and forms vortex rings during the ejection phase of the cycle. During the suction phase, the ambient fluid near the jet exit gets drawn back through the orifice into the actuator, as the expelled vortex ring travels away from the orifice due to its self-induced velocity [27]. Rampunggoon [28] stated that some off-design conditions can

cause the formed vortex ring to be sucked back into the actuator during the suction phase, thus, preventing the formation of a SJ downstream Synthetic jets generate a high turbulence level because of vortex pairs breakdown, due to its circumferential instability, which raises the fluctuation level compared to other jets [29]. Generally, the flow field of the synthetic jets can be classified into two regions: developing region and developed region. The developing region occurs near the orifice exit, where the flow is mostly dominated by the vortex rings. The developed region, which occurs at a distance away from the orifice exit depending upon the jet exit geometry and the turbulence caused by the collapsed vortex rings has the same characteristics as steady jets [30]. Thus, the time-averaged centerline velocity of synthetic jets starts with a value of zero at the orifice exit and rises to a high level at some distance downstream, before it starts decaying [12] according to the -1 power-law decay typical of circular jets [26] and the -1/2 power law for planar jets, as shown in Figure 2.2.

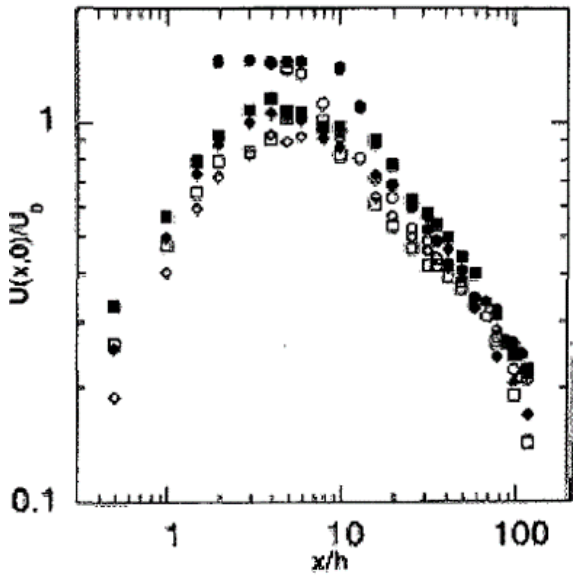

Figure 2.2 Time-Averaged Centerline Velocity Versus Downstream Distance, where h is the Width of the Slot [12]

2.2.1 Entrainment

Entrainment is the ability of a moving fluid to draw in additional fluid from the surrounding fluid. It is one of the main characteristics for jets (both steady and synthetic) and is the operational mechanism responsible in jet ejectors. The jet entrainment rate is defined by the gradient of the entrained mass flow rate in the direction of jet flow, $\Delta M_e/\Delta x$, as first introduced by Ricou and Spalding [31] for a fully developed steady turbulent axisymmetric jet. Hill [32] used Ricou and Spalding's work to directly measure the local entrainment rate in the initial region of an axisymmetric turbulent air jet to determine an entrainment coefficient. The entrainment coefficient, which pertains to the ejector's performance, is provided by Vermeulen et al. [33] and summarized as follows,

$$C_e = \frac{d}{M_j}\sqrt{\frac{\rho_j}{\rho_s}}\frac{\Delta M_e}{\Delta x} \qquad \textit{(2.16)}$$

Where C_e= entrainment coefficient

M_j= jet mass flow rate at the orifice

ρ_j= jet density at the orifice

ρ_s= density of the surrounding atmosphere

M_e= entrained mass flow rate up to position x

x = axial distance from the orifice exit plane

It was concluded by Smith and Swift [12] that synthetic jets entrain more fluid than steady jets do due to the vortex rings formed. For the pulsating jet, it was observed that the entrainment coefficient increased non-linearly with axial distance downstream of the orifice exit plane [33]. It was also found that an acoustic-pulsed driver increased the

entrainment coefficient by up to 4.5 times greater than the non-driven case at x/d = 10, and by up to 5.2 times at x/d = 17.5. Since M_j is zero for synthetic jets and M_e reaches a constant value when the flow reaches a steady state, it is impossible to apply the entrainment coefficient definitions.

In case of synthetic jets ejectors, the fluid is entrained into the primary flow inside the shroud through the secondary inlets. The amount of the entrainment fluid through the secondary inlets depends on the strength of the primary flow generated from the actuator and the size of the secondary flow inlet area.

2.3 Synthetic Jet Ejector Parameters

There are many parameters that control the generation of synthetic jets and their characteristics. The dimensionless groups that were discussed in Section 2.1 are obtained from these parameters. Murugan et al. [29] divided the synthetic jet governing parameters into three categories: actuator operating parameters, geometrical parameters, and fluid parameters. The parameters are summarized in Figure 2.3.

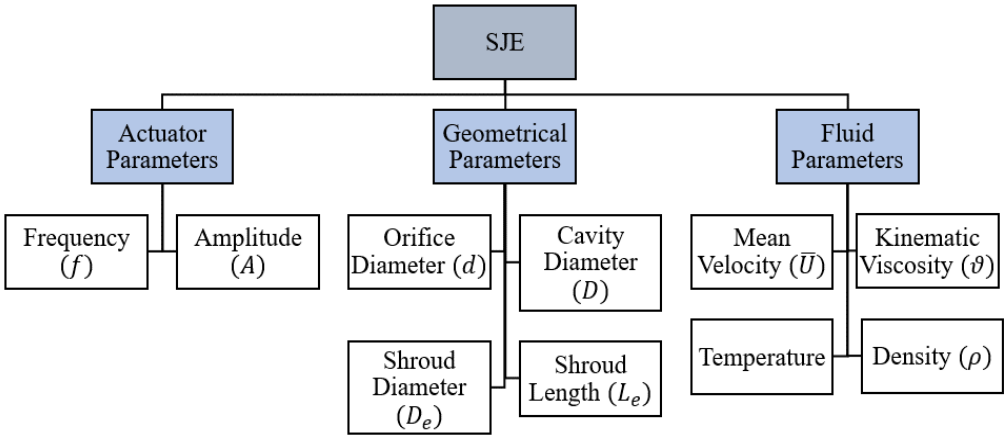

Figure 2.3 Parameters Governing the Synthetic Jet Ejector

2.4 Related Studies

A considerable number of studies have been conducted on the numerical and experimental aspects of synthetic jets. On the other hand, not many studies have been completed for synthetic jet ejectors. This section is divided into four subsections to review the pertinent studies on synthetic jets, synthetic jet ejectors and the behavior of vortex rings formed using a moving piston.

2.4.1 Synthetic Jets

Rayleigh [34,35] was first to notice that vibratory motion of a surface not only generates sound but also causes many phenomena, including a regular air current which is now called acoustic streaming. Eckart [36] developed a second-order mathematical model accounting for the friction, that was the main cause of Rayleigh's phenomena. This mathematical model helped in calculating the steady flow produced by a sound beam of circular cross-section. Subsequently, Ingard & Labate [37] used smoke to visualize the fluid particles and to analyze the acoustical streaming phenomena around an orifice. A sinusoidal motion was developed using acoustic waves and the smoke particle motion visualized using stroboscopic illumination. Therefore, Ingard & Labate were the first to observe what is not called a synthetic jet. In 1994, the first synthetic jet actuator was introduced by Coe et al. [38].

2.4.1.1 Experimental Studies

James et al. [39] experimentally investigated a round turbulent submerged water jet produced by a resonantly driven diaphragm mounted flush with a wall. Due to cavitation bubbles formed on the diaphragm surface and the jet formation was hindered by the suction and ejection of bubbles. Thus, jet spreading was lower than that of aconventional steady

jet. Smith & Glezer [9] evaluated the previous results by comparing the properties for a two-dimensional synthetic jet to a two-dimensional steady jet, for Reynolds numbers that ranged from 104 to 489 and Strouhal numbers from 0.04 to 0.19. They observed that the width and the velocity of the flow produced by a synthetic jet were lower than that generated by a steady jet. However, Cater & Soria [26] experimentally investigated a round Zero Net Mass Flux (ZNMF) jet, for Reynolds numbers ranging from 1,000 to 10,000 and Strouhal numbers ranging from 0.0015 to 0.0072. They observed that in the far field flow, the ZNMF has a cross-stream velocity distribution similar to that of a conventional steady jet, but with a larger spreading rate. Eventually, Glezer & Amitay [4] and Smith & Swift [12] observed that synthetic jets, with Re = 2,000 and St = 0.06, are mainly controlled by vortex pairs near the orifice, which entrain more fluid than steady jets. Thus, the width and the velocity of the synthetic jet are greater compared to the steady jet.

Shuster & Smith [40] studied the flow properties of a round synthetic jet experimentally, using PIV, with Reynolds numbers that ranged from 1,000 to 10,000 and Strouhal numbers from 0.33 to 1. They found that round synthetic jets scales such as time and length scales are defined using the dimensionless stroke length, L_o/d. If the distance from the orifice is less than L_o, the flow is completely dominated by vortex pairs during the ejection phase, beyond which the flow is similar to a turbulent steady jet.

Agrawal & Verma [41] conducted a similarity analysis that was supported by experimental data between a synthetic jet and a continuous jet flow field. It was concluded that synthetic jets have a larger spreading rate than continuous jets.

2.4.1.2 Numerical Studies

Kral et al. [22] conducted two-dimensional incompressible numerical simulations of a synthetic jet with a quiescent external flow. The actuator was prescribed as a sinusoidal velocity profile using the velocity inlet boundary condition. This was done with laminar and turbulent jets, but the laminar case was not able to capture the vortices collapsing that were observed experimentally. Although the synthetic jet actuator operated with ZNMF at the nozzle exit, the jet produced non-zero mean streamwise velocity.

A numerical study by Rizzetta et al. [23] was performed to investigate the interior actuator cavity flow and external jet flow field using the unsteady compressible Navier-Stokes equations and Direct Numerical Simulation (DNS). An oscillatory displacement boundary condition was specified at the lower end of the cavity. It was shown that the internal cavity flow becomes periodic after several cycles. Thus, only the external flow domain was considered in their following simulations using a periodic velocity inlet boundary condition at the actuator outlet. Also, it was noticed that the vortex breakdown due to the spanwise instabilities was not captured using the 2-D simulations, so 3-D simulations were conducted to overcome this issue.

Mallinson et al. [24] studied the synthetic jet flow both experimentally using a single hot-wire anemometer, and computationally, using the commercial software package CFX4.2. The experimental and the computational results for the velocity profile distribution were found to be very similar although the results near the exit were questionable due to the directional ambiguity of the hot-wire. It was discovered that the inertia (diaphragm forcing) and viscous (orifice boundary layer) forces are the main factors that impacted the maximum velocity for a particular actuator configuration.

Rampunggoon [28] numerically investigated the dynamics of synthetic jets in the presence of cross-flow as well as jets issuing into quiescent air using an incompressible Navier-Stokes solver in a two-dimensional configuration. A thorough parametric study of the jet characteristics was conducted by changing various parameters. The diaphragm amplitude, external flow Reynolds number, boundary layer thickness, and slot dimensions were all varied to observe the resulted changes on the flow. It was noticed that large mean recirculation bubbles are formed in the external boundary layer only if the jet velocity is significantly higher than the cross-flow velocity.

Kral et al. [22], Lee & Goldstein [42] again used the DNS method to study the effects of fluid and geometric parameters on the resulting flow field in two-dimensional slot synthetic jets pulsing into an initially quiescent flow. A more uniform velocity profile at the orifice and an increase in the vortex formation rate can be achieved by a thicker orifice lip. Compared with the round orifice lip, a straight orifice lip changed the orifice velocity profile, but the synthetic jet flow field and the formation of vortices were not affected.

Utturkar et al. [25,43] conducted two-dimensional numerical simulations to indicate how the design of the jet cavity would affect synthetic jets by taking into consideration the placement of the oscillating diaphragm and the changes in the cavity aspect ratio. Also, the authors evaluated a jet formation criterion, which was based on $\frac{Re_{U_o}}{S^2}$, for two-dimensional and axisymmetric synthetic jets. Furthermore, the authors have concluded the use of an axisymmetric orifice as the recommended method for generating SJs, at a low Reynolds number, compared to a two-dimensional slot.

Fugal [44] also used Reynolds-averaged Navier-Stokes (RANS) to study how the synthetic jet characteristics would be affected by changing the orifice exit geometry and the dimensionless stroke length. It was observed that the k-ε turbulence model more accurately predicts the downstream behavior of the jet than the other RANS turbulence models. It was also concluded that increasing the exit radius increases the magnitude of the stroke length required to generate a jet.

Ravi et al. [45] conducted a three-dimensional numerical simulation to study how synthetic jets with a larger aspect ratio develop when they are introduced into quiescent air. They used a finite difference based Cartesian grid immersed boundary solver, which is capable of simulating flows with complex 3-D, stationary and moving boundaries. It was found that the vortex train originating from the orifice exit undergoes axis-switching and assumes a complex shape. It was concluded, based on the mean shape of the flow field and the jet spreading, that synthetic jets enhance entrainment of the surrounding fluid.

Jagannatha et al. [46] numerically developed a two-dimensional time-dependent synthetic jet model. The authors stated that the most accurate simulation of the synthetic jet must be accomplished with a 3-D model in order to fully capture the flow behavior. However, the authors added that the synthetic jet behavior can be sufficiently described by a 2-D model that includes a moving piston or a vibrating membrane. They dynamic-layering technique that is simulated by a User Defined Function (UDF) from the Fluent solver was used to represent the piston movement in this simulation. Also, the selection of a proper turbulence model is required since the oscillating nature of the flow could result in some intensely localized fluctuations. It was determined that k- ω SST is the best URANS turbulence model to adapt with this periodic nature of synthetic jets. It was also

concluded that the simulation was able to capture the synthetic jet vortices, the flow field, and heat transfer characteristics related to the pulsating jet cooling.

2.4.2 Vortex Ring Generation Using a Moving Piston

In 1979, Didden [47] investigated the separated flow and the vortex circulation from the flow produced by ejecting fluid from a circular nozzle by means of an impulsively-started piston. The experiment was conducted using Laser-Doppler Velocimetry (LDV) technique. It was concluded that the circulation generated from this experiment, using a piston, underestimates the strength of the ring by approximately 25 % compared to the models where constant velocity profiles across the nozzle's cross section was assumed.

Allen and Auvity [48] used Didden's [47] geometry and circulation model to study the effect of the piston vortex, which is formed in front of the advancing piston within the cylinder, on the primary vortex ring that is generated at the orifice exit. The experiment was carried out by a moving piston ejecting fluid from a tube into a large tank. It was concluded that a piston finishing flush with the exit plane produces vortex rings with significant flow complexity. The piston vortex is injected and entrained into the primary vortex which resulted in an added impulse to the vortex ring. They also found evidence of a centrifugal instability on the piston vortex which generates vortex filaments in a plane perpendicular to the azimuthal direction. Also, some vorticity filaments, due to the centrifugal instability on the piston vortex, were detected in the plane perpendicular to the azimuthal direction. They found that the piston vortex reduces the distance that the ring is convected before transition occurs.

2.4.3 Synthetic Jet Ejector

Vermeulen et al. [49] conducted both numerical and experimental studies to show that adding a pulsation to a steady primary jet flow improves the ejector's performance. They also considered the special case of synthetic jet and showed that a "strong" synthetic jet actuator that is pulsed at 131 Hz with a velocity of 91 m/s for the zero primary jet velocity gives ejector performance as good as a pulsed high-velocity flow jet using a 150 W loudspeaker. The pumping effectiveness, defined as the mass flow rate ratio of secondary to primary flows, $\frac{M_S}{M_P}$, increased by up to 4.5 times that for a steady jet. It is speculated that the pumping effectiveness improvement was due to the high velocity at the boundary of the jet which is caused by the vortices generated. It was also observed that the majority of the entrainment happens at the initial vortex immediately downstream of the orifice exit. It was concluded by Meng [50] that SJEs enhance the entrainment better than the pulsating jets and rotor valve pumps. For long experiments, controlling the chamber's temperature was considered the only disadvantage of the SJE for that conducted experiment.

Lin [20,51] numerically investigated the behavior of particular configuration of synthetic jet ejector. An efficient numerical model was developed, and an extensive parametric study conducted. Univariate search optimization method was applied to determine the set of parameters that yield the maximum flow rate. Thus, optimum SJE dimensionless groups were then generated and summarized. This optimum configuration was then investigated for the use in an innovative seat ventilation system. For the simplified numerical model developed, the velocity profile is uniform across the primary flow inlet and varies periodically with a specified frequency, f and amplitude, V_A. It was

assumed that the secondary flow inlet has a constant pressure profile with a zero-gauge pressure that was implemented as a pressure inlet condition. The shroud exit was set to atmospheric pressure and implemented as a pressure outlet condition. The final grid used after conducting a grid convergence study contains 400×120 cells. The final timestep size, after conducting a timestep convergence study, was 1.38×10^{-5} s. The turbulence model used for this study was $k - \varepsilon$.

2.4.3.1 SJE Applications

Mahalingam & Glezer [52] designed and built a synthetic jet ejector that operated as an air-cooled heat sink. This module consists of a plate-fin heat sink integrated with synthetic jet actuators. The synthetic jet module contains a plenum that is driven by electromagnetic actuators. Each fin of a plate-fin heat sink is straddled by a pair of synthetic jets. Thus, the ejector system trails the cool air upstream of the heat sink and discharges it into the channels. It was concluded that the heat transfer coefficient generated using synthetic jet ejectors are 150 % greater than those generated using steady jets.

Mahalingam & Glezer [53] studied how synthetic jet ejectors can be used to augment the cooling provided by a global fan flow by reducing flow bypass. Flow bypass is defined that it is the air flowing above and around heat sinks that results in significant reduction in the amount of flow entering a heat sink. Adding synthetic jets upstream of the inlet to the heat sink allows re-entrainment of the inlet flow to reduce flow bypass. It was stated that synthetic jets helped to augment the heat dissipation of a heat sink by 25-35 %. Later, Mahalingam et al. [54] added that doubling the jet speed led to a 20 % increase in heat dissipation augmentation performance. Furthermore, the use of SJE helped in

reducing the noise level by 9 dBA, as it allowed the dual fans to operate at 6500 RPM instead of 9000 RPM.

2.4.4 Summary

It is shown from the literature that not many studies have been completed of synthetic jet ejectors. Also, none of the studies found regarding SJEs include a combined numerical and experimental studies. For instance, the simplified numerical solution [20] lacked an experimental validation. Furthermore, previous studies can be found regarding submerged SJs in water [8–10, 55, 56], but no studies known to the author exists on analyzing SJEs with water as a working fluid. Thus, this thesis focuses on the behaviour of SJEs in water, both experimentally and numerically.

2.5 Objectives

The main goal of this research is to evaluate the accuracy of the 2-D SJE model developed by Lin to determine the optimum conditions [20]. For this purpose, the flow field of the SJE with optimum geometry and operating conditions is investigated in detail using PIV experiments and numerical simulations. The specific objectives are as follows:

- To design and construct a SJE test facility with water as the working fluid that is dynamically similar to the optimum conditions from the simplified model.
- To measure the velocity fields using Particle Image Velocimetry (PIV) and determine the period-averaged volume flow rate experimentally.
- To develop a more realistic CFD model based on the optimum conditions from the simplified model.

- To use the more realistic numerical model to evaluate the assumptions made in the simplified numerical model and compare their predicted phase-averaged volume flowrate variation throughout the cycle with the experimental results.
- To compare the details of the experimental velocity results with the new, realistic, numerical results.

Chapter 3

EXPERIMENTAL METHOD

This chapter begins by introducing the constraints, and the selected SJE geometry for this study, which is based on the previously reported optimum SJE conditions [20]. Mechanical design of the SJE test facility are provided followed by the description of the phase-averaged velocity measurements using PIV technique. The experimental procedure and data reduction techniques are then explained in detail. The last section is devoted to the discussion of the method that is used to estimate the PIV measurements uncertainty.

3.1 SJE Geometry Selection

The predicted optimum dimensionless parameters that yield the maximum flow rate out of the synthetic jet ejector studied and presented in Lin's thesis [20] are summarized in Table 3.1

Table 3.1 General SJE Dimensionless Groups Optimum Operating Values

Dimensionless Group (Pi Terms)	Optimum Value
$\frac{Q_s}{{D_e}^2 V_A}$	0.262
d/D_e	0.8
D/D_e	0.8
L_e/D_e	4
$\frac{f\ D_e}{V_A}$	0.323
$\frac{\rho\ V_A\ D_e}{\mu}$	20,000
$\frac{\Delta p}{\rho\ {V_A}^2}$	0

One requirement in the design of the experimental flow facility is that flow visualization of dye traces and quantitative velocity measurement techniques such as laser Doppler anemometry can easily be applied. All these techniques are more easily applied in liquids hence, it was decided to use water as the working fluid. The arrangement of the experimental facility is shown in Figure 3.1. The SJE axis is vertical with the actuator fastened to the bottom of a larger tank containing water. The shroud is also fastened to the tank bottom so that it is co-axial with the actuator. The shroud and tank walls are plexiglass to allow flow visualization. The tank size was selected to be 1 m^3 in volume, 1m × 1m × 1m. Since the water in the tank containing the ejector must approximate a stationary media and the fact that the water has a free surface, it is necessary to use a large tank. In order to allow good spatial resolution for measurements and flow visualization within the shroud, the inside diameter of the shroud, D_e, is selected to be equal to 10 cm, which resulted in an outer diameter value of 10.7 cm, considering standard size tubes. Based on the shroud diameter selection and the optimum conditions obtained from the simplified model, the remainder of the SJE parameters are calculated and summarized in Table 3.2.

According to the optimized dimensions, as presented in Table 3.2, the actuator's diameter, D, is equal to the orifice diameter, d, which means that the actuator wall thickness is zero which is impossible to implement in practice. Moreover, the highlighted flow rate, from Table 3.2, corresponds to the periodic-averaged secondary volume flow rate, which is equal to the periodic-averaged total volume flow rate, as discussed in Chapter 2.

Table 3.2 The Optimized Dimensions & Parameters

Parameter	Value
Tank width (m)	1.0000
Shroud Diameter (De) (m)	0.1070
Actuator Diameter (D) (m)	0.0805
Orifice Diameter (d) (m)	0.0805
Shroud Length (Le) (m)	0.4000
Amplitude Velocity (Va) (m/sec)	0.1873
Frequency (f)(Hz)	0.5654
Period (T) (s)	1.7687
Stroke Length (Lo) (m)	0.1054
Amplitude (Sa) (m)	0.0527
Secondary Flow Rate (Qs) (m^3/sec)	0.00056
Angular Velocity (w) (rad/sec)	3.5525
Amplitude Acceleration (Aa) (m/s^2)	0.6654
Shroud Average Velocity (m/sec)	0.0625
Return Average Velocity (m/sec)	0.0006

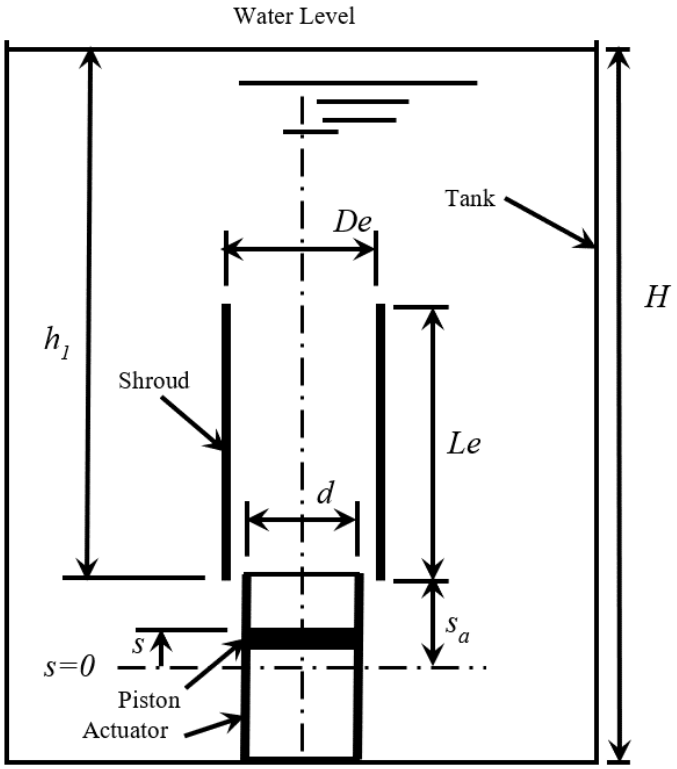

Figure 3.1 Shroud- Actuator-Tank Arrangement with Dimensions

3.2 SJE Test Facility

This section describes the main components of the SJE test facility and its specifications. Figure 3.2 shows a schematic CAD model for the SJE design, excluding the tank walls. All components are positioned on the top of the bench that is made of welded angle iron.

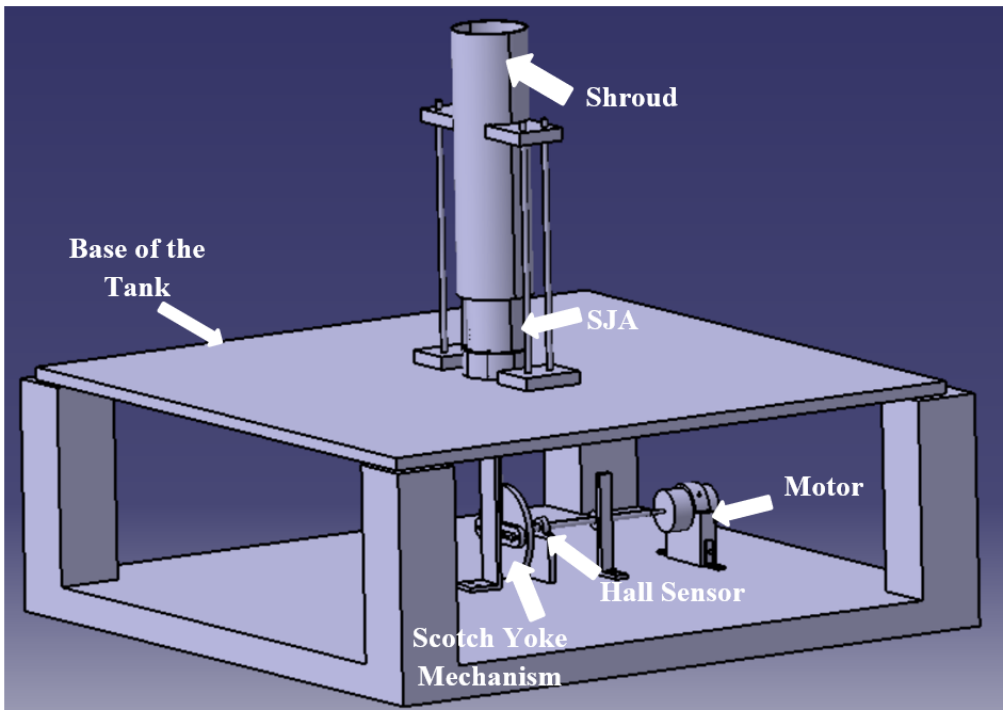

Figure 3.2 Schematic of the SJE CAD Model

3.2.1 The Containment Tank

As stated previously, the tank is filled with water, and the actuator and the shroud, which are the main components of the SJE, are centered on the base of the tank as shown in Figure 3.2.

The tank is made of five clear optical acrylic sheets, one for the base and one for each of the four sides. The base of the tank is designed to be 38.5 × 38.5 in^2 (98 × 98

cm^2). Two of the side acrylic sheets have a size of 38.5 × 39.5 in^2 (98 × 100 cm^2), and the size of the other two sheets is 40 × 39.5 in^2 (101.6 × 100 cm^2). The walls and the base of the tank are attached together using a dichloroethylene glue. The detailed drawings of the tank walls and its base as well as the other components to be discussed in Section 3.2 are presented in Appendix A.

A 4.5 in (11.4 cm) outer diameter (OD) clear acrylic tube with a thickness of 0.125 in (0.318 cm) and a length of 1.3 ft (39.6 cm) is used to represent the shroud. The transparency of the clear acrylic shroud allows for better in-shroud flow visualization. The actuator is machined from a solid 7075-aluminum cylinder. The actuator's inner diameter (ID) is 3.18 in (8.08 cm) with a thickness of 0.125 in 0.317 cm and a length of 12 cm. Since the stroke length of the piston, travelling inside the actuator, is approximately 10 cm, an extra 2 cm is left in the bottom of the actuator to adapt to any potential future changes. The aluminum actuator is also designed to include a flange at the bottom of the actuator. Two supports are attached to the shroud that are used to center the shroud over the actuator, as shown in Figure 3.2. The piston used as the oscillating driver for this SJA is made of polytetrafluoroethylene (PTFE), Teflon. Two nitrile rubber O-rings are placed around the piston to ensure a seal against any water leaks. Figure 3.3 shows an isometric view of the piston inside the actuator.

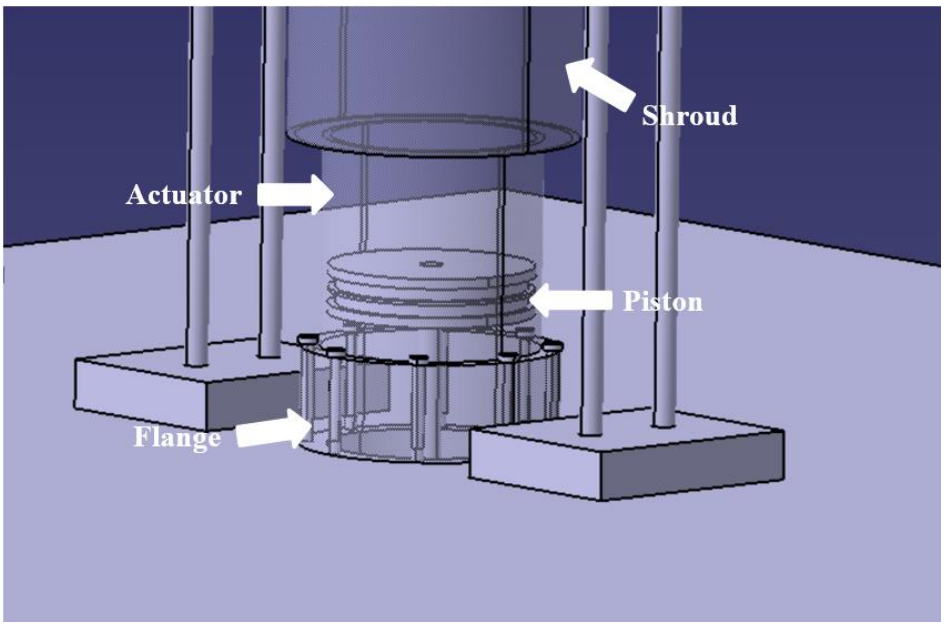

Figure 3.3 Isometric Drawing of the Piston and SJA

3.2.2 Scotch Yoke Mechanism

Since the piston is used as the oscillating driver, a proper reciprocating mechanism is necessary. The reciprocating mechanism selected for this SJE is the Scotch Yoke mechanism. Figure 3.4 shows the main components of the Scotch Yoke mechanism.

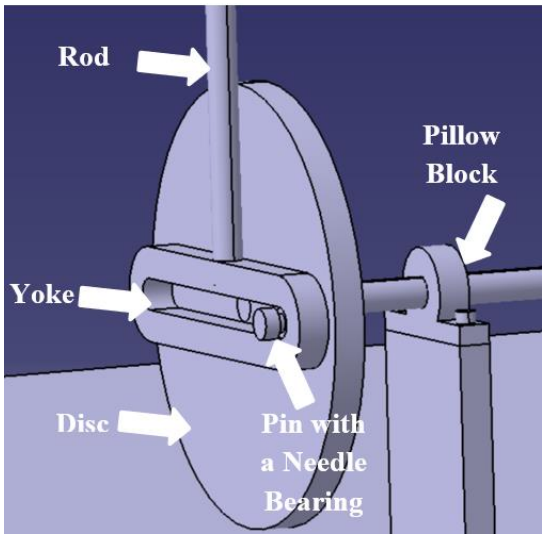

Figure 3.4 Components of the Scotch Yoke Mechanism

The Scotch Yoke mechanism was first designed by Charles Algernon Parsons [57]. The early application for this mechanism was on steam pumps, but now it is used as a mechanism on a test machine to produce vibrations. Simply, the Scotch Yoke is used to convert the angular motion to a linear one or vice versa. Also, this mechanism is able to provide a pure sine wave motion [58]. The basic idea of the Scotch Yoke mechanism includes a scotch, or it can be called a disk, that is rotated or driven by a motor, a pin that is connected to the scotch, and a yoke, where the pin slides along relative to the yoke [59].

For the present design, the upper face of the yoke is attached to a rod that is used to move the piston up and down within the cavity, from the bottom dead centre (BDC) to the top dead centre (TDC). The rod travels through two linear bearings to prevent angular motion of the rod. A needle bearing, which is made of hardened carbon steel, rolls along the inside surface of the yoke. The disk, which is the second main part of this mechanism, is connected to the bearing by a shoulder pin. The center of the other face of the disk is connected by keyway to a rotary shaft. The other end of the rotary shaft is connected to a DC motor by a flexible coupler to allow for small misalignment between the rotary shaft and the motor's shaft.

3.2.3 Motor Selection

Power is supplied from a GPR-6060D DC power supply to operate the DC motor The motor selected for this purpose is a Model 011-348-5030 Bison Gearmotor, which is rated at 1/8 hp, with a maximum voltage of 24 VDC and has a gear ratio of 28.1:1. The maximum angular velocity is 64 RPM with a torque of 112 lb-in (12.65 N-m).

The process of selecting the motor is based on an estimation of the maximum values of motor torque and power predicted during the cycle using a lumped parameter mathematical model, which is discussed in a capstone report by Alaswad [60]. In addition, a Finite Element Analysis (FEA) was conducted on the yoke, the shoulder bolt used to connect the yoke with the disc, the walls of the tank and the needle bearing to ensure that material stresses are within acceptable limits [60].

3.3 PIV Measurement Facility

3.3.1 Introduction

Particle image velocimetry is a non-intrusive velocity measurement technique providing information for the velocity field in a flow at multiple points simultaneously. A typical PIV system usually consists of three main components: a pulsed laser, a charger-coupled device (CCD) camera, and a synchronizer. The illumination from the laser must be of short time duration in order to accurately indicate the particle positions. Also, the illumination intensity must be such that it equally illuminates all particles in the fluid field of view (FOV). The seeding particles are illuminated on a particular plane twice within a very short time-interval by a laser sheet. The light scattered by each of these particles is recorded either as a multiple exposure on a single frame or as a single exposure on several frames. The later method has the advantage of allowing an indication of the direction as well as the magnitude of the velocity vector and is the one used in this thesis. In this case, the velocity can be determined by simply dividing the average displacement of the particles within a small interrogation region, found by a cross-correlation calculation two field of views (FOV's), by the predetermined short time interval, Δt. Therefore, the PIV technique does not measure the fluid velocity directly, but it measures the average displacement of

the tracer particles within a small region. The properties of the tracer particles, hence, must be such that they represent the fluid velocity in a satisfactory way. The particles must be large enough to reflect enough light to be captured by the camera. They must, however, be small enough to follow the flow faithfully. Also, the density of the tracer particles can influence their ability to follow the flow hence, neutrally buoyant particles are recommended.

3.3.2 PIV Facility Specifications

The PIV system used in this thesis consists of dual pulse Litron Nano L series Neodym-Yttrium-Aluminum-Garnet (Nd:YAG) laser, which is placed above the tank. Its output beam has a wavelength of 532 nm and an energy of 135 mJ/pulse with a maximum repetition rate of 15 Hz. The laser sheet is first expanded through a -15 mm cylindrical lens and then focused through a spherical lens with a focal length of 1000 mm, into the plane of interest. The images are recorded using a (TSI) PowerViewPlus 8 MP 12-bit digital camera with a resolution of 3320×2496 pixels operating in dual capture mode. The intensity of the incident light at any pixel is discretized into 2^n intensity levels, where n is the number of bits of the camera. Thus, the entire intensity range is discretized into 4096 levels. A TSI PIV 610035 LaserPulse synchronizer is used to synchronize the camera's operation with the laser. The camera is mounted with a 50 mm Nikkor lens. The images are captured and collected using the Insight 4G software developed by Thermal System Inc. (TSI). Both camera and laser are synchronized with the built-in delay generator in the synchronizer, which is externally triggered by a Hall sensor that detects the reciprocating piston position during its motion, at the bottom dead centre (BDC) in the actuator's cavity. Figure 3.5 shows the experimental set-up, including the PIV equipment

and the SJE test facility. The seeding particles used for this project are silvered hollow glass sphere of mean diameter 17 μm with a density of 1.6 g/cc, which are manufactured by Potters Industries [61]. It is shown in Appendix B, that these seeding particles follow the flow faithfully.

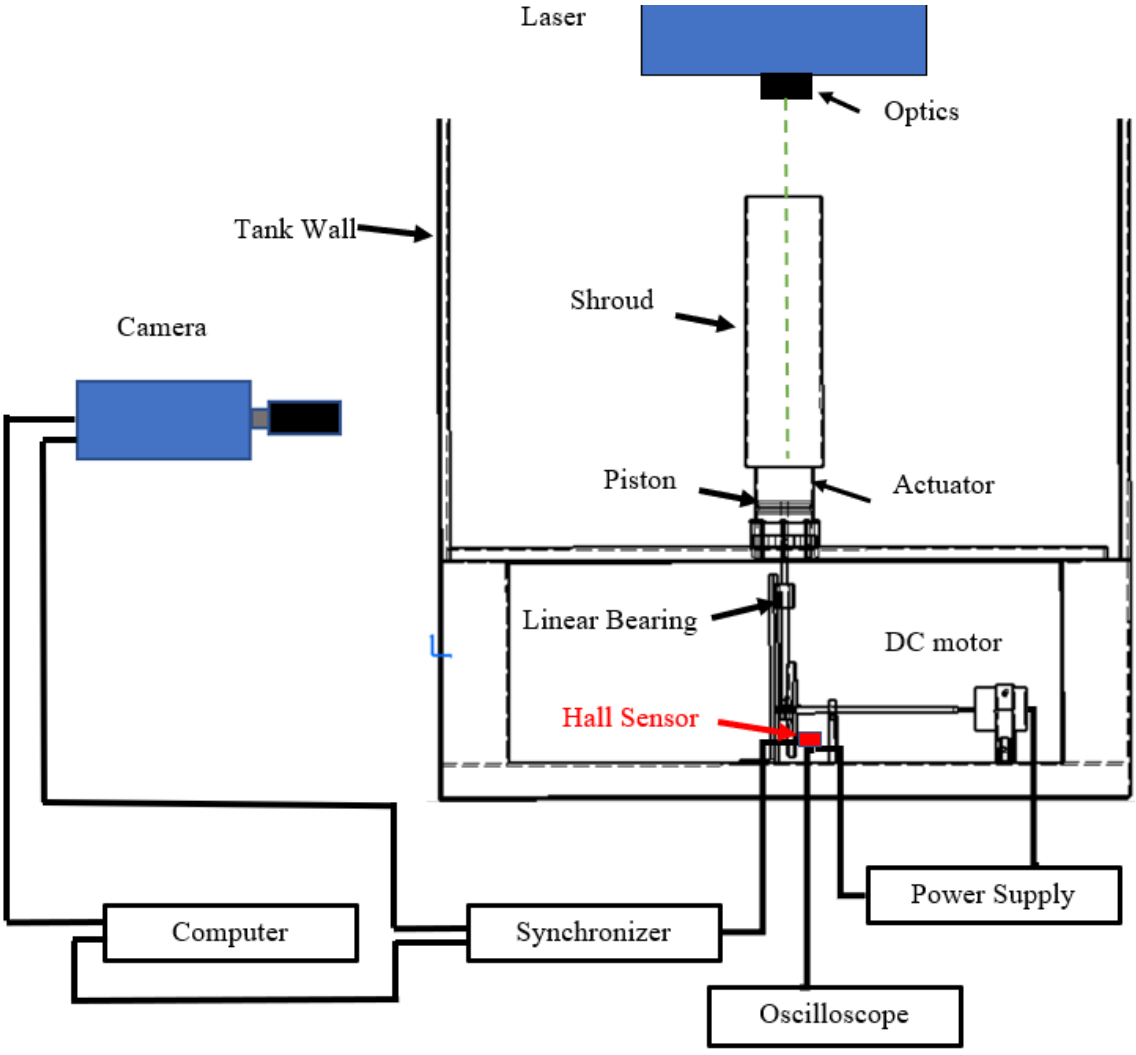

Figure 3.5 Experimental PIV Set-up

3.4 Experimental Procedure

After setting up the experimental test facility and the PIV system, the tank is filled with water to a height of 65 cm. The tank is left for a few days in order to remove the gas-bubbles formed on the walls of the tank and the shroud from dissolved oxygen in the tap water that is used. Steel rulers with a minimum division of 1 mm are glued to an acrylic block and immersed inside the synthetic jet ejector's shroud, on top of the actuator's surface as shown in Figure 3.6. This is used to calibrate the acquired images of the FOV. After positioning the calibration block, the position of the laser is adjusted, using a traverse, to illuminate the centre plane of the piston/actuator. The distance of the camera from the block is adjusted manually to obtain the best possible view with desired focusing level.

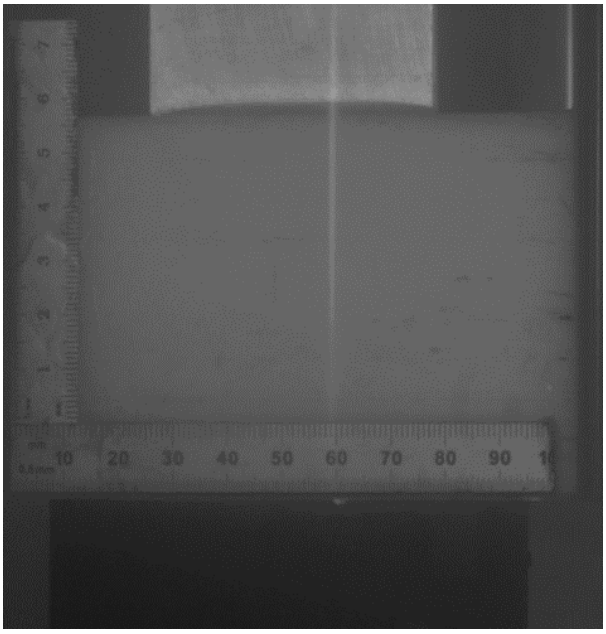

Figure 3.6 Calibration Image

3.4.1 External Triggering

Since the synthetic jet is unsteady and because of the limitations on the rate at which measurement scan be made with the PIV apparatus, phase-averaged measurements are required for mapping the velocity field over the entire cycle. A Hall sensor and the gate circuit shown in Figure 3.7 are used to send a transistor-transistor logic (TTL) signal to the synchronizer whenever the piston passes the reference point, which was indicated previously to be in the middle of the actuator, 90° clockwise (CW) from the BDC as shown in Figure 3.1. Once the synchronizer receives the signal, it triggers the illumination of the laser sheet, which also opens and closes the shutter of the camera twice to capture a pair of images (FOV's) within the selected Δt. The TTL signal that is received by the synchronizer is monitored using an oscilloscope as displayed in Figure 3.8. The period between the two trigger signals measured with the oscilloscope is 1.7 s, which represents the period of a piston cycle. Using Insight 4G software, the external triggering delay option is used to set the time within the period in which the measurements are made. The delay is sequentially set to 10 different values to capture ten points that are spaced equally within the cycle of the piston oscillation. The ten points, or delays within the cycle are made dimensionless by dividing with the cycle period and expressed graphically in Figure 3.9. The software set-up that was used to acquire the PIV measurements is explained in Appendix C.

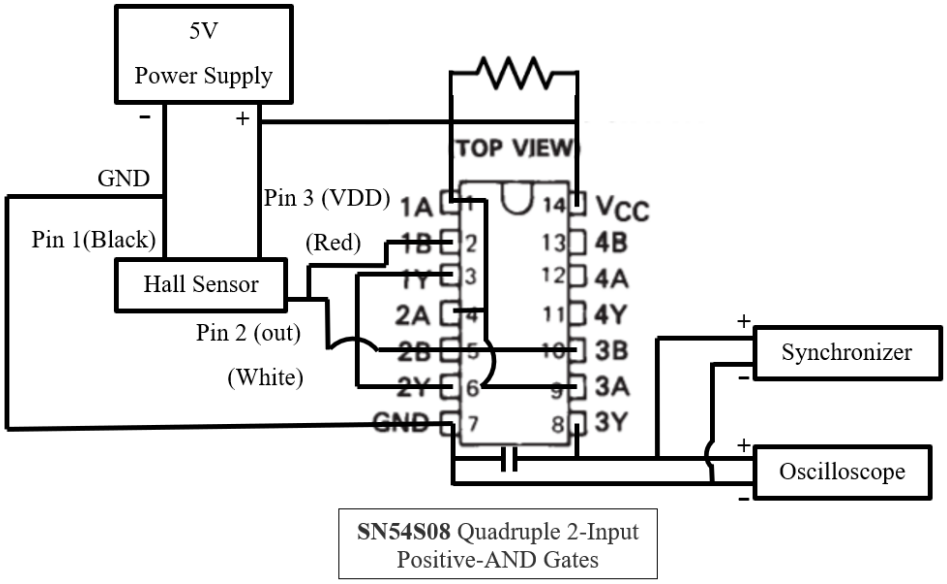

Figure 3.7 The Circuit that Converts the Digital Signal from the Hall Sensor to a TTL Signal that Externally Triggers the Synchronizer

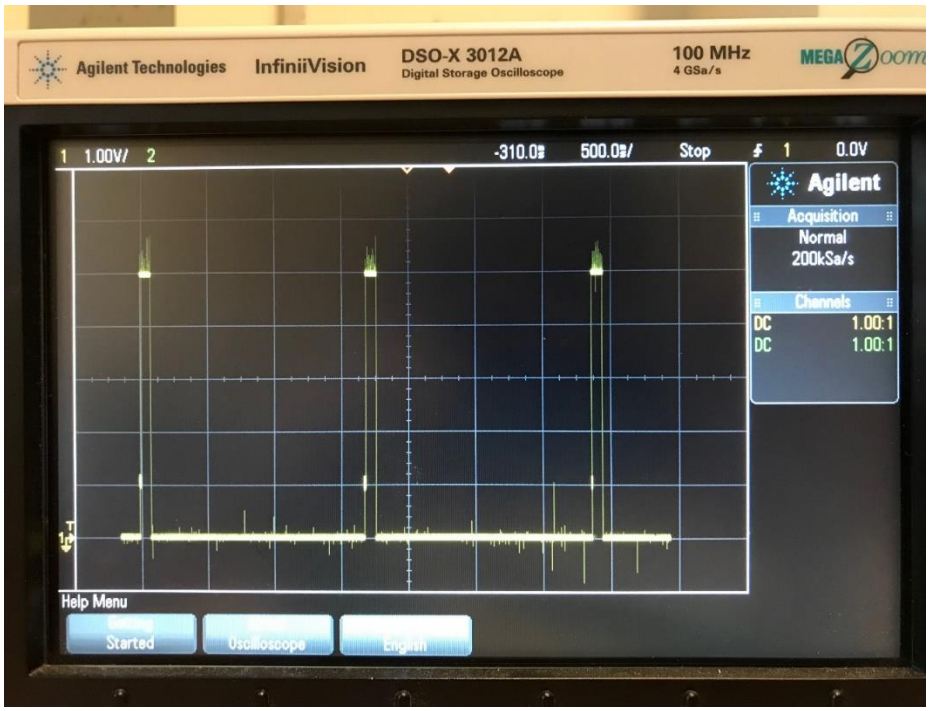

Figure 3.8 TTL Signals Generated by the Hall Sensor

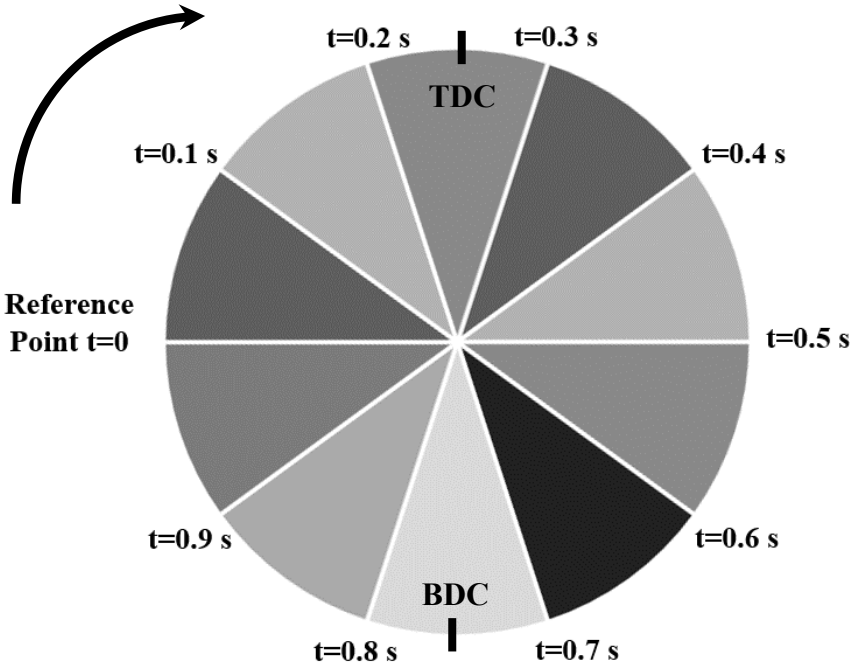

Figure 3.9 Captured Points within Dimensionless Time during a Cycle

3.5 Data Reduction

3.5.1 Image Evaluation Methods

An essential part of the PIV analysis is cross-correlation interrogation. Image pairs from a small interrogation area (IA) are cross correlated to determine an average displacement of the particles within the IA. Thus, the cross-correlation is a statistical pattern analysis method that is used to determine the differences in the particle patterns between the image in frame A and that in frame B. Huang et al. [62] defined this statistical method with the discrete cross-correlation function as shown in Equation 3.1,

$$C(m,n) = \sum_{i}\sum_{j} A(i,j)B(i-m,j-n) \qquad \textit{(3.1)}$$

where A and B are the corresponding images from frame A and frame B.

Since this quantity indicates agreement of particle positions in image A with those in image B, the shift in the location of the intensity peak in the correlation matrix C from a value of zero gives the most probable linear shift in the particles or the displacement vector from A to B for that particular IA. Once the displacement vector and the time interval Δt between the image pairs are identified, the velocity vector at time t for that IA can be determined using Equation 3.2.

$$V(IA, t) = \frac{S}{\Delta t} \qquad \textit{(3.2)}$$

There are two methods that can be used to determine the given C matrix in Equation 3.1: Direct Cross-Correlation (DCC) and Discrete Fourier Transform (DFT) [63]. The DFT method uses a Fast Fourier Transform (FFT) to determine the displacement [79]. The FFT method is explained briefly in the next section since it is the method used in this study.

Raffel et al [64] stated that the whole image is first divided into a number of small IAs depending on the velocity spatial resolution that we want. The cross-correlation is performed on each IA to obtain the average velocity vector. Using the FFT method instead of the DCC requires less computer operations and hence saves computational time. The concept of the FFT method is based on the fact that the cross-correlation of two functions can be simply found by taking the magnitude of the inverse FFT of the product of the FFT of image A(I, j) with the FFT of image B(i-m, j-n). Alternately, it is possible to take the product of the FFT of image A(I, j) with the complex conjugate of the FFT of image B(i-m, j-n). It is important to note that the displacement of the particles must be smaller than half the size of the interrogation area, otherwise aliasing occurs causing the intensity peak

in the correlation matrix to be folded back into the matrix and could appear on the opposite side of the matrix. Thus, it is recommended by Keane and Adrian [65] to keep the displacement less than one-quarter of the IA size, so the background noise in the correlation matrix remains low compared to the correlation peak.

3.5.2 Image Analysis

For each experiment, 1500 raw image pairs are acquired. The first image in each pair contains the information about the initial position of each particle, while the second image includes the information of particles moved by a small distance throughout the time, Δt. The images are analyzed using the free MATLAB software package, PIVlab ver. 2.02, which was developed by Thielicke [63]. After defining a mask to exclude the actuator from the analysis and identifying the region of interest, background subtraction is then applied to improve the contrast of the images. The intensity capping is applied to eliminate the bright spots within the images. The FFT cross-correlation PIV algorithm is then selected and the correlation process performed in two passes. Initially, the IA size is reduced from 64 × 64 pixels to 32 × 32 pixels for an estimate of the displacements. The grid is further refined to 16 × 16 pixels and the displacements are reanalyzed with 50 % overlapping. The correlation peak is located within an accuracy of one half pixel using a Gaussian curve-fitting method. The particle displacement is determined using the calibration scale. This process yields a final interrogation area with size of 16 × 16 pixels. The size of the average field-of-view of 212 × 108 mm and camera resolution of 3320 × 2496 pixels are employed in the present PIV measurements corresponding to an interrogation area size of 1.09 mm^2. The spatial resolution for all experiments is estimated to be 1.86 mm. The velocity vectors are then validated using the standard deviation filter

threshold and the local median filter threshold to replace the bad velocity vectors by the interpolated data.

3.6 PIV Uncertainty Analysis

Although taking the PIV measurements is considered a conventional procedure, quantifying the uncertainty related to this technique remains challenging and unclear. The PIV uncertainty approach utilizes information regarding the image capturing process as well as the image analysis processes. Like any other typical measurements, the PIV uncertainty analysis can be split into systematic (bias) and random errors.

The bias error can be caused by a large number of factors, as stated by Coleman and Steele [66]. These include such things as the timing order of the laser pulse, the calibration errors and the image particle diameter. Willert and Gharib [67] concluded that different seeding particle densities can vary the displacement error from 1 % to 10 %. Prasad et al. [68] proved that the seeding particle image diameter has to be larger than the image pixel resolution, otherwise, the bias error would increase significantly. Furthermore, Forliti et al. [69] estimated the error in the mean particle displacement for the Gaussian-fitting algorithm to be between 0.05 to 0.1 pixel.

Sciacchitano et al. [70] summarized the main factors that cause random error augmentation. The paring loss in the second image, the irregular seed particle images, the electronic noise in the pixel readout and the strong velocity gradients can increase the random error considerably. The change in laser intensity and the out-of-plane motion of seed particles can cause the loss of information in the second image within PIV measurements. Also, Prasad et al. [68] added that the random error can be increased due

to the fact that non-spherical particles that can show distortion from one exposure to another.

In this case, the method used to analyse uncertainties is that proposed by the Visualization Society of Japan (VSJ) [71] as a result of the PIV standardization (PIV-STD) project [72]. A guideline for estimation of the uncertainty of a PIV dataset was based on this procedure and presented at the International Towing Tank Conference (ITTC) in 2008 [73]. A short summary of the method used, and the error sources used in this study are given in Appendix D. A detailed definition of each source of error can be found in the guideline. The cumulative uncertainty was found to be approximately $\pm$ 0.00159 m/s.

Chapter 4

NUMERICAL METHOD

This chapter begins by describing the simplified numerical model [20], since the current study is an evaluation of that method. A description of the current numerical method is then given. The geometry is first described, followed by specification of the boundary and initial conditions. The turbulence model used is then explained in detail and the solver and the discretization schemes both in space and time discussed. The mesh generation and the grid independence study are then presented. The last section is devoted to the timestep independence study.

4.1 Lin's Numerical Model

One of the objectives of this study is to investigate the effectiveness of the numerical model and assumptions used to determine the SJE optimum conditions found by Lin [20]. While the details of his solution and optimization are available in his thesis, it is helpful to briefly explain the salient features of his numerical model and geometrical modifications necessary to compare with the current improved numerical model. The computational domain including the boundary conditions used in the simplified numerical model are summarized in Figure 4.1. The model did not simulate the motion of the piston explicitly, and it operated under restrictive assumptions that need to be justified. It was assumed that the secondary flow inlet has a constant pressure profile with a zero-gauge pressure that was implemented as a pressure inlet condition. This implies that there is no loss in energy in the flow as it approaches the secondary flow inlet plane from the surroundings. It was also assumed that the velocity profile is uniform across the primary

flow inlet and varies periodically with a specified frequency, f and amplitude, V_A. The SJE geometry conditions found by the simplified model to generate an optimal maximum flow, included a zero-wall thickness between the primary and secondary flows (actuator wall thickness). This condition, however, cannot be realized or implemented in either the practical application or in the CFD simulations. To approximate a zero-wall thickness, Lin assigned a very small wall thickness of 0.25 mm. In the current experimental study, it is necessary to have an actuator wall thickness of 2.5 mm. In order to make a fair comparison between the simplified numerical model and the current numerical and experimental results, Lin's assumptions, boundary conditions and numerical solution methods are applied to the current experimental geometry and flow conditions. Solutions obtained using these conditions (not given in the thesis) closely approximated the optimum dimensionless parameters specified in the simplified numerical model as presented in Table 3.1.

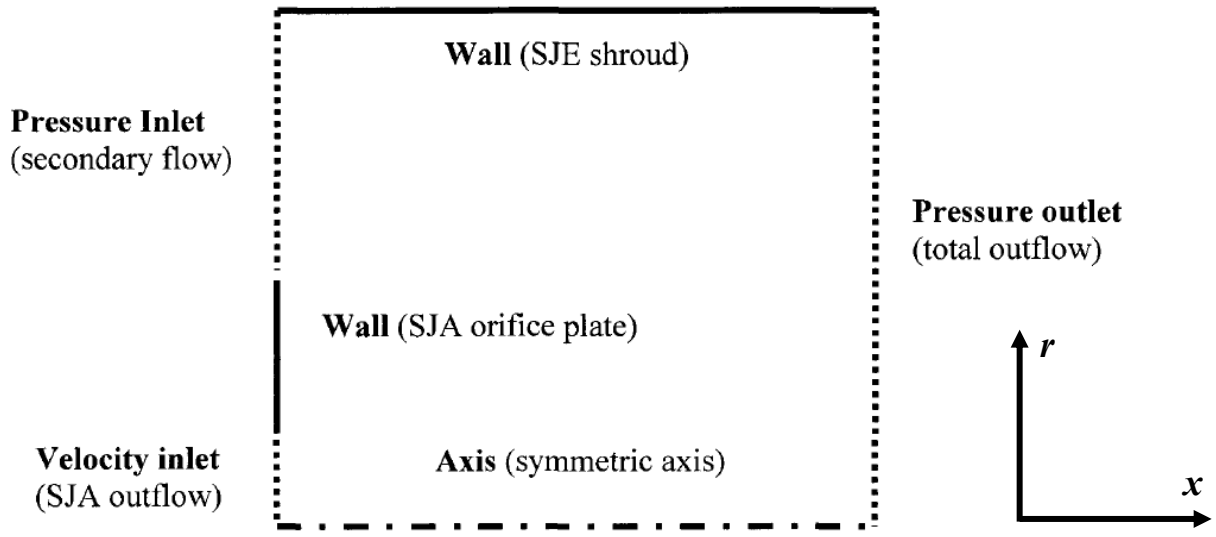

***Figure 4.1 Lin's SJE Numerical Model Boundary Conditions** [20]*

4.2 Improved Numerical Model

The main enhancements made in the improved numerical model in the current study are as follows. A better representation of the primary jet velocity profile is made by accurately modeling the piston motion. Also, the losses in the flow approaching the secondary inlet plane and the variation of pressure on it are more accurately modelled by including the surrounding fluid in the solution domain. In order to make a fair comparison with the experimental results, features of the experimental facility such as gravity and the free surface are also modelled.

4.2.1 Computational Domain

The SJE in this study has an axisymmetric geometry, therefore an axial symmetry is assumed for the flow field. The axial symmetric model was previously used by Lin [20] and also has been found to give acceptable results by Jagannatha et al. [46] for the case of a circular synthetic jet based cooling module. They reported that axial-velocity results obtained from the axisymmetric numerical model agree with the experimental results using the techniques of PIV, hot wire anemometry and Laser Doppler Velocimetry (LDV). As described in Section 3.2.1, the experimental SJE test facility is located in a square containment tank with 1 m × 1 m cross section. This is different from the computational domain, where the axisymmetric condition implies a cylindrical containment tank with a 1 m diameter. This difference is minor and will not significantly affect the velocity field in the SJE. In the experiments, the square containment tank is preferred since it eliminates the optical distortion due to the curvature of the SJE. The computational domain for this study is shown in Figure 4.1 along with the orientation of the coordinate system. It is important to note that the axis of symmetry is along the x-axis (or horizontal axis) which

is a requirement of Fluent. One should note that the gravitational acceleration is acting in the negative x direction. Also, the moving piston is shown in Figure 4.2 to represent the oscillating driving mechanism. With the exception of the containment tank geometry, the geometry and dimensions are maintained between the SJE experiments and numerical simulations. Table 4.1 summarizes all geometrical variables.

Table 4.1 SJE Geometrical Parameters

Parameter	Value
SJA Orifice and Cavity Radius, R (mm)	40
SJA Wall Thickness, tt (mm)	2.5
SJE Shroud Radius, R_S (mm)	53.5
SJE Shroud Thickness, TT (mm)	3.2
SJE Shroud Length, Le (mm)	400
Piston Oscillation Amplitude, Sa (mm)	52
Gap between the Shroud and the Actuator, G (mm)	11
Tank Radius, R_T (mm)	500
Tank Height, H (mm)	1000

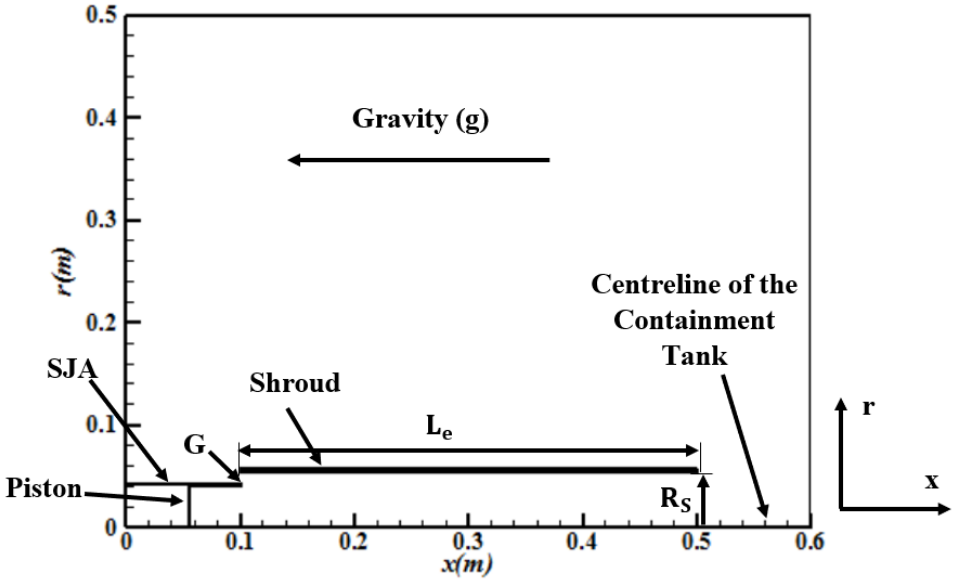

Figure 4.2 Geometric Information for the SJE Solution Domain

4.2.2 Initial Grid

The shape of the calculation domain is rectangular, so a structured quadrilateral mesh with clustered grid lines are created using ANSYS Workbench meshing option. The initial number of elements used for this mesh is 86374 grid points. The average aspect ratio for this model is approximately 1.8. The ideal aspect ratio is one, so this aspect ratio value is considered to be high. The model has a very refined mesh around the walls, the primary inlet, the secondary inlet and inside the tube. However, the mesh gradually becomes coarser closer to the containment tank walls or following the r-axis since the velocity gradients are small in this region. This is the main reason for the relatively high aspect ratio.

4.2.3 Boundary & Initial Conditions

Figure 4.3 shows the boundary conditions (BCs) that are used for this model. The walls and the piston face of the SJA, the shroud, and the tank walls are all modeled as no-slip walls. The right side being the exit of the shroud is given as a pressure outlet. Since it is open to the atmosphere, it has a zero-gauge pressure. The backflow turbulent intensity and the backflow turbulent viscosity ratio for the pressure outlet are set to 5 % and 10, respectively. The centreline is specified as an axis. The piston face is modeled as a dynamic mesh using the height-based layering-mesh option with a split factor and a collapsing factor of 0.4 and 0.2, respectively. The boundary condition along the line that represents the piston is taken to be a rigid body type. The dynamic mesh is moved periodically using the User Defined Function (UDF) given in Appendix E. The UDF is compiled and hooked in Fluent to the dynamic mesh profile. The piston velocity is represented using the sinusoidal function given in Equation 4.1.

$$V_{p(t)} = V_A \sin(2\pi f t) \qquad \textbf{(4.1)}$$

It is important to mention that the time step size, that is specified in the UDF file and in the Fluent settings, is required to be less than the time taken by the piston to cross one cell. This time is smallest when the piston velocity is at its maximum value hence the required condition is represented by Equation 4.2.

$$Time\ Step\ Size\ (\Delta t) < \frac{One\ Cell\ Height\ (\Delta x)}{Piston\ Velocity\ Amplitude\ (V_A)} \qquad \textbf{(4.2)}$$

Based on the existing mesh, the cell height within the dynamic mesh settings is specified to be 0.333 mm. Also, the operating density must be specified to be zero to avoid the inclusion of a false averaged density due to the inclusion of air in the computational domain [74].

The implicit Volume of Fluid (VOF) Eulerian formulation is used to account for the water free surface and to determine if any waves appear. A volume fraction cut-off of 1×10^{-6} is used. Also, the "sharp" type is used for the interference modeling. Figure 4.3 shows the water-air interface location. The solution is initialized with the Hybrid initialization method in Fluent. After initializing the solution, the temperature for the whole domain is set to be equal to the room temperature, taken to be 22℃.

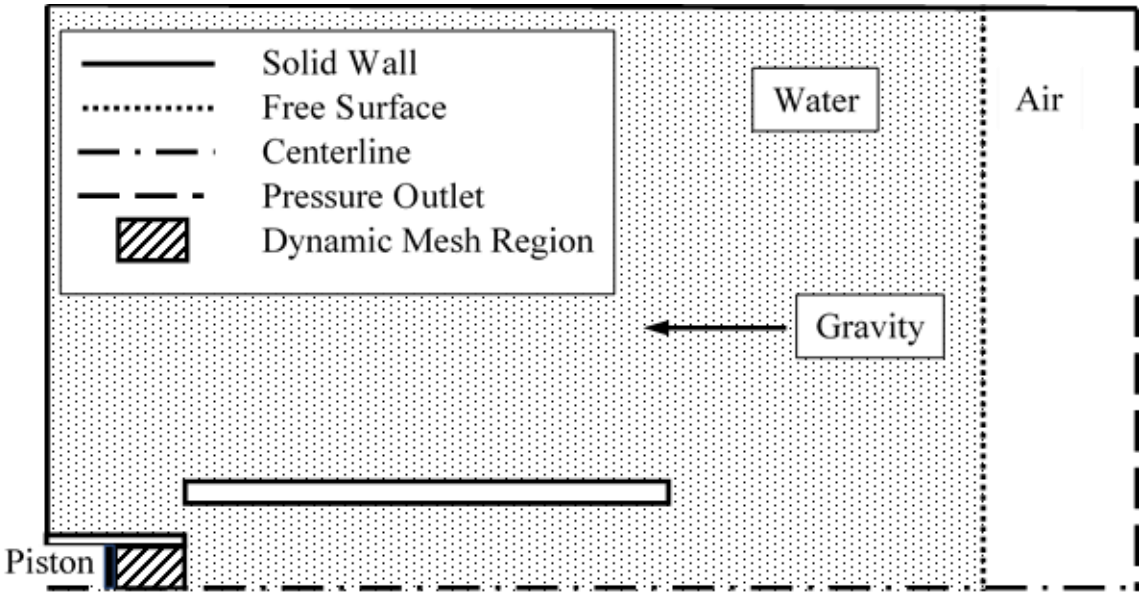

Figure 4.3 SJE Numerical Model Boundary Conditions

4.2.4 Turbulence Model

To improve the new SJE model, a search was conducted for a better turbulence model. As indicated in the turbulence modelling literature review in Appendix F, the Shear Stress Transport (SST) $k-\omega$ turbulence model has been used in aerodynamic high-speed jet applications. Generally, the $k-\varepsilon$ model gives similar results to the $k-\omega$ model except for the flow regions near the walls, where the boundary layers exist and the $k-\omega$ model is superior. This realization led to the development of the shear stress transport (SST) $k-\omega$ model, which is a combination of the $k-\omega$ and the $k-\varepsilon$ model. As described by Menter et al. [75], the standard $k-\varepsilon$ model applies far from the wall region, and the $k-\varepsilon$ model transforms into the $k-\omega$ model near the wall region. A complete turbulence validation analysis with a range of models including unsteady Reynolds averaged Navier-Stokes (URANS), direct numerical simulation (DNS) and large eddy simulation (LES) in both 2-D and 3-D simulations was conducted by Gatski and Rumsey

in 2004 [76]. It was concluded that the SST model works the best among the URANS models in representing the synthetic jet flow into quiescent air and a turbulent cross flow. For this reason, it is selected as the current turbulence model.

4.2.5 Equations & Solver Details

Seven equations need to be solved for the improved numerical model: continuity, x-velocity, r-velocity, energy, k, omega and volume fraction. The equations can be found in Fluent's theory guide [77]. Since the SJE flow is incompressible, the pressure-based solver is selected for the solution of the transient, axisymmetric set of equations. The value of the gravitational acceleration is set of 9.81 m/s^2 and directed in the negative x-direction. The energy equation is enabled in order to give a better estimate of the energy losses.

The segregated solution method with a second order implicit transient formulation is used as the solution algorithm. The pressure-implicit with a splitting of operators (PISO) scheme is used for the pressure-velocity coupling. The Green-Gauss Cell-Based scheme is used for the spatial discretization gradient. PRESTO! is used as the pressure spatial discretization scheme. QUICK is used for the momentum spatial discretization scheme as it speeds up the momentum convergence. Also, compressive is used for the volume fraction discretization scheme. The compressive scheme is a second-order reconstruction scheme based on the slope limiter. The framework of the compressive scheme is described as follows,

$$\emptyset_f = \emptyset_d + \beta \nabla \emptyset_d \qquad (4.3)$$

where, $\emptyset_f$ is the face VOF value, $\emptyset_d$ is the donor cell VOF value, β is the slope limiter, and $\nabla\emptyset_d$ is the donor cell VOF gradient value. The slope limiter β value for the compressive scheme is equal to 2 [74]. The second order upwind scheme is used for the turbulent kinetic energy, the specific dissipation rate, and energy. Table 4.2 summarizes the under-relaxation factor used for each variable. The relative normalized convergence criterion is used for this simulation. All the equations are solved using 1×10^{-3} convergence criteria except for energy and continuity, where 1×10^{-6} is applied.

Table 4.2 Under-Relaxation Factor for Each Variable

Variable	Under-Relaxation Factor
Pressure	0.3
Density	1
Body Forces	1
Momentum	0.7
Volume Fraction	0.5
Turbulent Kinetic Energy	0.8
Specific Dissipation Rate	0.8
Turbulent Viscosity	1
Energy	1

This model is simulated using the commercial CFD package, ANSYS Fluent 17.0. This simulation is run using the Double Precision option in order minimize any round-off errors. The Parallel option is selected with 12 processes in order to reduce computational time. The computer used to run this simulation has an ASUS X99-M WS motherboard with an Intel Xeon CPU E5-1650 v3 running at 4.2 GHz with 64 GB DDR RAM at 2400 MHz. Although not used in this study, the computer has an NVIDIA Tesla K40 GPU

computing processor with 2880 CUDA cores capable of 4.29 Tflops and onboard memory of 12 GB GDDR5. Microsoft Windows 10 Pro is used as the operating system.

4.2.6 Grid Independence Study

Numerical errors occur when the governing flow equations representing values which are continuous in time and space, are modeled as algebraic expressions in a discrete domain of space and time [78]. This is referred to as a discretization error, which can occur due to an improper grid size or timestep size. This section discusses details for the grid independence studies that is implemented. It is known that the more grid points used, the more accurate the numerical solution would be. On the other hand, addition of extra grid points require more computer CPU time and memory without achieving any additional significant or needed accuracy. Also, the distribution of grid points is important by clustering more cells in regions where high velocity gradients are expected, as was shown in the initial grid section. Thus, improper grid point distribution could result in poor results or longer time for the simulation to converge.

A grid convergence study is conducted by obtaining the solution for a case with a set number of grids, then doubling the number of grid points and examining how the quantities associated with the flow change. The quantities compared in this study are the period-averaged volume flow rate and the axial velocity components at two critical points within the flow domain. The selected two points are one located on the secondary inlet plane at the mid-point (y/d = 0.61) and the other one located on the jet centerline one actuator-radius from the actuator exit, as presented in Figure 4.4. These two points are selected for the grid independence study because the improved numerical model is to be compared with the simplified numerical model on middle of the secondary plane inlet.

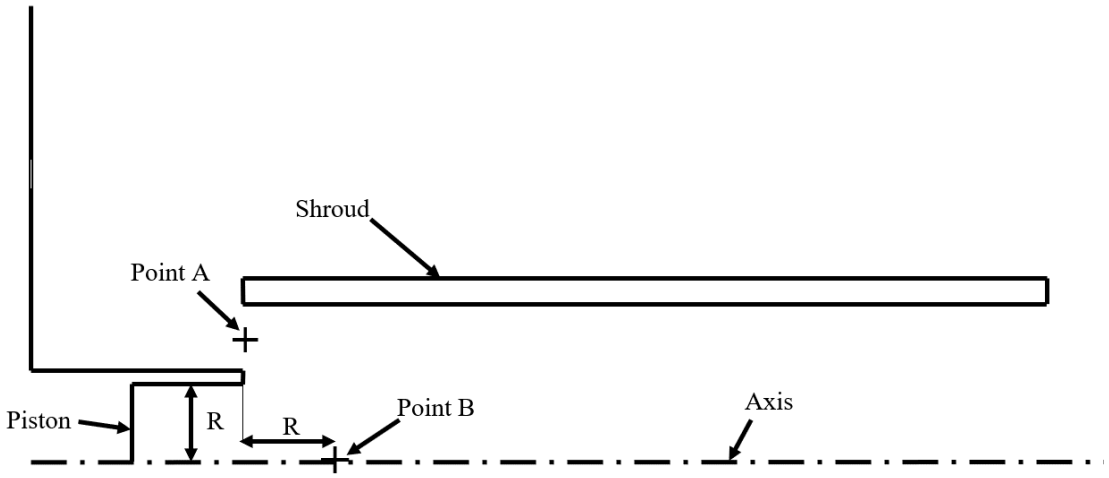

Figure 4.4 The Selected Two Points to Determine the Axial Velocity Convergence within the Grid Refinement Study

The original grid included 86374 grid points. The grid is then refined, only along the r-axis to 129860 grid points, because that is where the high-velocity gradients are located and where the vortices are developed. The error percentage for the period-averaged volume flow rate between the two meshes is approximately 0.7 %, which is considered negligible. However, the axial velocity profile at point B, in Figure 4.6, for the two meshes appears significantly different. Thus, the mesh is further refined. This time, the mesh is refined in both, x-axis and r-axis, which results in 193405 grid points. It is noticed that the period-averaged volume flow rate for the refined mesh in both axes is identical to the one generated from the refined mesh in the r-axis. Also, the velocity profiles in point A and point B, as indicated in Figure 4.4, are similar as shown in Figures 4.5 and 4.6.

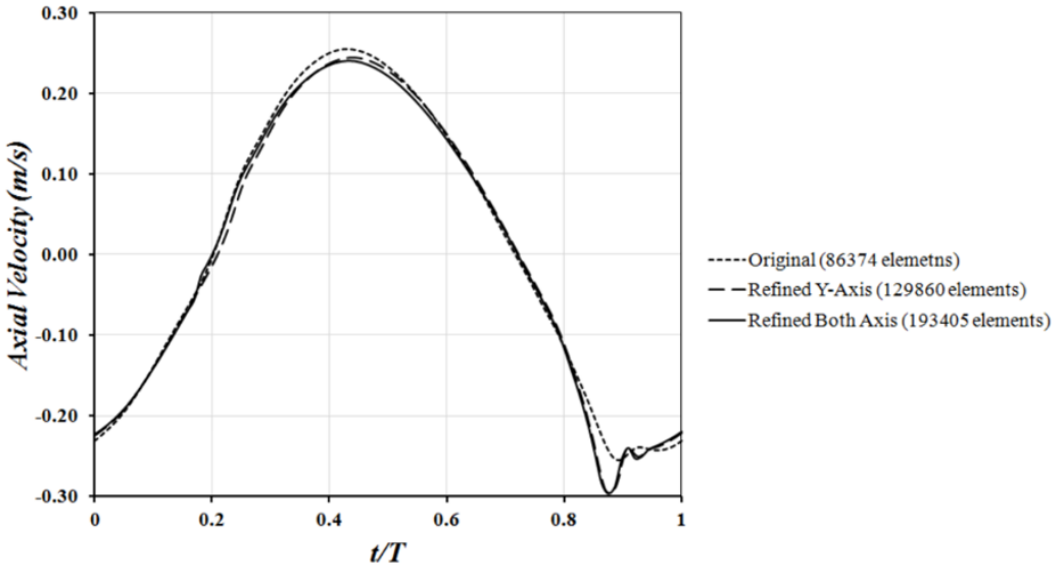

Figure 4.5 Grid Refinement Convergence Study for Point A

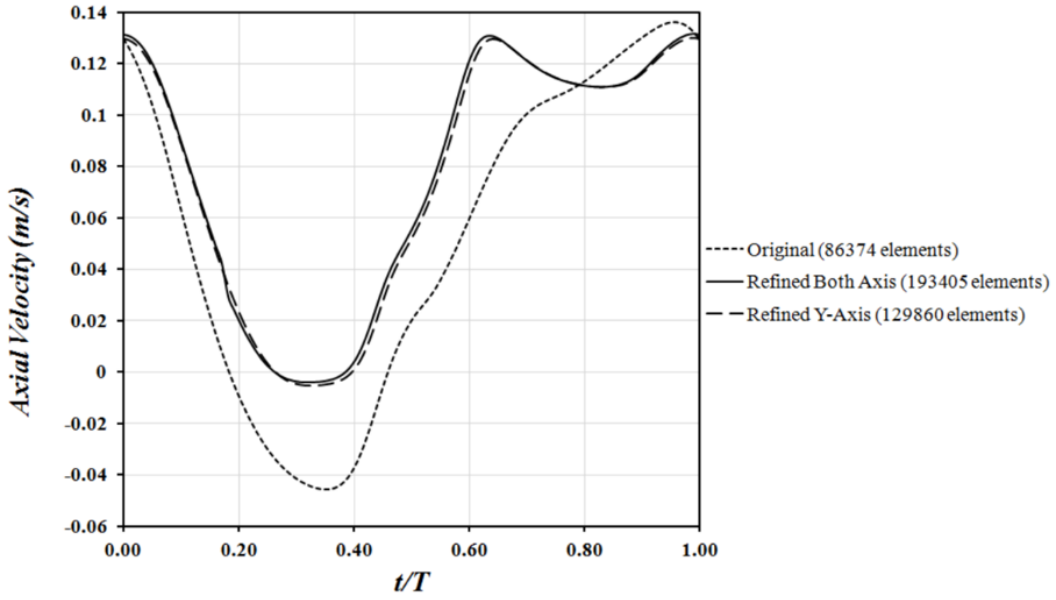

Figure 4.6 Grid Refinement Convergence Study for Point B

4.2.7 Time-Step Independence Study

Improper time step size will either cause the solution to be unstable or give poor results. As with the grid size, the required time step size must be determined by comparing results for successively smaller/larger time step sizes. For this study, the axial velocity at four different points is compared for two different time step sizes. The four points analyzed are shown in Figure 4.7. Two points are analyzed at an axial distance of one diameter away from the actuator's outlet: one along the axis and the other one in the middle of the gap between the shroud and the actuator's wall. The other two points are analyzed at the same location as the first two points, but they are located one and a half diameter away from the actuator's outlet. These four points are selected because the flow is expected to be developed in those regions, thus, the axial velocities at those four points will be the base of comparison later in this study.

Initially, the solution is obtained by running the simulation with a 0.001s time step size. Since the period for this study is equal to 1.769 seconds, as specified from the optimum conditions, the time steps per cycle (TSPC) is equal to 1769. The time step size is then reduced to 0.0005s with 3538 TSPC. Reducing the time step size does not change either the axial velocity significantly at any of the four points or the period-averaged volume flow rate at the shroud exit. The axial velocity results at the two different time step sizes are shown in Figures 4.8, 4.9, 4.10 and 4.11. Table 4.3 summarizes the percentage error between the two different time steps at each of the previously discussed points. The highest percentage error value obtained is equal to approximately 3 %, which is considered to be negligible for the current purpose of this study. Furthermore, the same time independence study is conducted using the two points used in the grid independence study.

The largest difference in the period-mean volume flowrate difference is approximately 3 %, while that for the axial velocity component is about 11 %.

To conclude, based on the grid independence and the time step independence studies, the final grid used the refined mesh along the r-axis, which contains 129860 grid points, is selected. The time step selected for use is 0.001 s. It is also important to note that the resulting average value of y+ near the walls is approximately equal to 2.8.

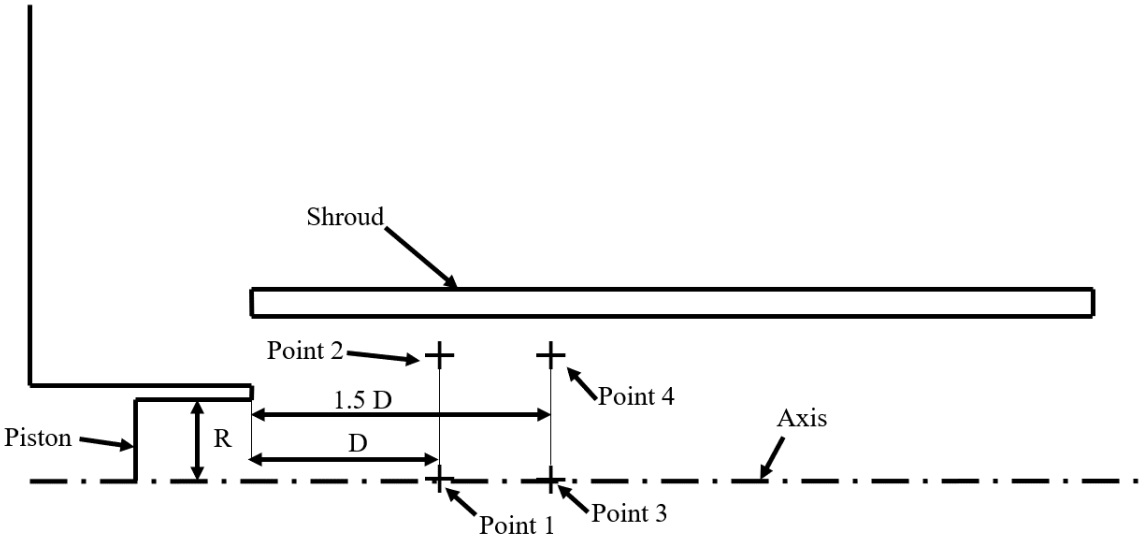

Figure 4.7 The Selected Four Points to Determine the Axial Velocity Convergence within the Time Step Independence Study

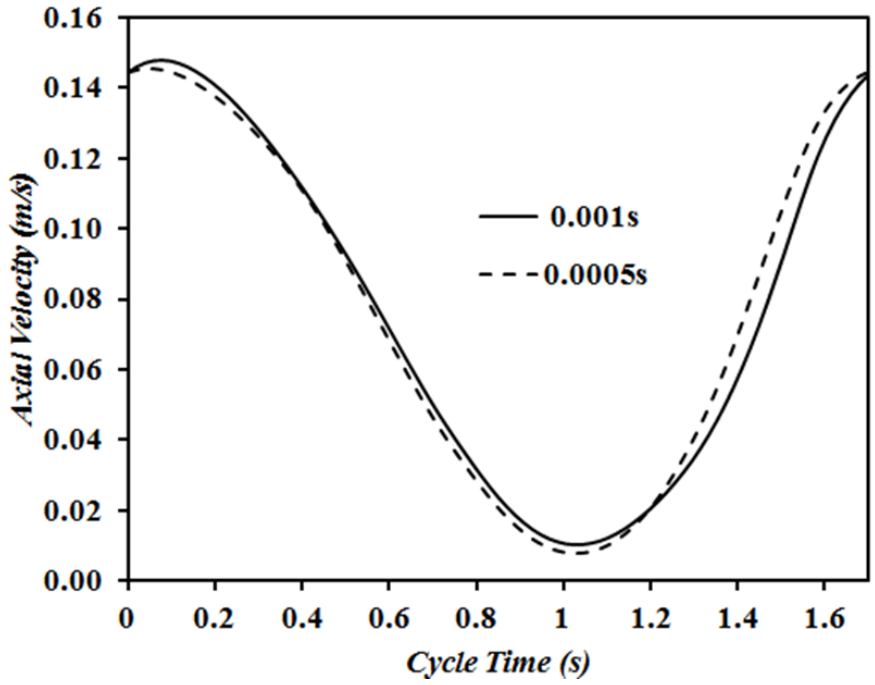

Figure 4.8 Axial Velocity at One Diameter away from the Actuator's Outlet along the Axis for Two Different Time Step Sizes

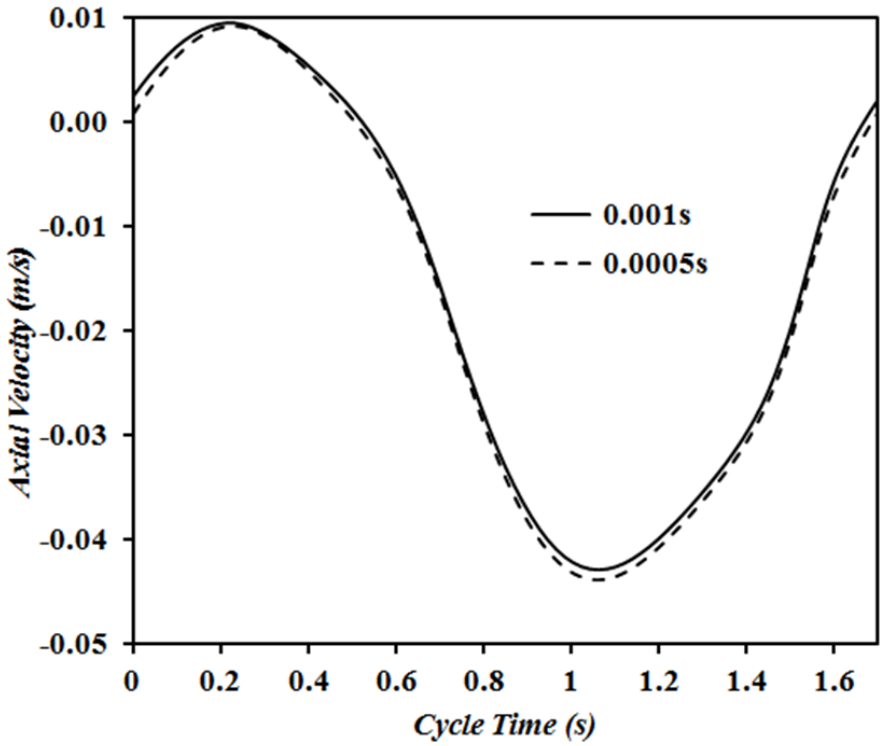

Figure 4.9 Axial Velocity at One Diameter away from the Actuator's Outlet in the Middle Distance between the Shroud and the Actuator's wall for Two Different Time Step Sizes

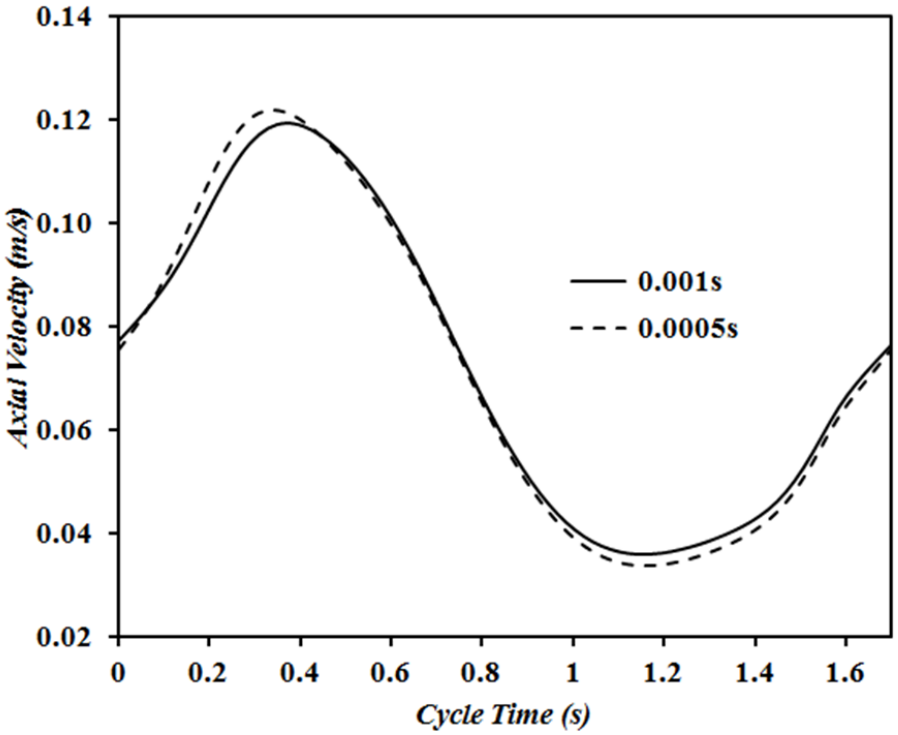

Figure 4.10 Axial Velocity at One and a Half Diameter away from the Actuator's Outlet along the Axis for Two Different Time Step Sizes

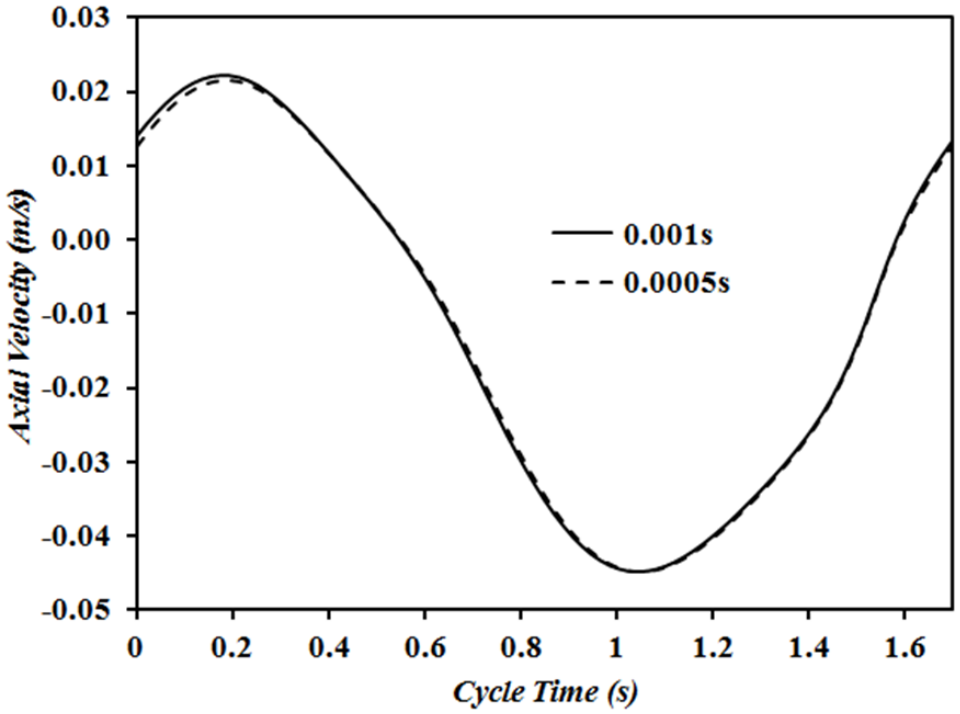

Figure 4.11 Axial Velocity at One Diameter and a Half away from the Actuator's Outlet in the Middle Distance between the Shroud and the Actuator's wall for Two Different Time Step Sizes

Table 4.3 The Error Percentage Difference between the 0.001 s and 0.0005 s Time Step Sizes for the Axial Velocity and the Period-Averaged Volume Flow Rate at the Specified Points

Variable Analyzed at Each Point Location	Error Percentage Difference
Axial Velocity at D away from the Actuator Outlet Along the Axis	0.8%
Axial Velocity at D away from the Actuator Outlet in the Middle Distance between the Shroud and the Actuator's Wall	0.5%
Axial Velocity at 1.5 D away from the Actuator Outlet Along the Axis	1.2%
Axial Velocity at 1.5 D away from the Actuator Outlet in the Middle Distance between the Shroud and the Actuator's Wall	0.1%
Period-Averaged Volume Flow Rate at the Exit of the Shroud	3.0%

Chapter 5

RESULTS AND DISCUSSION

This chapter begins by comparing the cycle-averaged volume flow rate for the experiments, the improved CFD numerical method and the simplified CFD numerical method developed by Lin. An evaluation of the simplified model assumptions is then made. The mean flow fields obtained from the phase averaged PIV experiments, their U_{rms} values and the results from the improved CFD simulations at three representative dimensionless times throughout the cycle are then analyzed. PIV instantaneous velocity fields selected from those used to determine the phase-average values at one dimensionless time within the cycle (at t/T = 0.8) are also presented to highlight the complexity of the flow field. These also are shown to vary from cycle-to-cycle and the variations are also explained. The longitudinal profiles of the axial velocity component for the experimental and the improved numerical flow fields at certain radii are discussed as well. Discussion of the axial velocity profiles across the shroud's diameter at selected axial positions are also provided for both the experimental and the improved CFD numerical methods. The last section is devoted to comparing the axial velocity at certain points of interest, for the experiments and the improved CFD numerical model.

5.1 Comparison of the Improved and Simplified Numerical Models and Experiments

The results are considered in two sections. The first section deals with a direct comparison of the ability of the improved and simplified models to accurately predict the phase-averaged volume flowrate variation throughout one cycle and its mean value. This

is a measure of the pumping capability of the device. This section also involves using the improved numerical model to evaluate the assumptions made in the simplified model. The second section is a detailed comparison of the improved numerical model and the experimentally obtained flow fields.

5.1.1 Comparison of Phase-Averaged Volume Flow Rate Predictions with Experiments

For purposes of comparison, the phase-averaged volume flow rate at x/d = 1.75 is obtained from the experimental method, the improved CFD numerical model and the simplified numerical model. For the improved numerical method and the simplified numerical method, the average volume flow rate results are obtained directly from Fluent for the last cycle of the converged periodic solution. The average volume flow rate at each dimensionless time within the cycle is given by Equation 5.1,

$$Q = 2\pi \int u\, r\, dr \qquad \textit{(5.1)}$$

where, Q is the volume flow rate, u is the axial velocity and r is the radius.

The experimental values are obtained by integrating the area under the velocity × radius versus radius curves using the trapezoidal rule. Due to the asymmetry, the left and the right sides of those curves are integrated separately, multiplied by 2π, and the average value from the two sides obtained.

Figure 5.1 shows the phase-averaged volume flow rate versus the dimensionless time within the cycle for the three models. The curve for the experimental phase-averaged flow rate throughout the cycle is close to and has the same trend as the improved CFD

numerical method results. However, as expected, the results obtained from the simplified numerical CFD method are considerably different than the improved numerical results and the experimental results. The mean cycle-averaged volume flow rate for the experimental method, the improved CFD numerical method and the simplified numerical method are $6.94\times 10^{-5}\,m^3/s$, $7.95\times 10^{-5}\,m^3/s$ and $55.1\times 10^{-5}\,m^3/s$, respectively. The difference between the mean of the experimental results and the mean of the improved numerical CFD results is approximately 12 %, whereas the percentage difference between the mean of the experimental method results and the mean of the simplified numerical method is approximately 94 %. The percentage difference is calculated based on the values from the experimental method. The incorrect assumptions in simplifying Lin's numerical method are likely the reasons for the large difference between the simplified numerical model and the improved numerical model and the experiment.

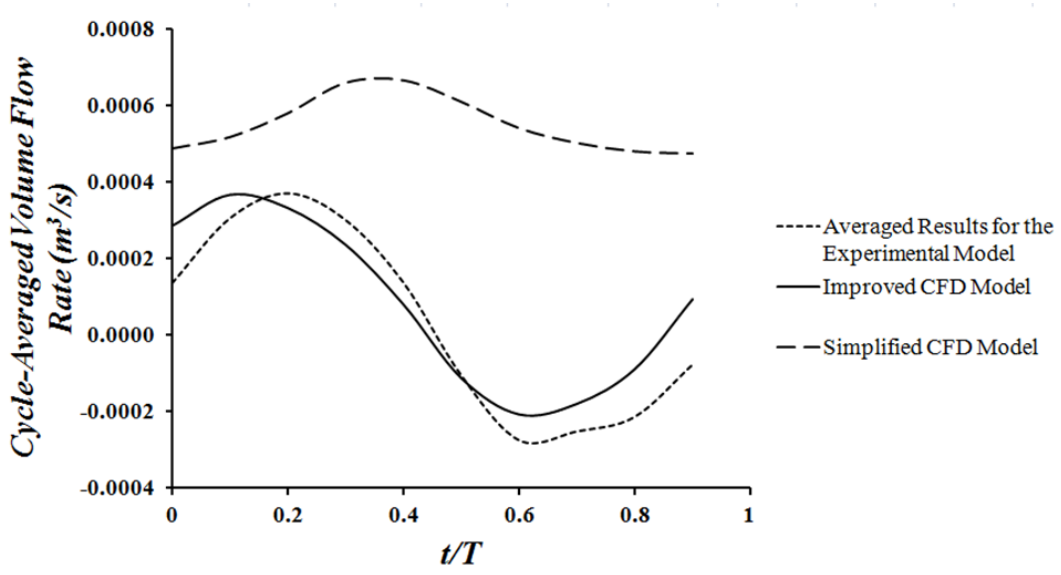

Figure 5.1 A Phase-Averaged Volume Flow Rate Comparison between the Experimental Method, the Improved CFD Numerical Model and the Simplified Numerical Model at x/d=1.75

5.1.2 Evaluation of Lin's Simplified Model Assumptions

As explained in Section 4.1, Lin assumed a constant pressure profile across the secondary flow inlet and a constant velocity profile across the exit of the orifice.

Figures 5.2, 5.3 and 5.4 show the axial component of the velocity across the exit of the orifice at t/T = 0.2, 0.5 and 0.8, respectively for both the simplified and the improved numerical models. It can be clearly seen that the assumption of the uniform velocity variation over the plane is not adequate and does not represent the motion properly.

Figure 5.5 shows the total pressure variation across the secondary flow inlet obtained from the improved numerical model for the same three dimensionless times during the cycle. Also, for comparison purposes, the simplified model assumption of a zero value across the plane is included. The assumption that the total pressure across the secondary flow inlet is zero only applies during a short period of the cycle time, and for the majority of the other times, it is less. This is expected due to the energy losses in the flow approaching the plane from the surroundings. All of the above-mentioned reasons contribute to the significant difference observed between the simplified numerical model results and the improved numerical model results.

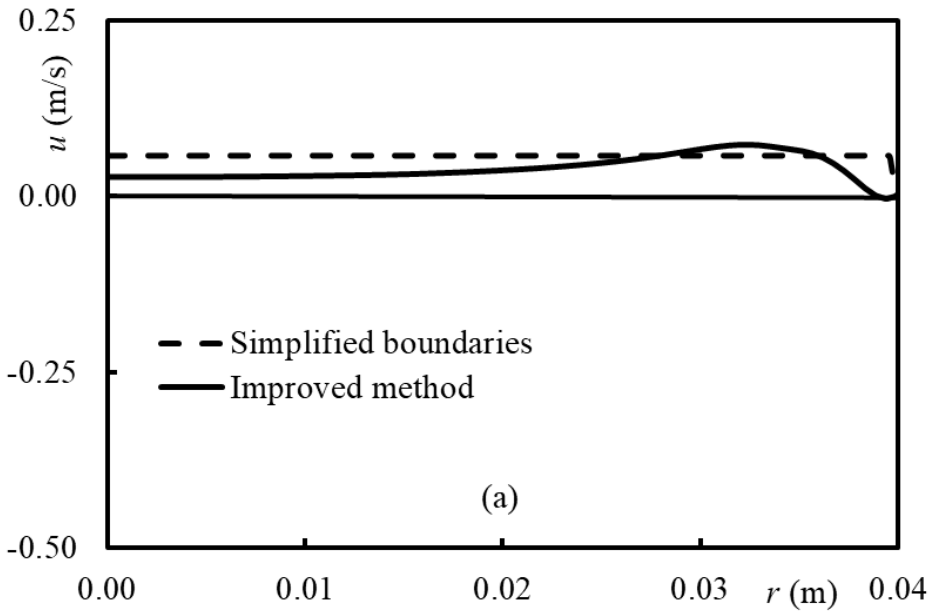

Figure 5.2 Axial Velocity Variation across the Exit of the Orifice at t/T=0.2

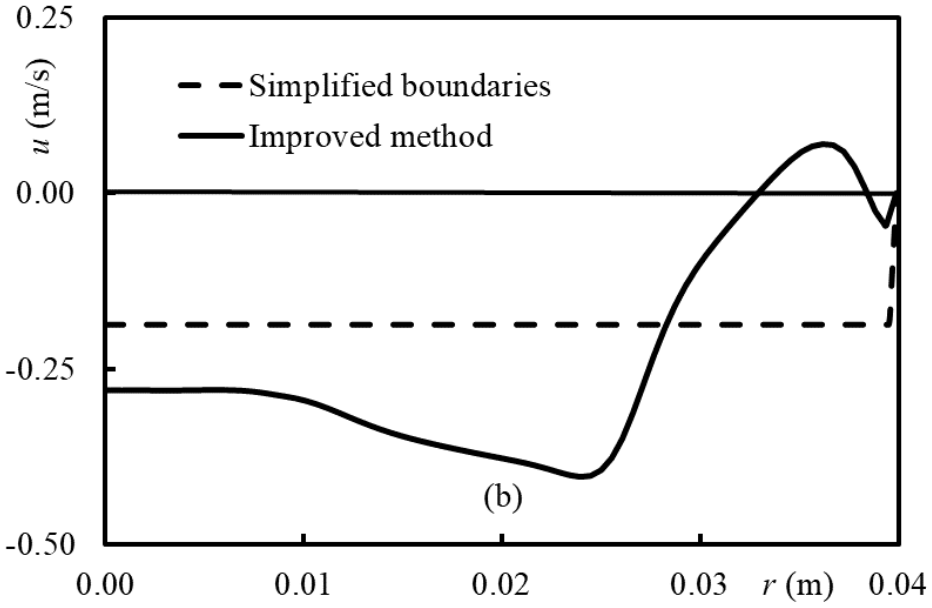

Figure 5.3 Axial Velocity Variation across the Exit of the Orifice at t/T=0.5

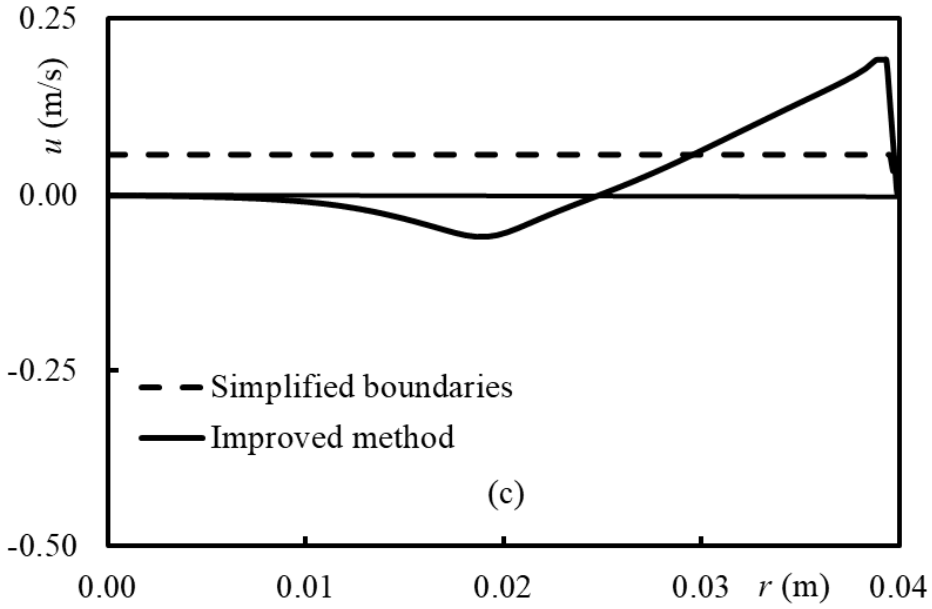

Figure 5.4 Axial Velocity Variation across the Exit of the Orifice at t/T=0.8

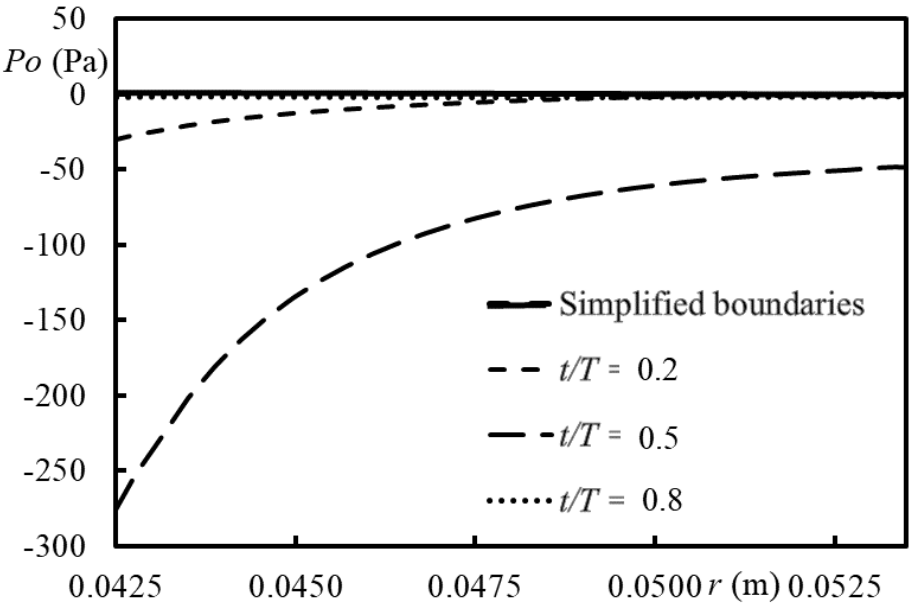

Figure 5.5 Total Pressure Variation on the Secondary Flow Inlet Plane at t/T=0.2, t/T=0.5 and t/T=0.8

5.2 Detailed Comparison of the Improved Numerical Model and Experimental Results

In Section 5.1.2, it is concluded that the average volume flow rate results for the simplified method are not accurate due to the assumptions made by Lin. Thus, the rest of the thesis will only compare results between the improved numerical model and the experiments and analyze them in detail. This section begins by analyzing in detail the mean flow fields for the experiments and the improved numerical model. Also, the cycle-to-cycle variations and the U_{rms} contours are then explained. The longitudinal and the radial variations of axial velocity are presented. Finally, the axial velocity variation over cycle at certain points of interest in the flow field are presented and evaluated.

5.2.1 Mean Flow Field Analysis

This section presents the phase-averaged velocity fields obtained from the experiments at dimensionless times within the cycle and the velocity fields at corresponding dimensionless time from the improved CFD numerical simulations. Contours of the root-mean-square of the velocity values, U_{rms}, at corresponding times are also discussed. Results will only be considered at three dimensionless times; $t/T = 0.2$, 0.5 and 0.8. The remainder of the results are presented in Appendix G. The piston location and its direction of motion at these dimensionless times are summarized in Figure 5.6, where the arrow represents the direction of the velocity or piston movement direction.

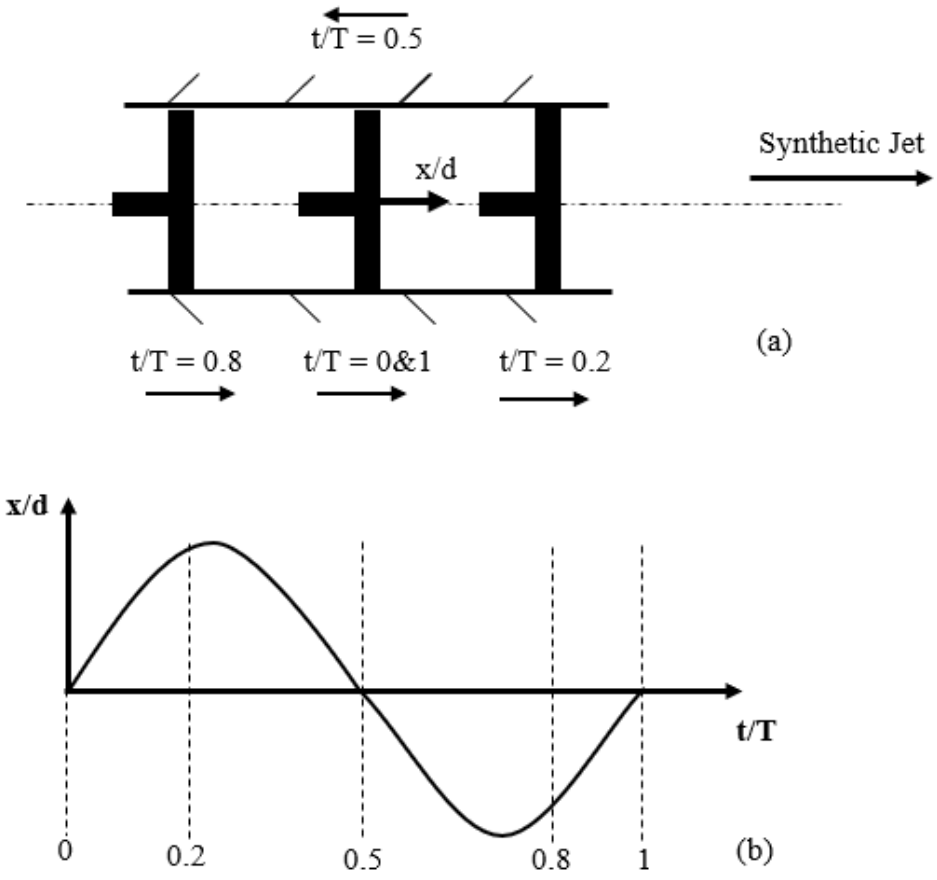

Figure 5.6 Specified Dimensionless Times within a Cycle a) Piston Position and Direction, b) Dimensionless Times

The flow fields for the phase-averaged experimental velocity vectors, numerical velocity vectors and contours of the root-mean square values of the velocity vector magnitudes are presented in Figures 5.7, 5.8 and 5.9 respectively. The white box in the experimental flow fields represent the actuator cylinder in which the piston travels. Since the actuator is made of aluminum, it is not possible to capture the internal velocity field, unlike in the case of the CFD. The values of $^{x}/_{d} = 0$ and $^{r}/_{d} = 0$ represent the exit of the actuator (or the shroud inlet) and the centreline of the piston, respectively. The

experimental data (Figures 5.7a, 5.8a and 5.9a) and the computational data (Figures 5.7b, 5.8b 5.9b) show the entire flow field. Note, however, that the numerical model assumes an axisymmetric boundary condition, so half of the flow field is initially modelled and then mirrored across the x-axis. For the experimental and the numerical data, the flow field is captured only inside the shroud, so the boundaries shown represent the inside walls of the shroud. It is important to note that the mean flow fields for all experimental cases are based on the phase-averaged velocity vectors over 1500 cycles, while for the numerical cases, the flow field is the periodically steady solution for the last calculated cycle (cycle number 124).

The results in this section correspond to each of the three dimensionless times within a cycle. Each of the following three paragraphs discuss the experimental velocity fields and the corresponding U_{rms} values as well as the improved numerical flow fields for one of these three dimensionless times. The last two paragraphs in this section are devoted to discussing the general behavior of the flow field over all dimensionless times within a cycle for both the experimental and the improved numerical flow fields, respectively.

In Figures 5.7a and 5.7b, corresponding to t/T = 0.2, the velocity vectors for both the experimental and the numerical cases show very different velocity patterns. The flow field for the experimental case in Figure 5.7a is more uniform at the exit of the actuator orifice compared to the numerical case. After x/d = 0.3, the velocity vectors for the experimental case start to deviate towards the walls, which results in larger magnitudes of the velocity vectors away from the axis. A small recirculation is detected around the edge of the actuator's cavity. Generally, the phase-averaged velocity field is symmetric about the centreline. However, no significant vortex is detected for the experimental case at this

dimensionless time. For the numerical case, shown in Figure 5.7b, one vortex is detected at the exit of the actuator advancing along the centre of the piston. This is called a piston vortex and has also been observed by Allen and Auvity [48]. In addition, as the flow being entrained from the containment tank approaches the secondary flow inlet it strikes the outer wall of the SJA and divides into two streams. One stream is seen to enter the shroud and form a vortex ring, also known as the primary vortex which was also observed by Allen and Auvity [48]. The primary and the piston vortices seem to combine to direct the entrained flow between them towards the axis and reduce the velocities near the inner wall of the shroud. The secondary inlet flow, in both the experimental and the numerical data, seems to be directed out of the shroud. This is expected to occur since t/T = 0.2 is near the end of the ejection phase. The U_{rms} contours are presented in Figure 5.7c. The highest U_{rms} values are located at the exit of the actuator and on the secondary flow inlet plane, and the magnitudes decrease gradually further away from the actuator outlet. The ratio of the RMS axial velocity and the velocity amplitude (U_{rms} /V_A), ranges from 13 % to 20 %. This is considered to be very high compared to the acceptable uncertainty of 10 %, as explained in Appendix D.

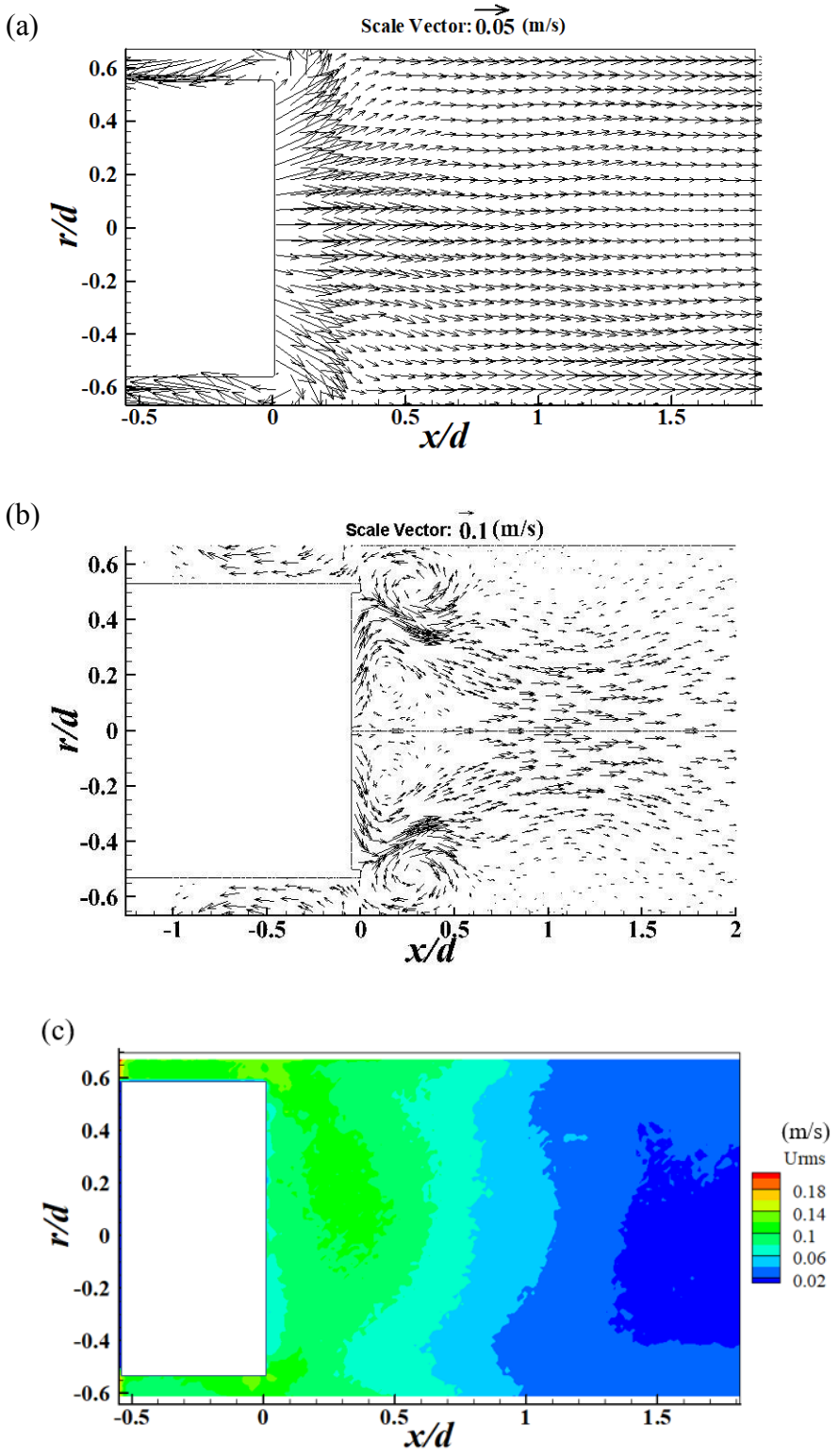

Figure 5.7 Velocity Field Vectors Obtained at t/T = 0.2 from (a) Phase-Averaging, (b) Improved CFD Simulation, (c) U_{rms} Contours

In Figures 5.8a and 5.8b, corresponding to t/T = 0.5, the experimental and the numerical flow fields are seen to have some similarities. Both flow fields show a large recirculation at the edge of the orifice exit (primary vortex). For the experimental case in Figure 5.8a, at x/d > 0.5, the velocity vectors are directed uniformly towards the negative x-direction and the flow is pulled towards the actuator cavity. Also, it is shown that the magnitude of the velocity vectors is greater along the centreline and decrease gradually towards the shroud walls. Along the centerline, the flow that is directed into the cavity is decelerated through an interaction with the vortex at the edge of the cavity and forms a stagnation point at approximately x/d = 0.5. Also, another stagnation point is detected at x/d = 0.25, due to the entrained secondary inlet flow forming a radially inward jet that splits into two streams in the axis. One stream is directed towards the actuator, while the other flows away from the actuator. For the numerical case in Figure 5.8b, as the flow is entrained from the containment tank into the secondary flow inlet it hits the outer wall of the SJA and is divided into two flows. One flow enters the shroud and forms a vortex (primary vortex). This is similar to the previous dimensionless time however, the large primary vortex ring inside the shroud covers the entire inner radius of the shroud and causes disturbances (large scale flow features) in the flow field further away from the actuator inside the shroud. The piston vortex travels into the actuator. A stagnation point is detected near x/d = 0.2, due to the interaction between the primary vortex and the piston vortex inside the actuator. The secondary flow for both the experimental and the numerical results seems to be directed into the shroud. This is expected to occur since the t/T = 0.5 is considered to be in the middle of the suction phase. The U_{rms} contours in Figure 5.8c show greater magnitudes at the exit of the actuator and on the secondary flow inlet plane. Also,

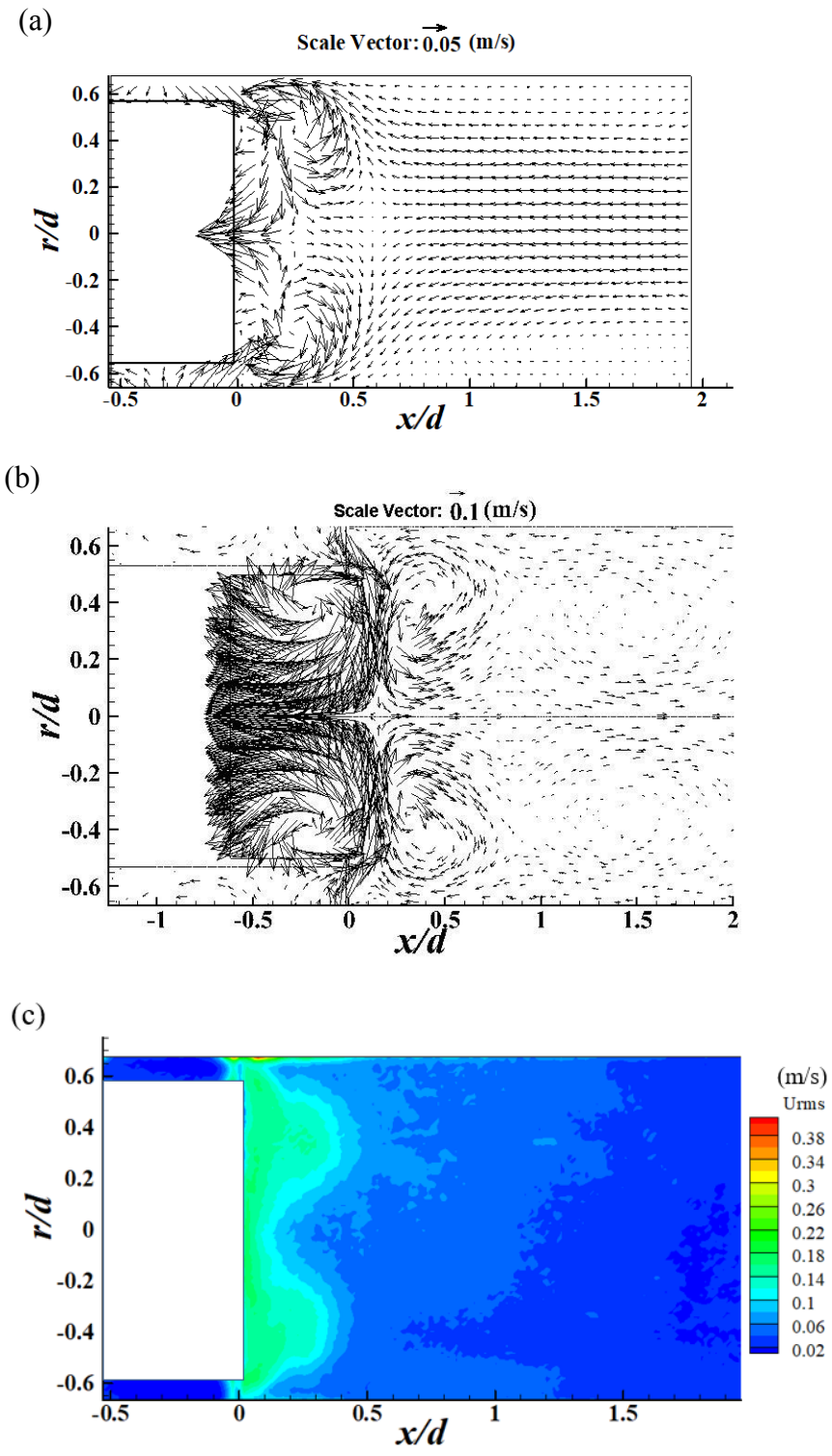

Figure 5.8 Velocity Field Vectors Obtained at t/T = 0.5 from (a) Phase-Averaging, (b) Improved CFD Simulation, (c) U_{rms} Contours

the U_{rms} contours seem to have the same semi-circular shape as the vortex observed at the exit of the actuator in Figure 5.8a. The ratio of the RMS axial velocity to the velocity amplitude (U_{rms} /V_A), which ranges from 16 % to 23 %, is considered to be very high compared to the acceptable uncertainty of 10 % as explained in Appendix D.

In Figures 5.9a and 5.9b, corresponding to t/T = 0.8, the flow field is similar to the one at t/T = 0.5. The primary vortex inside the shroud, for both the numerical case in Figure 5.9b and the experimental case in Figure 5.9a, seem to be moving away from the centerline and diminishing. This is more evident in a video of the transient flow fields. For the experimental case in Figure 5.9a, the primary vortex, restricts the flow far away from the actuator exit from being pulled back into the actuator. As a result of this, along the centreline, a stagnation region exists at approximately x/d = 0.75. Also, the primary vortex increases the flow out of the secondary flow inlets at x/d = 0. A stagnation point is detected at around x/d = 0.15 along the centerline as the radially inward flow in that region is divided into two streams. One stream gets entrained with the primary vortex ring and flows away from the actuator while the other is pulled into the actuator. The flow field at this dimensionless time is not as symmetrical as the previous dimensionless times presented in Figures 5.7a and 5.8a. The numerical data in Figure 5.9b, shows a similar pattern as the experimental case at the exit of the orifice and at the secondary flow inlet. The flows on the secondary inlet for both the experimental and the numerical data are directed out of the shroud. This is expected to occur since the t/T = 0.8 is near the beginning of the ejection phase. The large primary vortex in this case, however, appears to generate a non-uniform flow field (large scale flow structures) further away from the actuator and the stagnation point further away from the exit cannot be detected. Between the primary vortex ring and

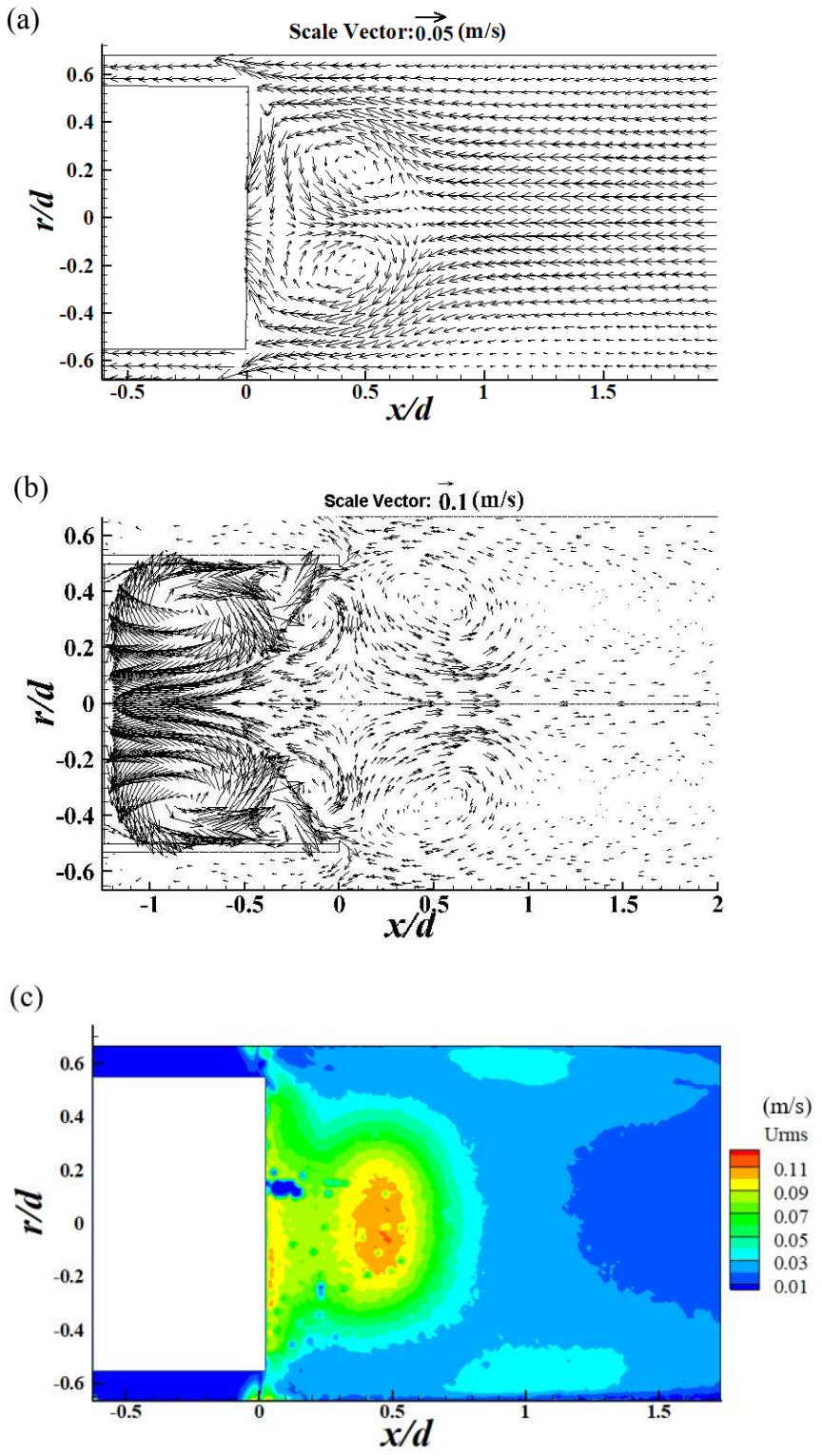

Figure 5.9 Velocity Field Vectors Obtained at t/T = 0.8 from (a) Phase-Averaging, (b) Improved CFD Simulation, (c) U_{rms} Contours

the piston vortex ring inside the actuator, a stagnation point is detected along the centerline at around x/d = 0.1. The U_{rms} contours shown in Figure 5.9c, indicates very high U_{rms} values at the exit of the actuator compared to the downstream flow. It extends to approximately x/d = 0.5 and is approximately circular in shape. This is expected due to the large vortex in the region, as shown in Figure 5.9a. The ratio of the RMS axial velocity to the velocity amplitude (U_{rms} /V_A), which ranges from 9 % to 16 %, is considered to be extremely high compared to the acceptable uncertainty of 10 %, as explained in Appendix D.

Considering all the experimental cases shown in this section and in Appendix G, during the transition from the ejection to the suction phases, primary vortex rings are formed outside the actuator exit, near the centerline. This is due to the interaction between the entrained secondary flow into the shroud and the forced flow inside the actuator. These vortex rings seem to grow during the suction phase and dissipate during the ejection phase. During the ejection phase, the flow field is more uniform and most of the velocity vectors are directed towards the shroud outlet, except the velocity vectors near the sides of the cavity, which get pulled uniformly into the secondary flow inlet. A region of saddle (stagnation) points appear on the centerline due to the interaction between the vortex rings and the flow drawn into the actuator. The presence of the primary vortex ring can explain why the velocity vectors along the centerline deviate towards the walls during the ejection phase. The stagnation point moves along the centerline during the cycle, which results in instabilities (small vortex rings) in the downstream flow field. Also, the U_{rms} values detected within the suction phases seem to be higher than the ones deteced within the

ejection phases. This can be due to the primary vortex formed in the suction phases and dissipated during the ejection phases.

Generally, considering all numerical cases, a primary vortex at the exit of the actuator is formed when the transition from the ejection to the suction phase occurs, and then diminishes during the transition from the suction to the ejection phase. The diminishing vortex moves away from the axis due to the high flow along the centerline from the actuator. Also, the majority of the flow entrained into the shroud through the secondary flow inlet is pulled into the actuator's cavity and forms a vortex. The vortex strengthens during the suction phase, and persists until a piston vortex is formed half-way through the ejection phase. The piston vortex breaks down almost instantaneously at the beginning of the suction phase and is not travelling downstream in the flow field.

5.2.2 Experimental Cycle-to-Cycle Variations

Figures 5.10 a, b and c show the instantaneous flow fields for the experimental velocity vectors at dimensionless time of t/T = 0.8 for cycles 145, 1416 and 1459, respectively. The vortex ring formed at the exit of the actuator for the instantaneous flow fields are not as symmetrical as the ones shown in the phase-averaged flow fields. Also, it can be noticed that the flow distribution and the vortices formed downstream in the flow field are significantly random and not following any specific pattern. Furthermore, the instantaneous velocity fields show a large number of small eddies that appear at various positions within the shroud. These eddies appear to be randomly generated and are likely moving with the mean flow, sometimes away from and sometimes towards the actuator exit. The significant difference between the instantaneous flow fields indicates the existence of the cycle-to-cycle variations in the experimental results. In addition, during

the experiment, a significant out-of-plane motion of the particles is indicated by the observed reduction in the cross-correlation peak in the interrogation region, particularly close to the actuator. One should note that, the vortices observed in the flow field in Figures 5.10 a, b and c are the projection of 3-D vortices on the 2-D measurement plane.

Table 5.1 summarizes the U_{rms} values, the mean axial velocities (U) and the ratio U_{rms} /U at the points of interest, where U is the local mean velocity. The acceptable uncertainty of the PIV measurements is selected to be about 10 % of the dimensional axial velocity values, as explained in Appendix D, and cannot account for these cycle-to-cycle variations. Although Figure 5.10 seems to indicate some randomness in the flow field, the extremely high values of the U_{rms} and the presence of large flow structures makes it unlikely that it is can be classified as only turbulence. These results are similar to Murugan et al. [29] who found that synthetic jets exhibit a circumferential instability that can generate a high turbulence level due to the vortex breakdown, which raises the fluctuation level compared to other jets. Rizzetta et al [23] also found that vortex breakdown generated due to the circumferential instabilities could not be captured using the 2-D simulations and 3-D simulations overcame this issue.

Fortunately, Allen and Auvity [48], observed a similar occurrence in their experiments using a piston ejecting fluid from a tube into a large container. In their case, the piston stopped at various distances from the tube exit and did not oscillate. Their results were not repeatable unless they allowed the flow to settle in the tank for about 30 minutes between runs. As that is impossible to implement in the current experiment, the cycle-to-cycle variations could be caused by the residual unsteadiness in the flow within the shroud at the end of each cycle. Thus, the detected eddies in the instantaneous flow fields can

cause an intense mixing like that caused by turbulence. Also, extremely small disturbances on the water surface, which vary from one cycle to another could result in a position error that would cause greatly different instantaneous flow fields.

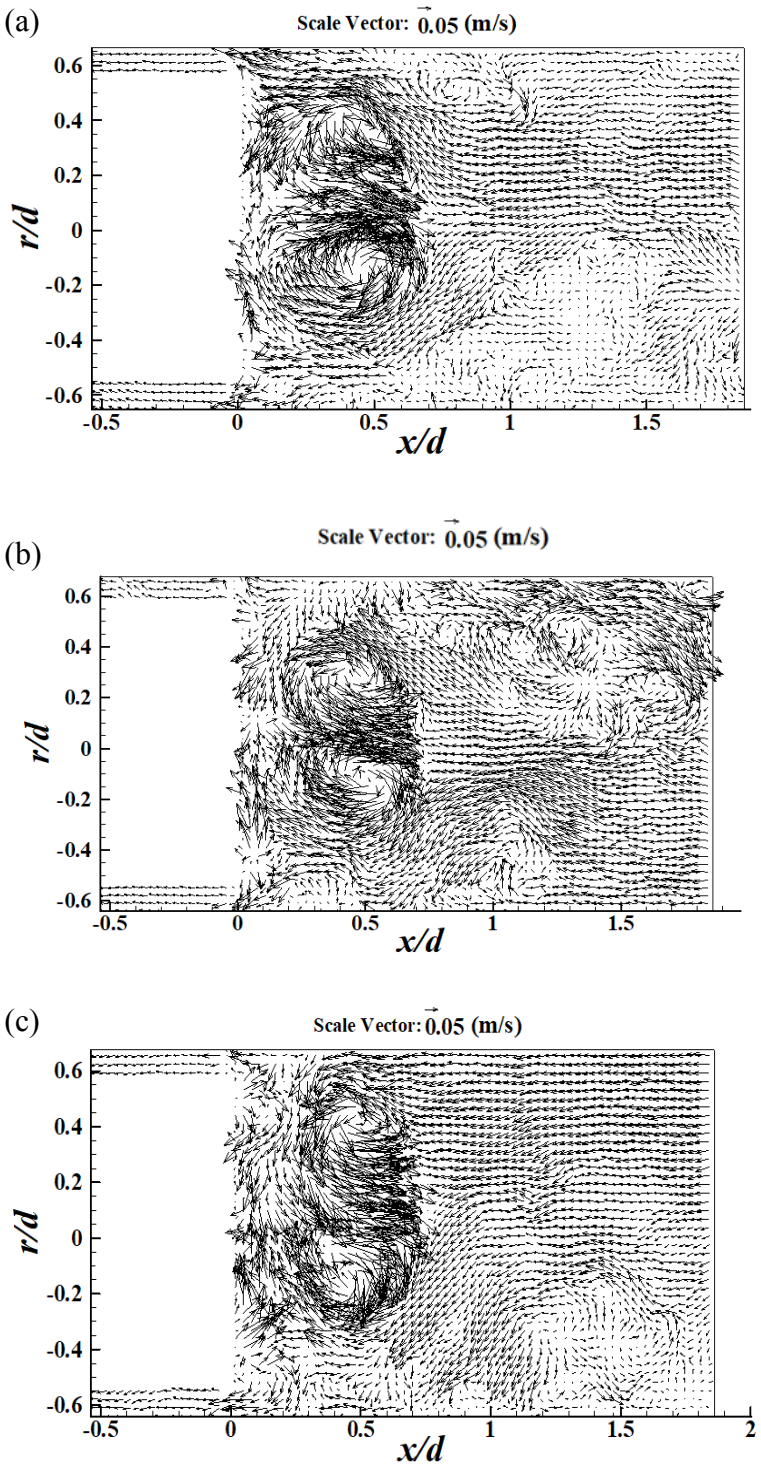

Figure 5.10 Instantaneous Flow Field at t/T=0.8 for Cycle a) 145 b) 1416 c) 1459

Table 5.1 U_{rms} / V_A at Points of Interst throughout the Cycle

		(U_{rms}/V_A) %			
Dimensionless Times at the Cycle\Points of Interest	Phase	1D Along the Axis	1.5D Along the Axis	1D Along the Middle of the Secondary Flow	1.5D Along the Middle of the Secondary Flow
0.8	Ejection Phase	16	9	14	13
0.9		17	10	15	14
0		18	11	16	15
0.1		19	12	17	16
0.2		20	13	18	17
0.3	Suction Phase	21	14	19	18
0.4		22	15	20	19
0.5		23	16	21	20
0.6		24	17	22	21
0.7		25	18	23	22

5.2.3 Longitudinal Variation of the Axial Velocity

Variation of the axial velocity component with increasing axial distance from the actuator exit at three radial positions is presented in Figures 5.11 to 5.16 inclusive. The experimental data (Figures 5.11, 5.13 and 5.15) are presented along the center of the actuator ($^{r}/_{d} = 0$), the middle of the top secondary flow inlet ($^{r}/_{d} = 0.6$), and the middle of the bottom secondary flow inlet ($^{r}/_{d} = -0.6$). Also, the acceptable dimensionless velocity ($^{u}/_{V_A}$) uncertainty for the experimental results is found to be nearly constant along the flow and is calculated to be approximately 10 % as described in Appendix D. If the magnitude of the dimensionless axial velocity ($\frac{u}{V_A}$) is greater than 0.1, the uncertainty is less than 10 % and is acceptable. The numerical data (Figures 5.12, 5.14 and 5.16) is only presented along the axis and along the center of the secondary flow inlet since the simulation is axisymmetric. The percentage difference for the rest of the thesis is measured based on the difference between the two dimensionless axial velocities multiplied by a 100, $(\frac{u1-u2}{V_A}) \times 100$.

For t/T = 0.2, the flow for the experimental case in Figure 5.11 appears to get fully developed earlier than the numerical case in Figure 5.12. The axial flow for the experimental case becomes fully developed after x/d = 1.2 along both the centre of the secondary flow inlets ($^{r}/_{d} = 0.6 \ \& \ -0.6$) and along the centerline ($^{r}/_{d} = 0$), while for the numerical case it becomes fully developed at around x/d = 4. For the numerical case, the axial velocity along the centre of the secondary flow inlet ($^{r}/_{d} = 0.6 \ \& \ -0.6$) equals the axial velocity along the axis ($^{r}/_{d} = 0$) at around x/d = 4.5, while this cannot be detected within the FOV of the experimental case. For the experimental case, the

difference between the velocity along the top secondary flow inlet ($^{r}/_{d} = 0.6$) and the along the bottom secondary flow inlet ($^{r}/_{d} = -0.6$) is very small near the jet exit, till approximately x/d = 0.6, but becomes larger, reaching a maximum value of approximately 6 %, further away from the exit, indicating that the flow field is not perfectly symmetric. After reaching the fully developed state, the percentage difference for the axial velocities along the axis ($^{r}/_{d} = 0$) between the experimental and the numerical cases is about 5 %. Also, the percentage difference between the axial velocity along the centre of the secondary flow inlet for the numerical case and the axial velocity along the centre of the averaged secondary flow inlet ($\frac{(^{r}/_{d}=0.6)+(^{r}/_{d}=-0.6)}{2}$) is approximately 8 %. The resulting dimensionless axial velocities after reaching the developed state fall within the acceptable uncertainty limit, 10 %, as explained in Appendix D.

For t/T = 0.5, the flow for the experimental case in Figure 5.13 again appears to become fully developed in a shorter distance than the numerical case in Figure 5.14. The axial flow for the experimental case becomes fully developed after x/d = 1 along both the centre of the secondary flow inlets ($^{r}/_{d} = 0.6 \,\&\, -0.6$) and along the centerline ($^{r}/_{d} = 0$). While for the numerical case, the axial flow becomes fully developed at around x/d = 3.25. For the numerical case, the axial velocity along the centre of the secondary flow inlet ($^{r}/_{d} = 0.6 \,\&\, -0.6$) equals the axial velocity along the axis ($^{r}/_{d} = 0$) at around x/d = 3.5, while this can not be detected within the FOV of the experimental case. For the experimental case, the difference between the velocity along the top secondary flow inlet ($^{r}/_{d} = 0.6$) and the along the bottom secondary flow inlet ($^{r}/_{d} = 0.6$) is very small near the actuator exit, to about x/d = 0.75, but becomes larger, reaching a maximum value of

approximately 3 %, further away from the exit, indicating that the flow field is reasonably symmetric. After reaching the fully developed state, the percentage difference for the dimensionless axial velocities along the axis between the experimental and the numerical cases is about 10 %. The dimensionless axial velocities after reaching the fully developed value for both the numerical and the experimental cases along the secondary flow inlet are almost zero, which shows a good agreement between the two methods. It is important to note that flow pattern for the numerical and the experimental cases at this dimensionless time shows a good agreement with each other. The resulting dimensionless axial velocities for the secondary flow inlet after reaching the developed state falls within an approximate uncertainty limit of 20 %, which is beyond the acceptable limit of 10 %, as explained in Appendix D.

For t/T = 0.8, the velocity profiles of the numerical case in Figure 5.16 agree with the velocity profiles of the experimental case in Figure 5.15. Within the captured FOV the axial velocities for the experimental case do not reach a fully developed state. For the numerical case, the axial flow becomes fully developed at around x/d = 4. For the numerical case, the axial velocity along the centre of the secondary flow inlet ($^{r}/_{d} = 0.6$) becomes equal to the axial velocity along the axis ($^{r}/_{d} = 0$) at approximately x/d = 4.5, while this does not happen within the FOV for the experimental case. For the experimental case, the difference between the velocity along the top ($^{r}/_{d} = 0.6$) and the bottom ($^{r}/_{d} = -0.6$) secondary inlets is very small near the jet exit, till about x/d = 0.5, but becomes larger, reaching a maximum value of approximately 12 %, further away from the exit, indicating that the flow field is not symmetric. The percentage difference between the axial velocities along the axis for the experimental and the numerical cases is about 19 %. This

can be justified as the flow for the experimental case has not yet reached a fully developed value within the captured FOV. Also, the percentage difference between the axial velocity along the centre of the secondary flow inlet for the numerical case and the axial velocity along the centre of the averaged secondary flow inlet ($\frac{(r/d=0.6)+(r/d=-0.6)}{2}$) is approximately 7 %. The resulting dimensionless axial velocities, after reaching the developed state, fall within the acceptable uncertainty limit, 10 %, as described in Appendix D.

Overall, the majority of the numerical and the experimental cases have similar axial velocity patterns at each of the specified dimensionless times. The flow field for the experimental cases becomes fully developed at a shorter x/d distance compared to the numerical cases. This can be caused by the intense mixing, which was mentioned earlier in Section 5.2.2 and tends to eliminate the velocity differences within the mean flow. The greater the mixing, the faster the mean flow differences are eliminated causing a fully developed state to occur sooner. Thus, the flow field of the numerical cases is dominated by the vortex that is located at a larger distance downstream in the flow field than the ones formed in the experiment. Also, most of the numerical cases contain two vortices inside the shroud, but the experimental cases contain only one vortex. On the other hand, the vortex ring observed in the experiment dies out earlier than the ones observed in the numerical method. For the numerical cases, the axial velocities along the center of the secondary flow inlet, after reaching the fully developed value, seem to match with the axial velocities along the axis, but this does not apply for the experimental cases within the captured FOV's.

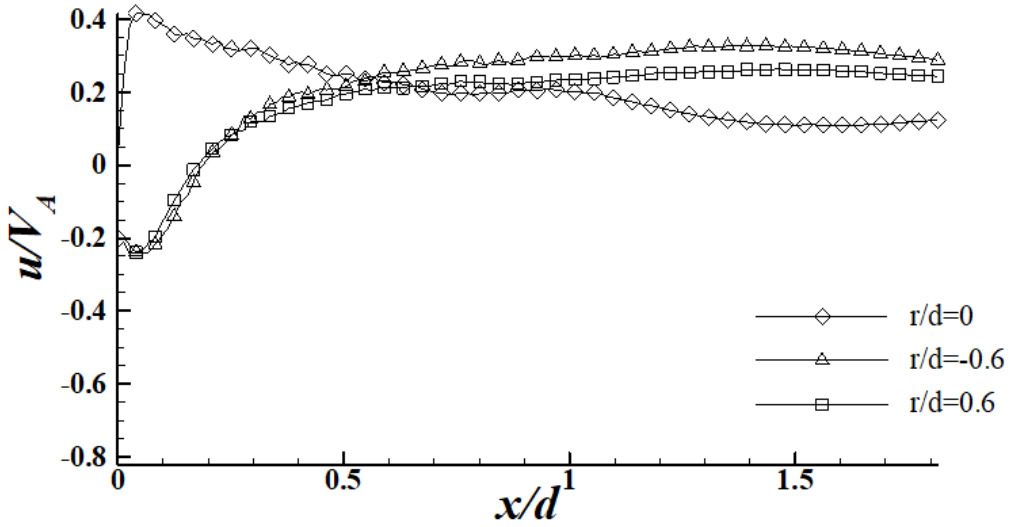

Figure 5.11 The Variation of the Experimental Dimensionless Axial Velocity along the Flow Field Downstream at Three Locations at t/T = 0.2

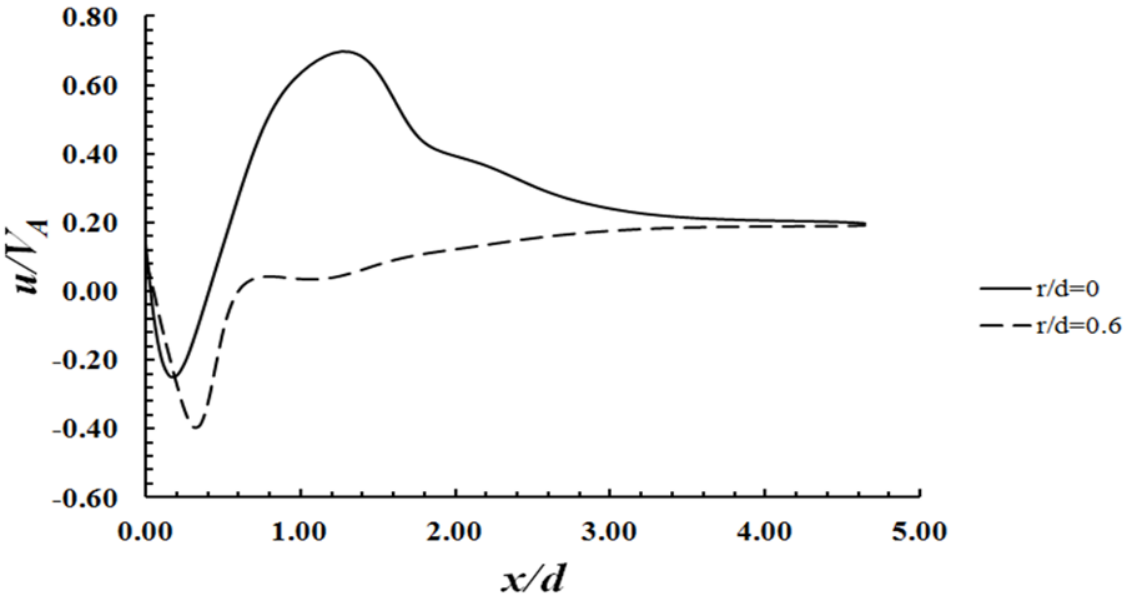

Figure 5.12 The Variation of the CFD Numerical Dimensionless Axial Velocity along the Flow Field Downstream at Three Locations at t/T = 0.2

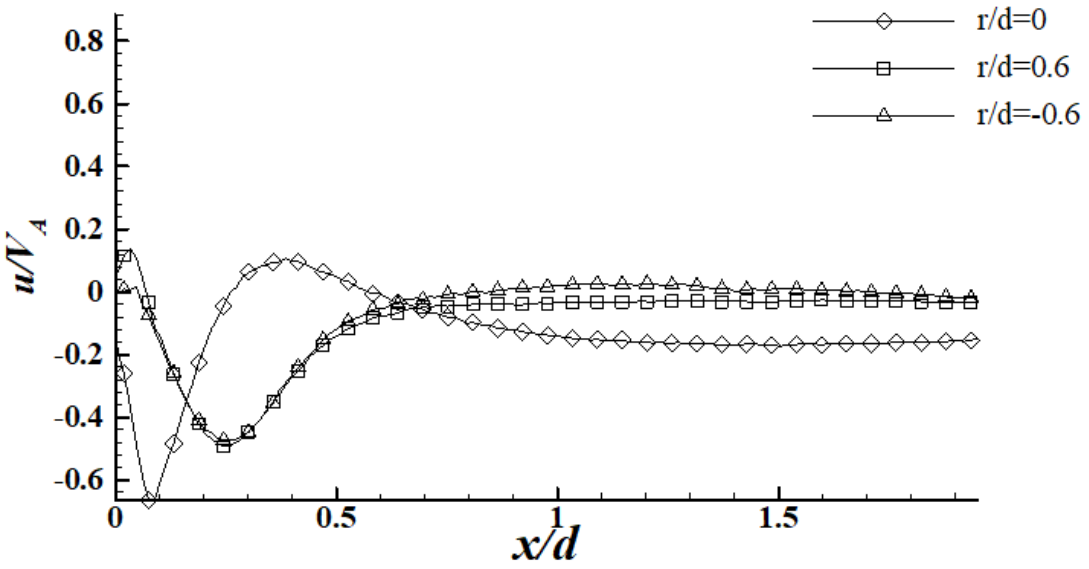

Figure 5.13 The Variation of the Experimental Dimensionless Axial Velocity along the Flow Field Downstream at Three Locations at t/T = 0.5

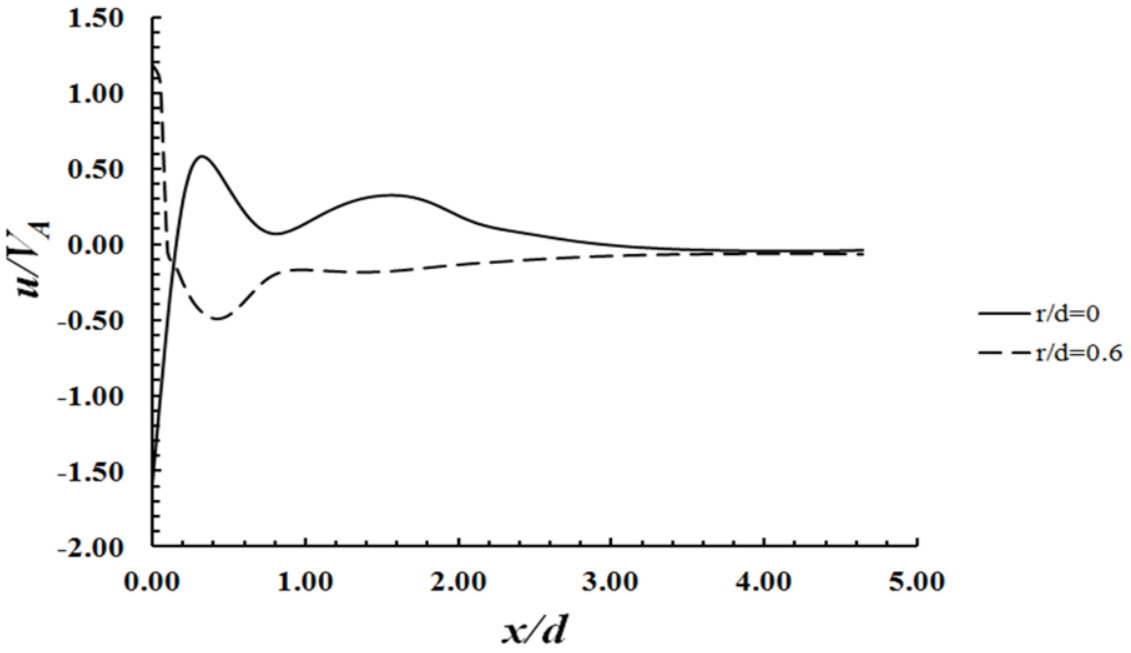

Figure 5.14 The Variation of the CFD Numerical Dimensionless Axial Velocity along the Flow Field Downstream at Three Locations at t/T = 0.5

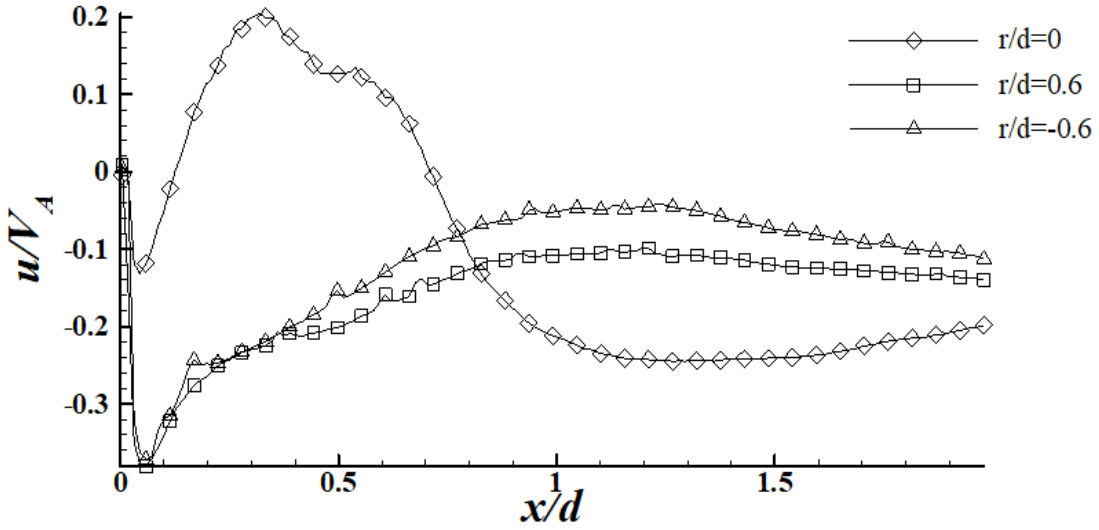

Figure 5.15 The Variation of the Experimental Dimensionless Axial Velocity along the Flow Field Downstream at Three Locations at t/T = 0.8

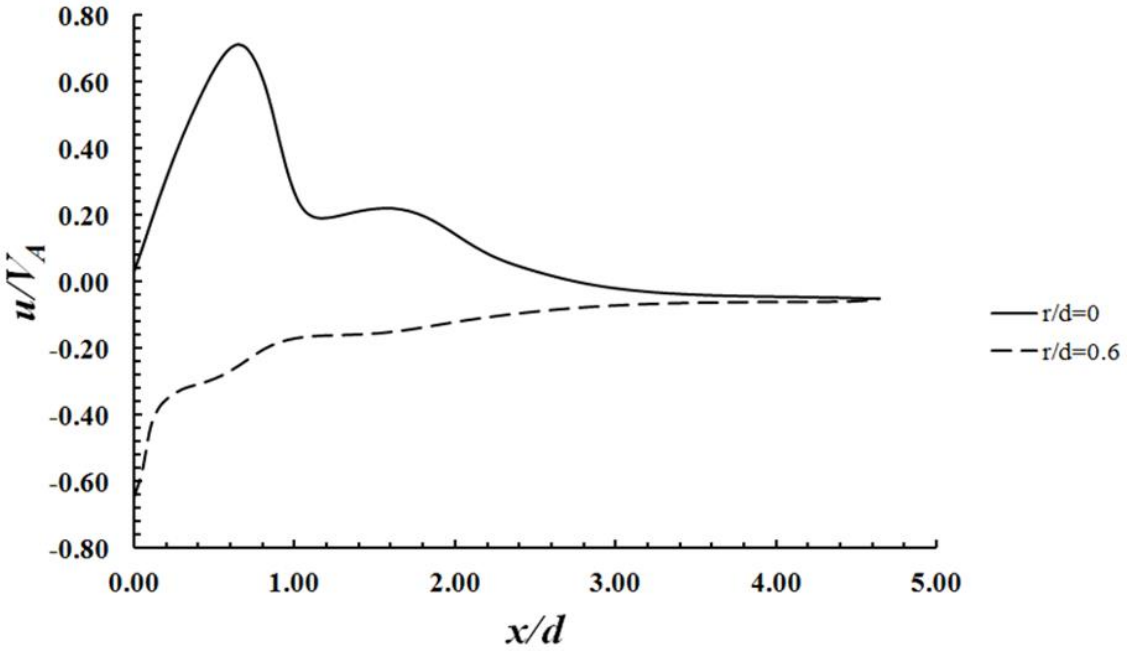

Figure 5.16 The Variation of the CFD Numerical Dimensionless Axial Velocity along the Flow Field Downstream at Three Locations at t/T = 0.8

5.2.4 Radial Variation of Axial Velocity across the Shroud's Diameter

Figures 5.17, 5.18 and 5.19 present the radial variation of axial velocity at x/d = 1.75 for the experimental and the improved CFD numerical method at t/T = 0.2, t/T = 0.5 and t/T = 0.8, respectively. The uncertainty for the experimental results is presented in Appendix D. Since the axisymmetric model is used for the numerical method the velocity profiles are perfectly symmetrical across the shroud diameter. However, for the experimental results, this has not been achieved. Also, for all the experimental cases, the left portion of the FOV, which extends from r/d = -0.69 to r/d = 0, is always greater than the right portion from r/d = 0 to r/d = 0.69. The percentage difference between the axial velocity peaks of each half of the flow field at t/T = 0.2, t/T = 0.5 and t/T = 0.8 are 5.5 %, 5.5 % and 5 %, respectively. The percentage difference in this section is defined as $(\frac{u1-u2}{V_A}) \times 100\%$. At t/T = 0.2, 0.5 and 0.8, the resulting dimensionless axial velocities fall within an uncertainty limit of 30 %, which is beyond the acceptable limit of 10 % as described in Appendix D. For the experimental cases, during the ejection phase (t/T = 0.8 to 0.2), the velocity along the secondary flow inlets ($^{r}/_{d} = 0.6 \,\&\, -0.61$) is higher than the velocity along the centerline ($^{r}/_{d} = 0.6$) and vice versa during the suction phase (t/T = 0.3 to 0.7). On the other hand, the numerical cases show the complete opposite velocity profiles.

Certain aspects of the experimental arrangement can contribute to the observed asymmetric velocity profiles. The gap between the shroud inner wall and the actuator's outer wall was found to have a 0.8 mm misalignment. Also, a non-flat surface of the piston can cause a variation in the radial flows in the azimuthal direction. Furthermore, this can be due to the misalignment of the laser illumination not being along the diametral plane.

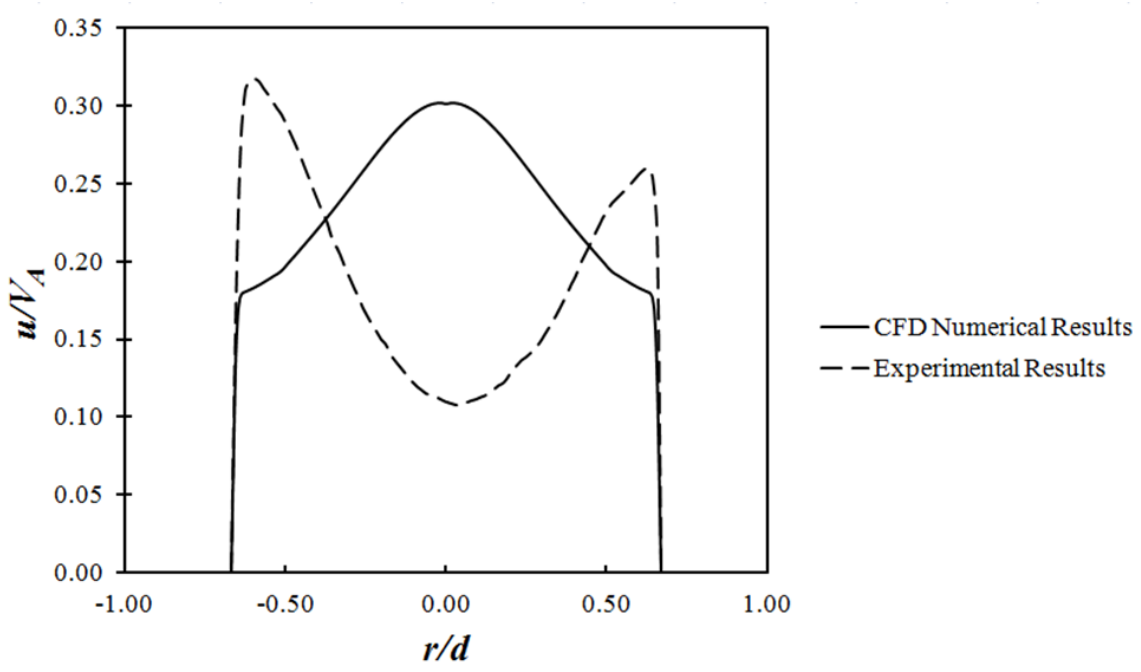

Figure 5.17 Velocity Profile across the Shroud's Diameter at x/d = 1.75 for the Experiment and the Numerical Simulation at t/T = 0.2

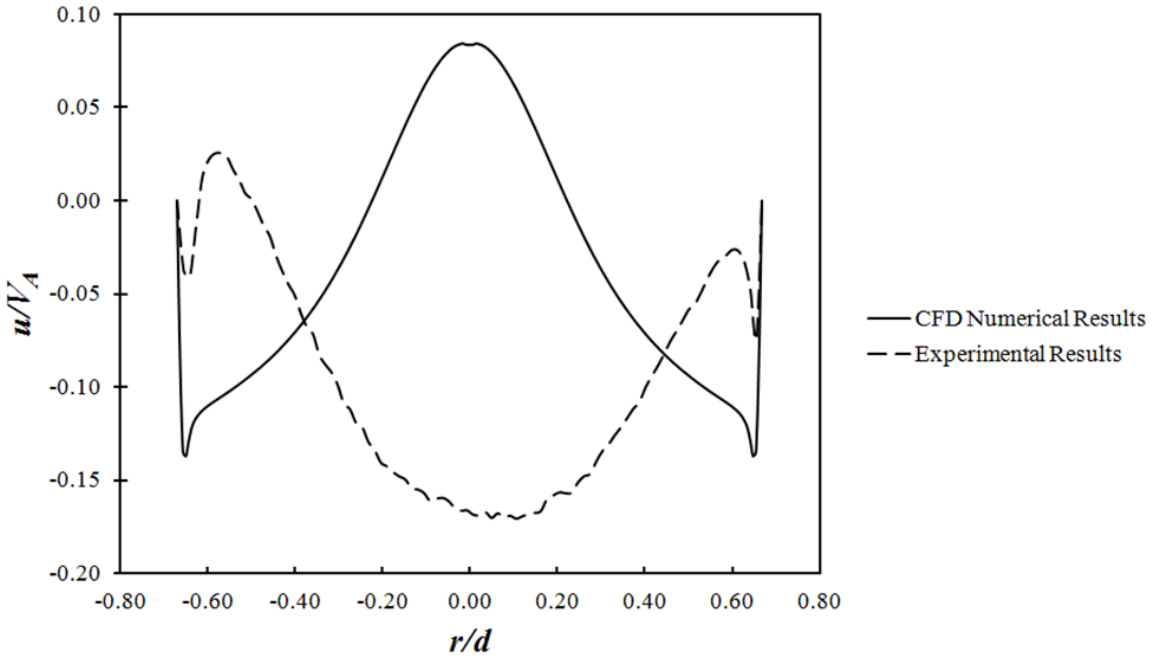

Figure 5.18 Velocity Profile across the Shroud's Diameter at x/d = 1.75 for the Experiment and the Numerical Simulation at t/T = 0.5

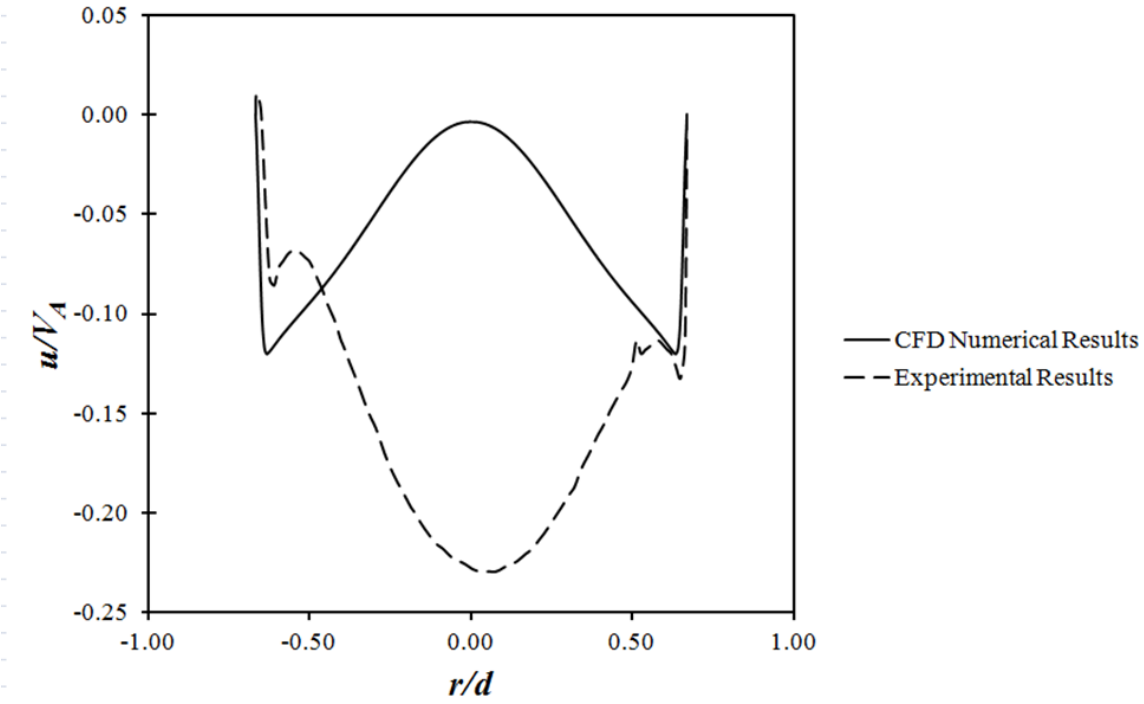

Figure 5.19 Velocity Profile across the Shroud's Diameter at x/d = 1.75 for the Experiment and the Numerical Simulation at t/T = 0.8

5.2.5 Axial Velocity Variation over Cycle at Certain Points of Interest in the Flow Field

Each of Figures 5.20, 5.21, 5.22 and 5.23 presents the axial velocity results over one cycle, at one of the four points selected for analysis, previously shown in Figure 4.7. Both the experimental method and the improved CFD numerical simulation results are included. Two points are located at an axial distance of one diameter away from the actuator's outlet: one along the axis and the other one in the middle of the gap between the shroud and the actuator's wall. Due to asymmetry, in the case of the experiment, the average of the two values for the points in the middle of the secondary flow inlets is used. The other two points are located at the same location as the first two points, but they are located one and a half diameters away from the actuator's outlet. As observed in Section

5.2.3, the experimental results become fully developed in a shorter downstream distance than the improved CFD numerical results. A comparison between the results at the points of interest with the results at the points reaching the fully developed state is of interest. The percentage difference in this section is measured based on the difference between the two dimensionless axial velocities multiplied by100, $(\frac{u1-u2}{V_A}) \times 100$.

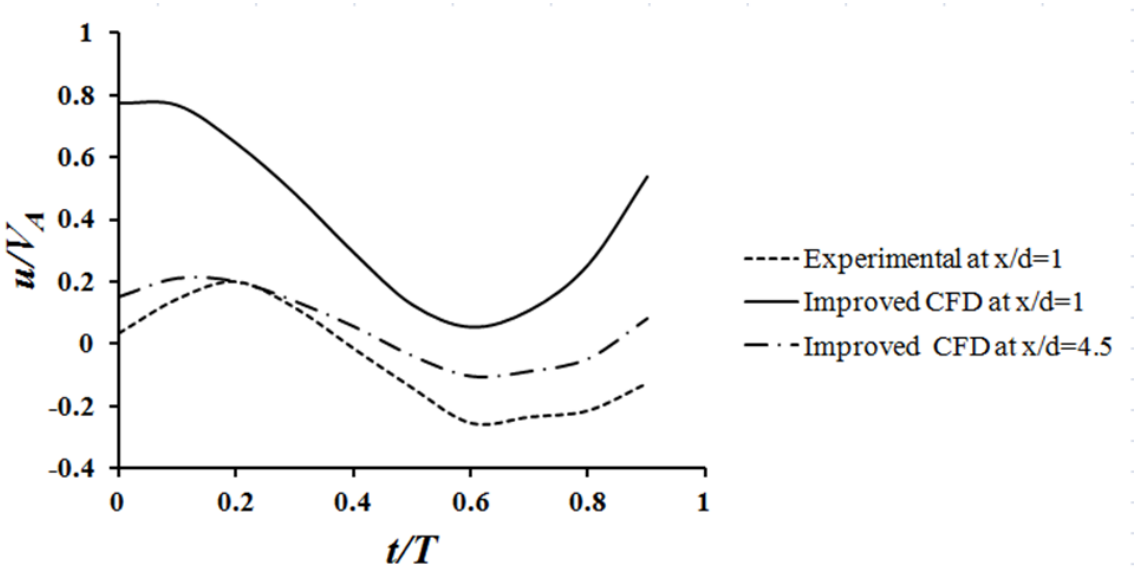

Figure 5.20 A Dimensionless Axial Velocity Comparison of the Experimental Method and the Improved CFD Numerical Model along the Axis at x/d = 1

Figures 5.20 and 5.21 show the comparison within a cycle along the axis, or the centerline of the flow field. The improved CFD model results and the experimental results have the same trend. However, the maximum percentage difference between the improved numerical model and the experimental results at x/d = 1 equals approximately 80 %, and the maximum percentage difference between them at x/d = 1.5 equals about 40 %. As mentioned in Section 5.2.3, the fully developed state for the improved numerical model at all the dimensionless times is achieved at about x/d = 4.5, while at x/d = 1.5, the fully

developed state for the experimental results is achieved. Comparing the fully developed states for the experimental results, at x/d = 1.5, and the fully developed results for the improved numerical model, at x/d = 4.5, the maximum percentage difference between the two models is approximately 16 %.

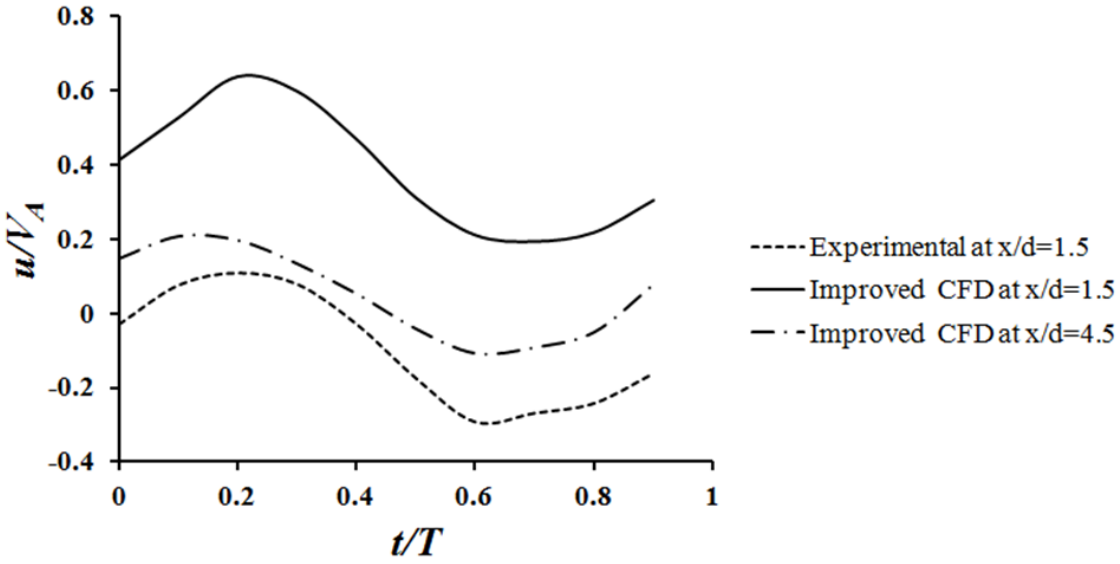

Figure 5.21 A Dimensionless Axial Velocity Comparison of the Experimental Method and the Improved CFD Numerical Model along the Axis at x/d = 1.5

Similarly, Figures 5.22 and 5.23 show the comparison within a cycle along the middle of the secondary flow inlet of the flow field. The improved CFD model results and the experimental results show the same trend. However, the maximum percentage difference between the improved numerical model and the experimental results at x/d = 1 equal approximately 20 %, and the maximum percentage difference between them at x/d = 1.5 equals about 18 %. As mentioned in Section 5.2.3, the fully developed state for the improved numerical model at all the dimensionless times is achieved at about x/d = 4.5, while at x/d = 1.5, the fully developed state for the experimental results is achieved.

Comparing the fully developed states for the experimental results, at x/d = 1.5, and the fully developed results for the improved numerical model, at x/d = 4.5, the maximum percentage difference between the two models is approximately 10 %.

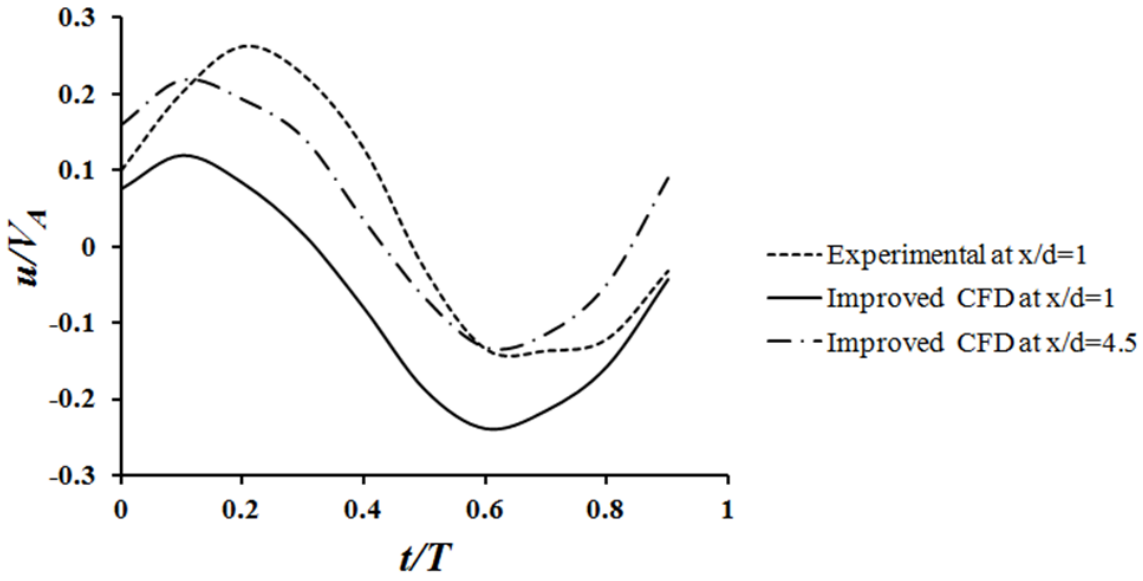

Figure 5.22 A Dimensionless Axial Velocity Comparison of the Experimental Method and the Improved CFD Numerical Model along the Centre of the Secondary Flow Inlet at x/d = 1

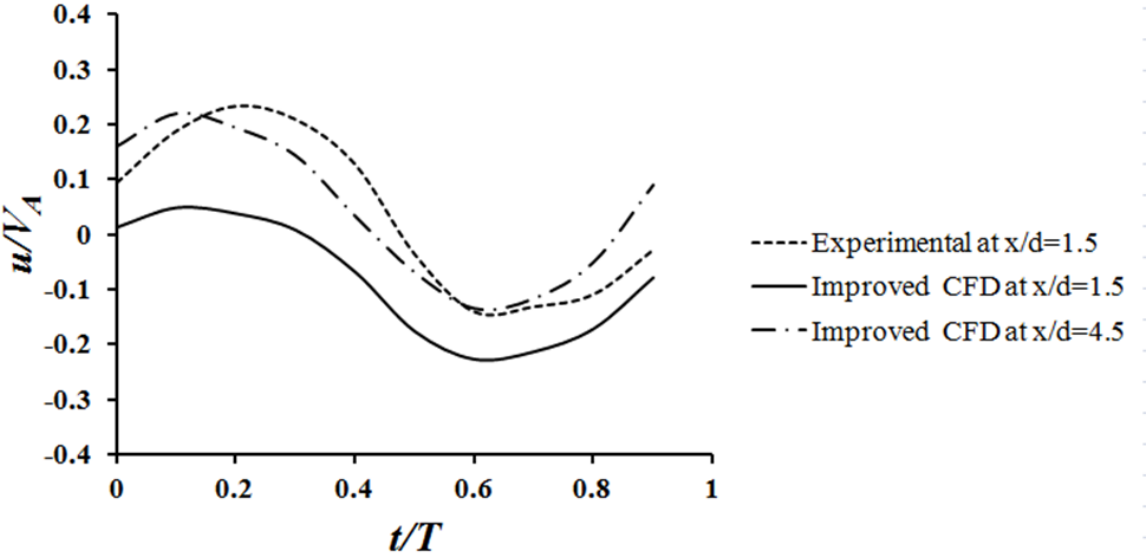

Figure 5.23 A Dimensionless Axial Velocity Comparison of the Experimental Method and the Improved CFD Numerical Model along the Centre of the Secondary Flow Inlet at x/d = 1.5

Generally, the figures show similar trends between the experimental and the improved CFD numerical results along the centerline and along the middle of the secondary flow inlet, but the magnitudes vary significantly at the specified points. The results obtained from the improved CFD numerical model at the fully developed state agrees better with the experimental results compared with the ones obtained before reaching the fully developed state. This is due to the intense mixing that was evidenced by the cycle-to-cycle variations as explained in Section 5.2.2 and 5.2.3

Chapter 6

CONCLUSIONS & RECOMMENDATIONS

6.1 Conclusions

Recall that the objectives of this thesis are to conduct both PIV experiments and an improved numerical model and to compare them. Also, an evaluation of the accuracy of a previous 2-D SJE simplified model [20] is conducted. The conclusions of this work are grouped into two sections as indicated below.

6.1.1 Evaluation of the Simplified Numerical Model

- The assumptions regarding the actuator outlet velocity profile and the secondary flow inlet pressure made in the simplified numerical model are shown to be inaccurate.
- The simplified numerical model is found to over-predict the variation of phase-averaged volume flow rate throughout the cycle and the cycle averaged value.
- The complexity of the flow field observed in the SJE requires a careful consideration of the model selection.

6.1.2 Comparison of Improved Numerical Model with Experiments

- The improved numerical model gives a reasonably accurate prediction of the variation of phase-averaged volume flow rate throughout the cycle and the cycle averaged values.
- Numerical and phase-averaged experimental flow field patterns show some similarities however, certain details are quite different.

- The experiments exhibited extremely large cycle-to-cycle variations which is an indication of intense fluid mixing. It is speculated that these variations are due to turbulence and the observed transient large-scale structure motion.
- The experimental axial velocity profiles across the shroud diameter are asymmetrical and completely different in trend to the numerical results at most time phase positions during the cycle.
- Consideration of phase-averaged axial velocity profiles in the longitudinal direction indicates that the flow in the experimental case develops within a shorter downstream distance than predicted by the numerical method. It is speculated that the early development is due to the intense mixing that is present in the shroud.

6.2 Recommendations

The following recommendations for future work are made to improve the understanding of the complex flow field of the SJE,

- Perform a new optimization study of synthetic jet ejector's performance using the improved numerical model.
- Develop a 3-D CFD numerical model in order to determine the effect of the imposed symmetry condition on the flow field.
- Use an unsteady turbulence model that has the capabilities of resolving the wide range of scale structures associated with the mixing, such as Large Eddy Simulation (LES).
- Repeat the experiment with a time-resolved PIV in order to eliminate the uncertainties resulting from the phase-averaging method.

- Eliminate the misalignment in the gap between the actuator and the shroud and repeat the experiment.
- Extend the field-of-view of the experiment to approximately x/d = 3 in order to capture the fully developed state for all the dimensionless times within the cycle.

Appendix A

CAD DRAWINGS

The CAD parts drawings are presented in Figures A.1 to A.14 inclusive. The units of the dimensions are specified within the "Sequence ID" Label at the bottom right of each of the drawings.

A.1 Tank CAD Drawings

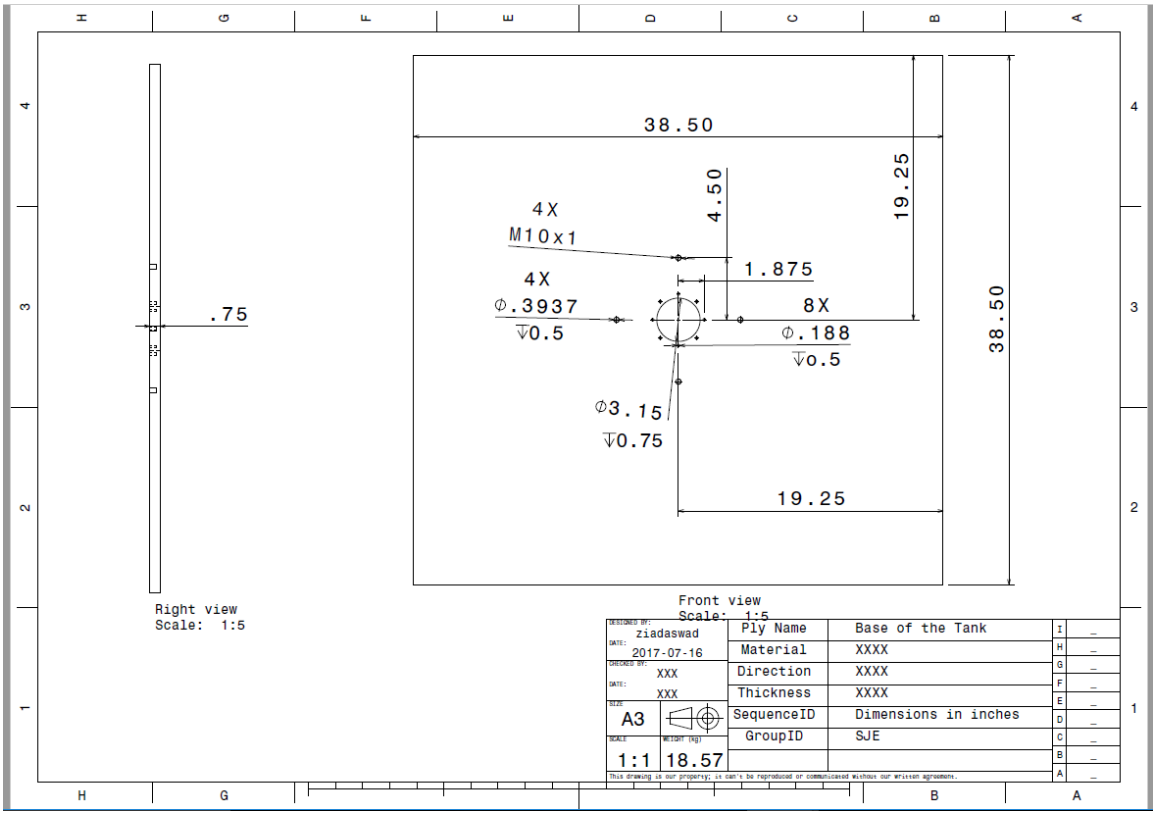

Figure A.1 Base of the Tank CAD Drawing

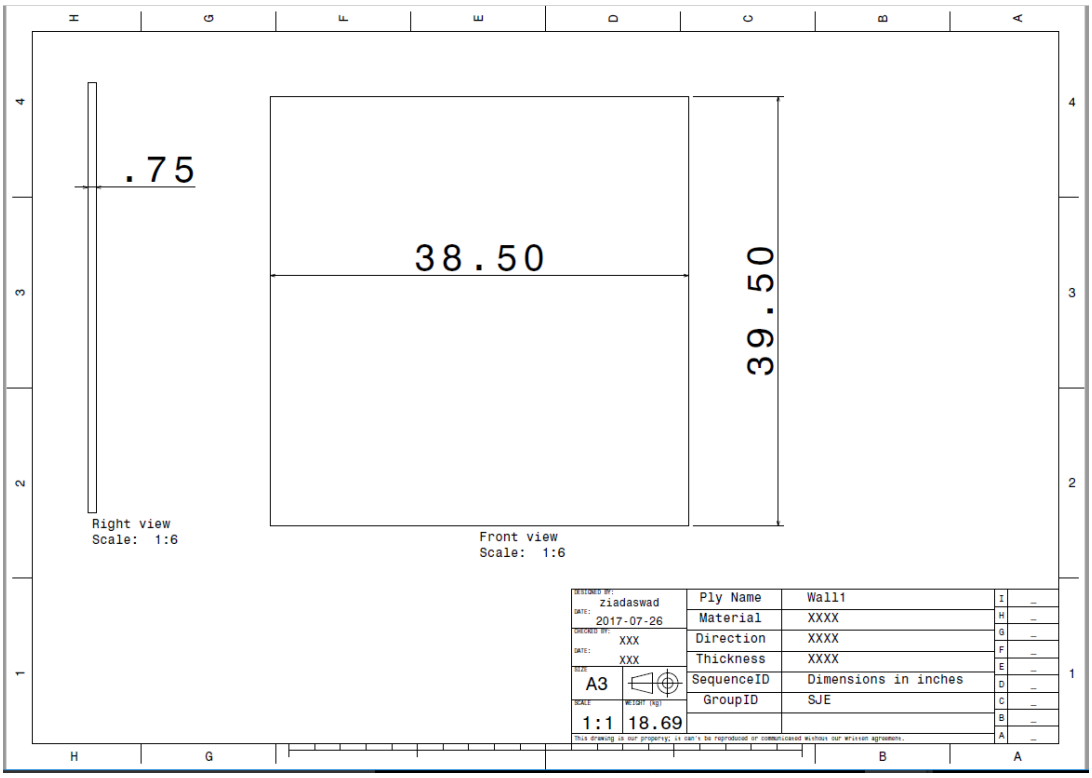

Figure A.2 The Smaller Side Walls CAD Drawing

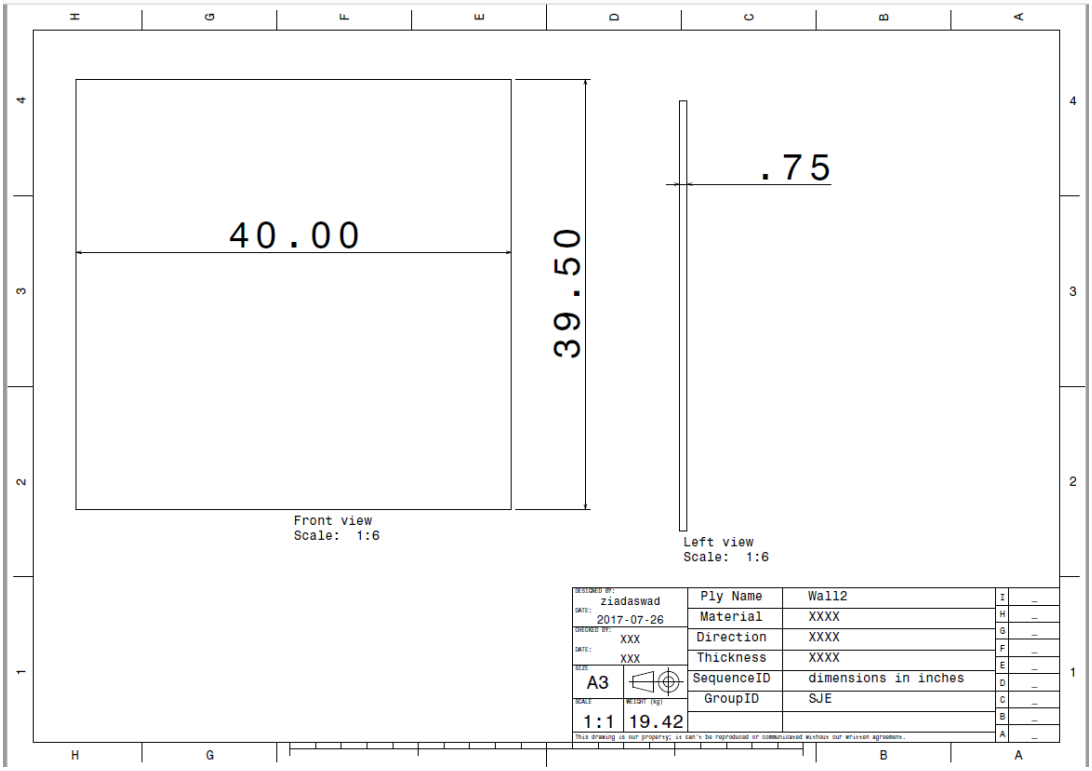

Figure A.3 The Larger Side Walls CAD Drawing

A.2 SJE CAD Drawings

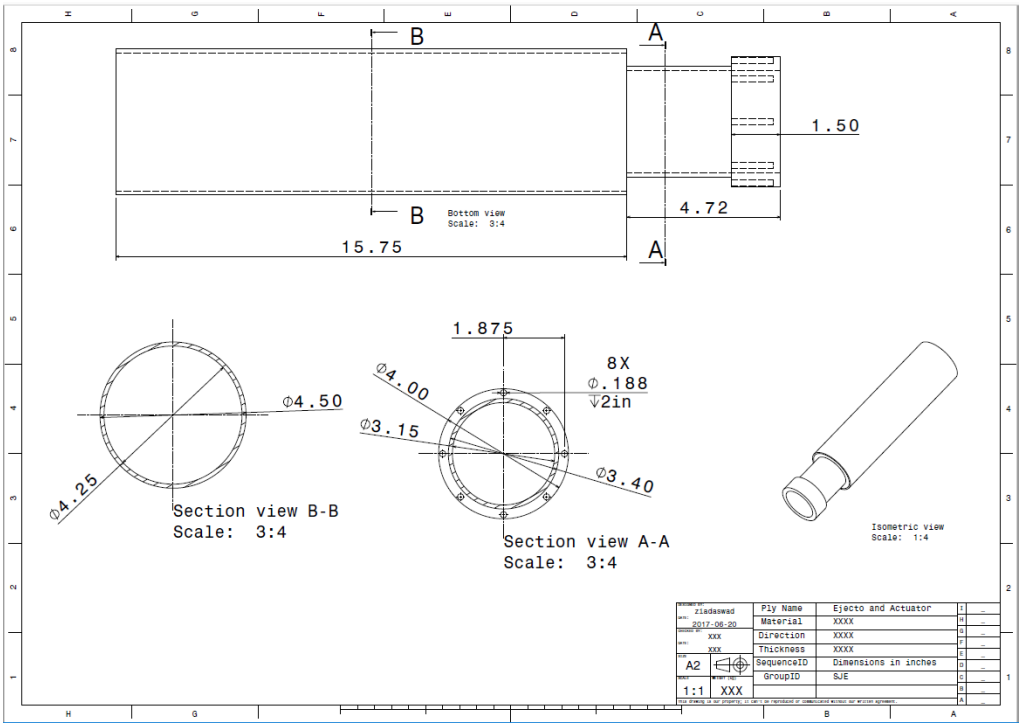

Figure A.4 The Shroud, the Actuator and the Flange Integrated CAD Drawing

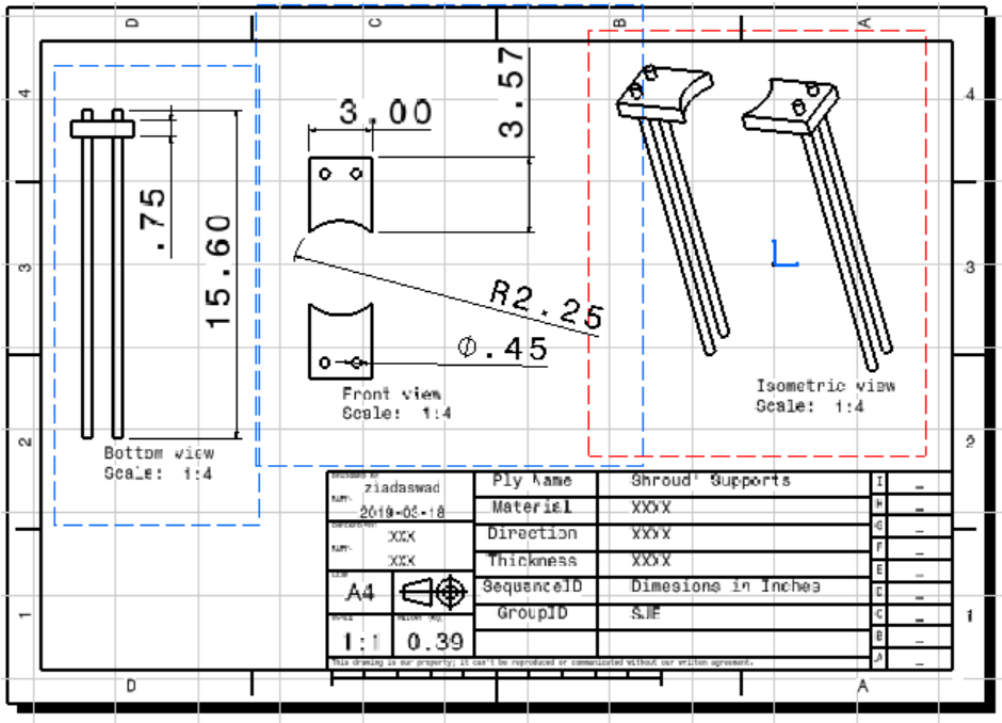

Figure A.5 The Shroud Supports CAD Drawing (Acrylic Pieces and Threaded Rod)

A.3 Bench CAD Drawing

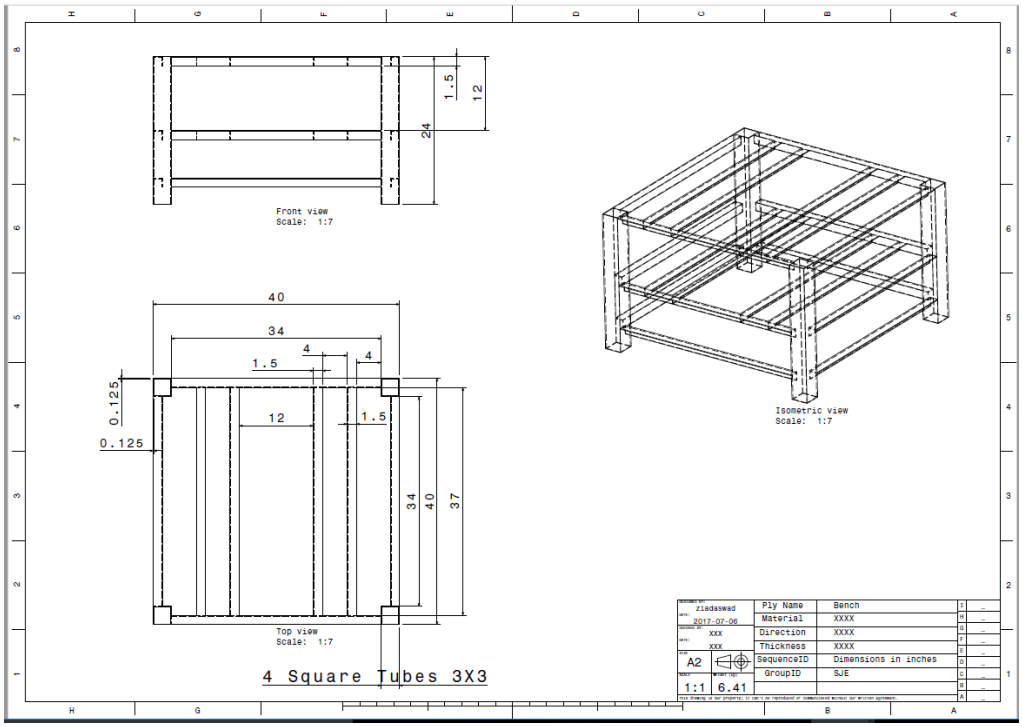

Figure A.6 Bench CAD Drawing

A.4 Scotch Yoke Mechanism CAD Drawings

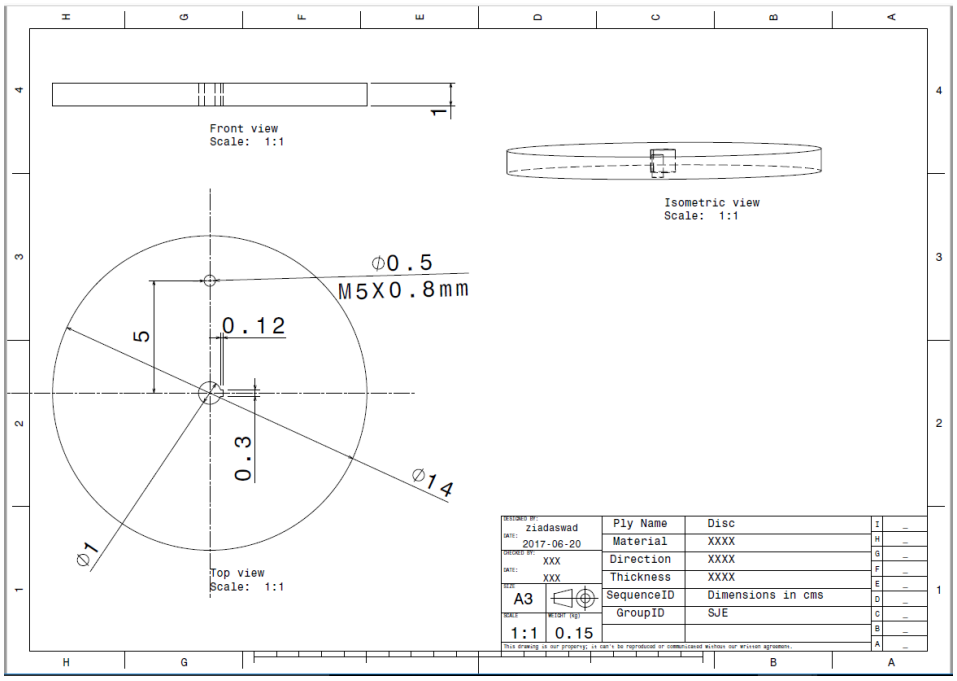

Figure A.7 Disc CAD Drawing

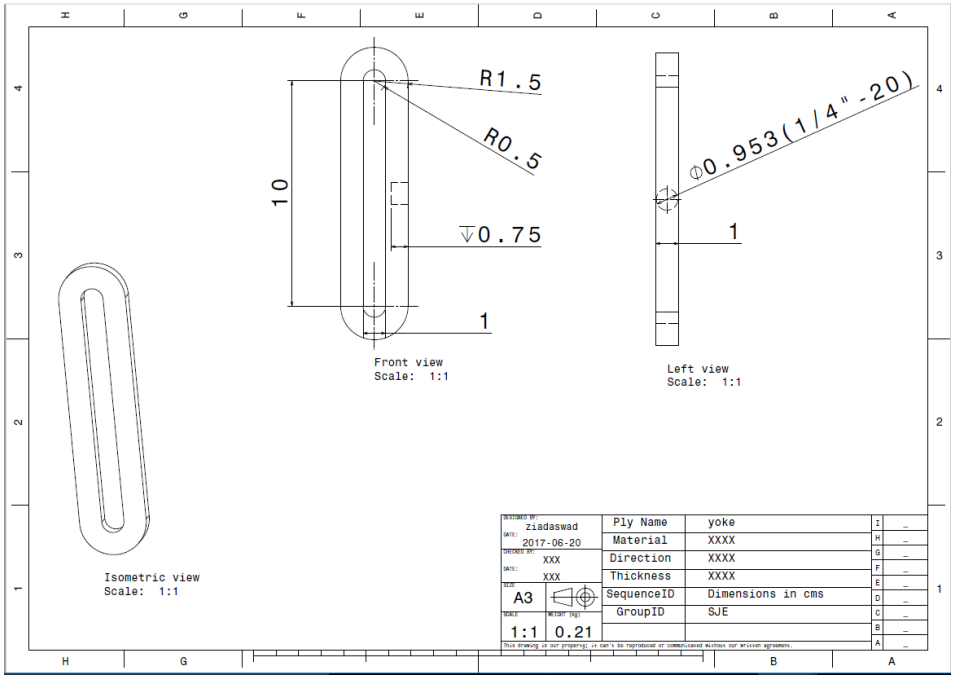

Figure A.8 Yoke CAD Drawing

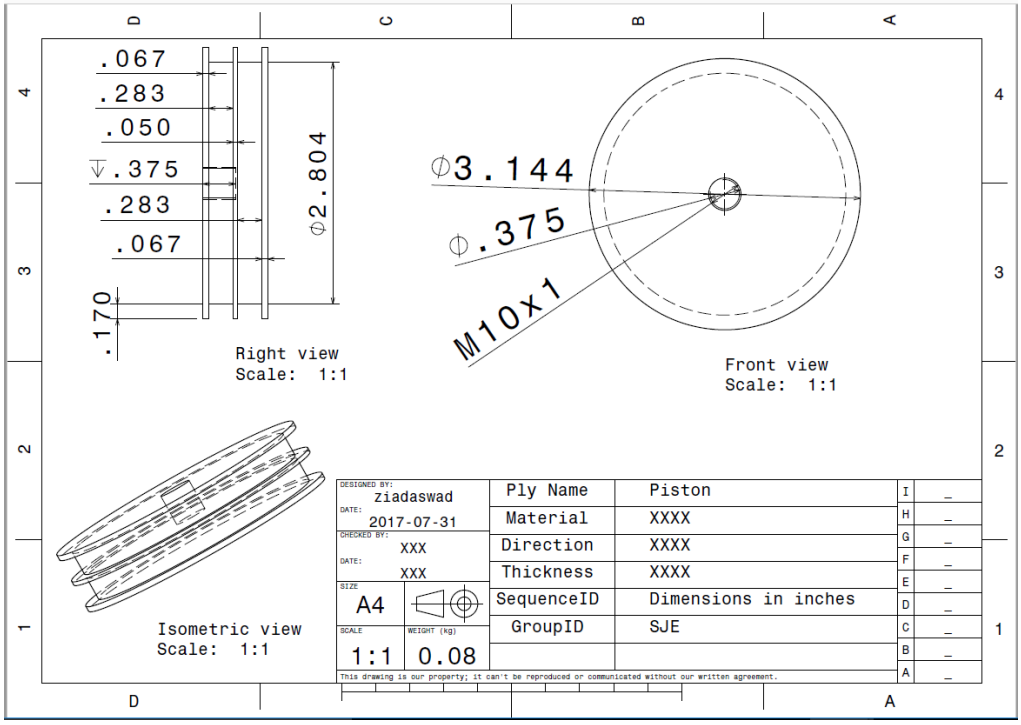

Figure A.9 Piston with Two O-rings CAD Drawings

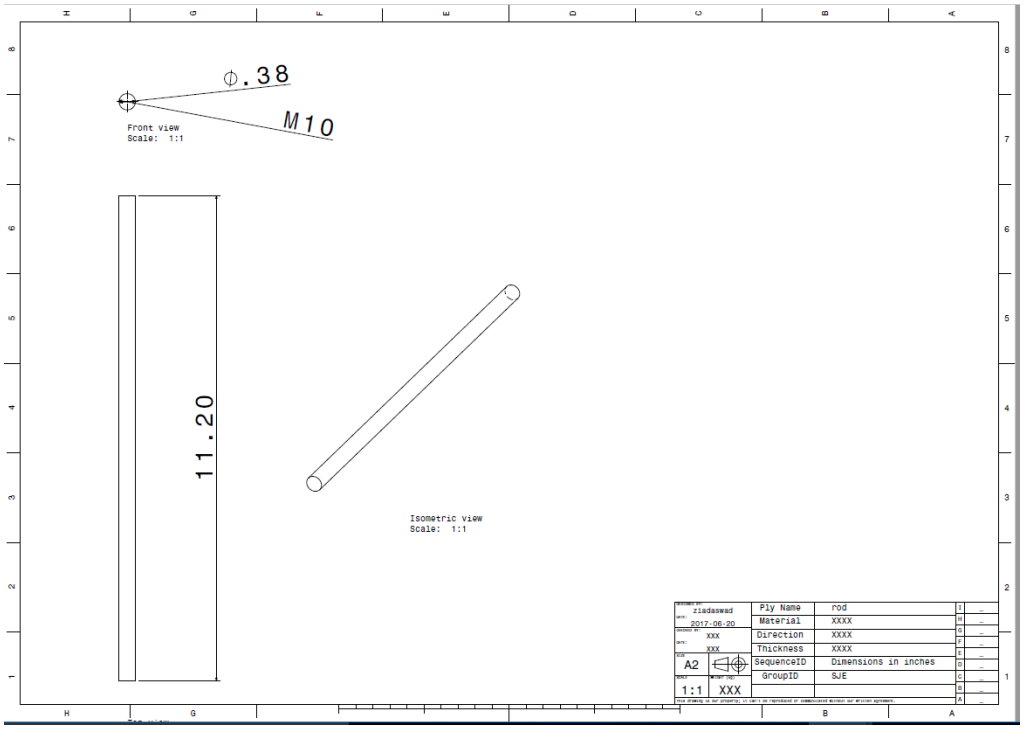

Figure A.10 Rod (Connects between the Yoke and the Piston) CAD Drawing

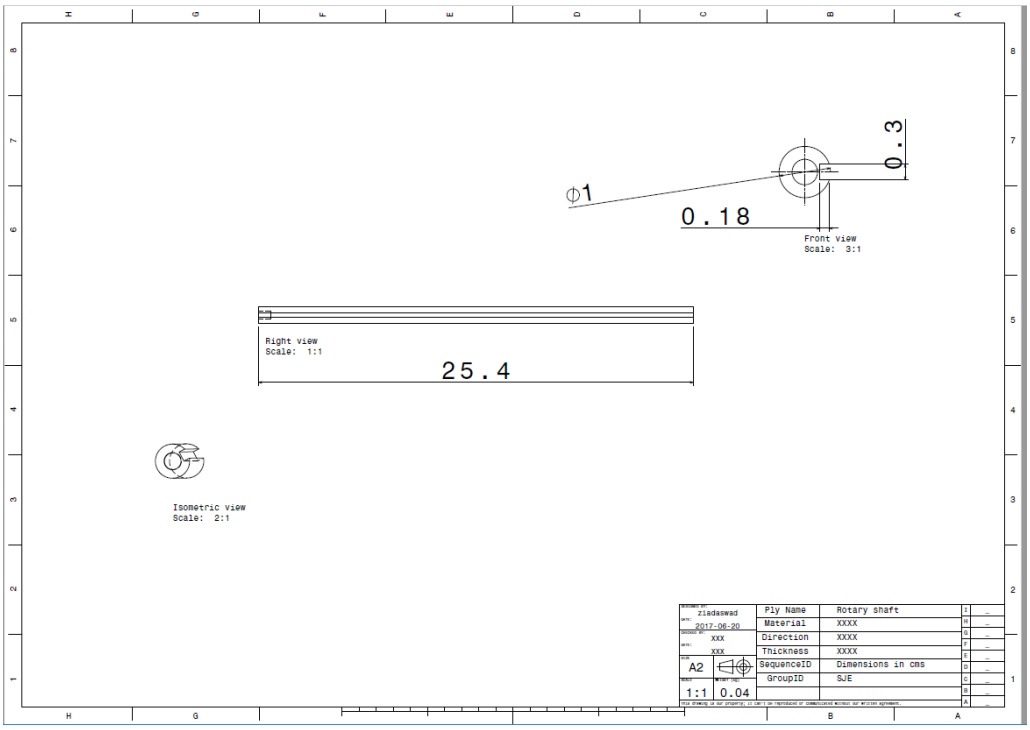

Figure A.11 Keyed Rotary Shaft CAD Drawing

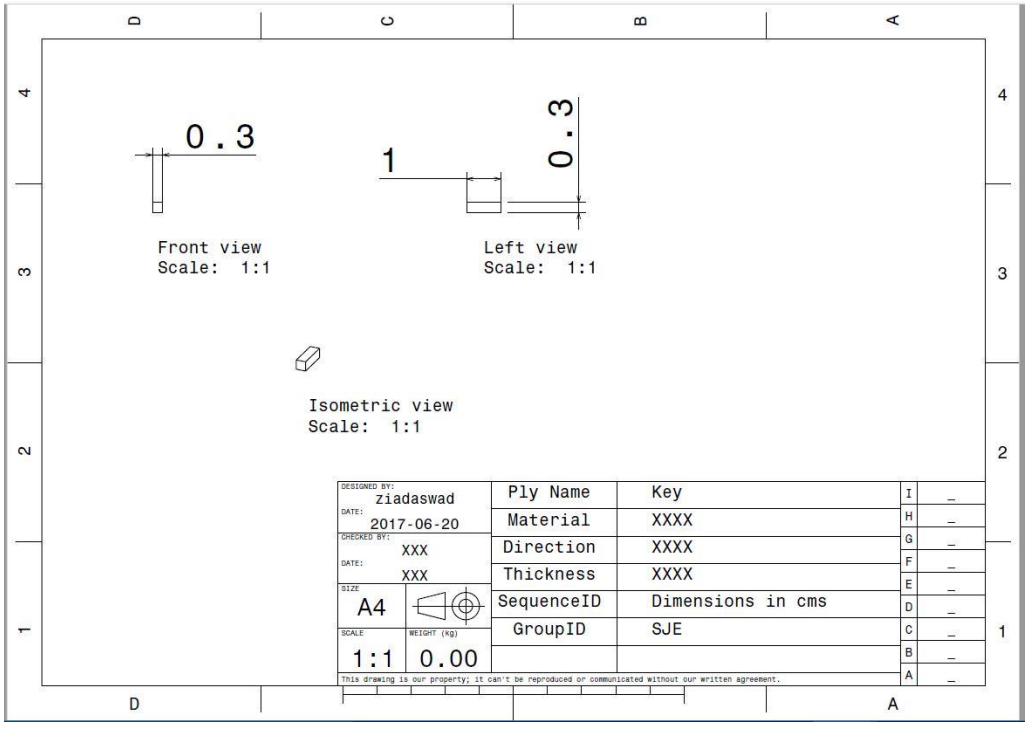

Figure A.12 Square Key CAD Drawing

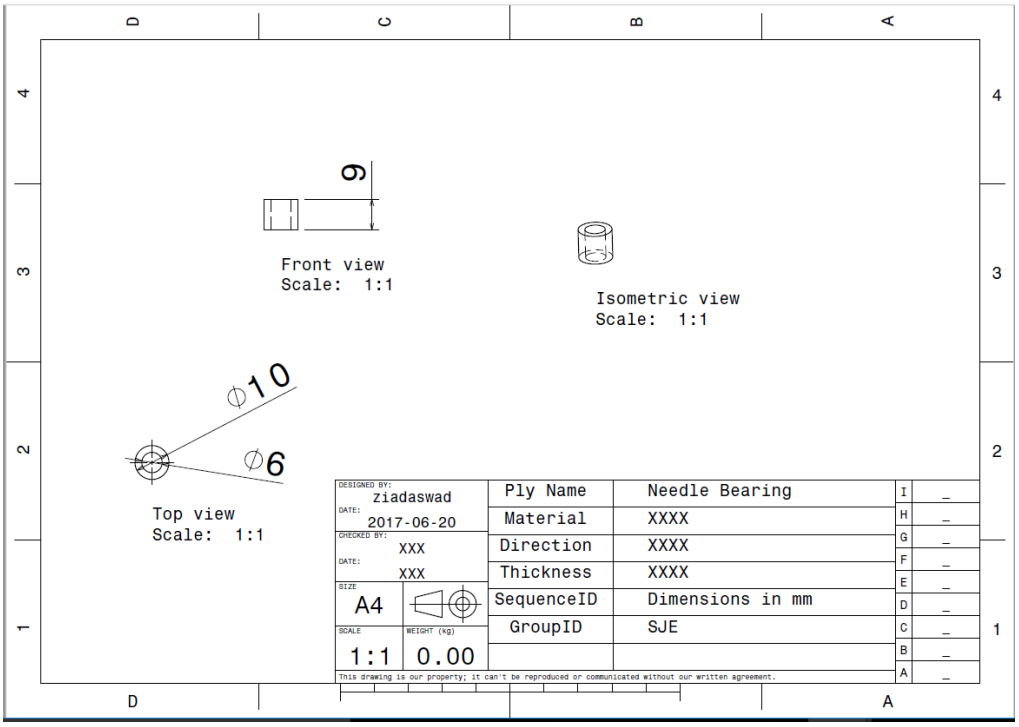

Figure A.13 Needle Bearing for the Yoke CAD Drawing

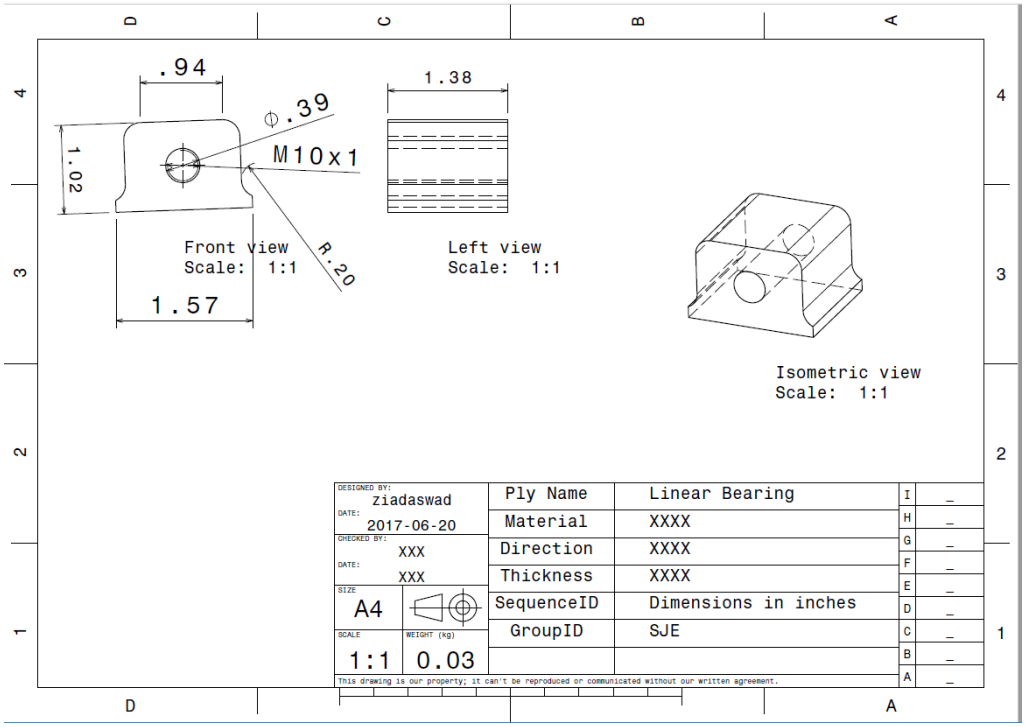

Figure A.14 Linear Bearing Drawing

Appendix B

VERIFICATION OF SEEDING PARTICLE SIZE

In Chapter 3, it is stated that the seeding particles used for the current experiment are silvered hollow glass spheres of mean diameter 17 μm with a density of 1.6 g/cc and manufactured by Potters Industries. This section includes an estimate of the particles ability to accurately follow the flow.

The external forces acting on the moving seeding particles in the water flow must overcome the inertial force due to the mass of the particles (m_p) and the added mass (m_a) that is related to accelerating the surrounding fluid. This added mass can be taken as is ½ the volume of the sphere times the fluid density [79]. The force equation is shown in Equations B.1, where a_y is the acceleration of the particles in the flow. The external forces include the weight and drag forces. In this case, the weight is small compared to drag and is neglected. Using the drag force formula for sphere, $F_D = 6\pi\mu V_r$, where V_r is the relative velocity and equals $V_f - V_p$, where V_f is the velocity of water and V_p is the seeding particle velocity. This formula when substituted into Equation B.1 gives Equation B.2, where μ is the kinematic viscosity of water, ρ_p is the density of the seeding particles, ρ is the density of water and r is the radius of the particle. After simplification, the ordinary differential equation given in Equation B.3, results which can be solved using Laplace transforms. Since V_f is a cosine wave with an amplitude V_A, its Laplace transform is $V_A/(s^2 + w^2)$. Applying the Laplace transform to the entire equation gives Equation B.4. Rearrangement gives Equation B.5.

$$\sum F_y = (m_p + m_a)a_y \tag{B.1}$$

$$6\pi\mu r(V_f - V_p) = \frac{4\pi r^3}{3}(\rho_p + {}^{\rho}/_{2})\frac{dV_p}{dt} \tag{B.2}$$

$$9\mu V_f = 2r^2\left(\rho_p + {}^{\rho}/_{2}\right)\frac{dV_p}{dt} + 9\mu V_p \tag{B.3}$$

$$9\mu\frac{V_A\, s}{s^2 + w^2} = 2r^2\left(\rho_p + {}^{\rho}/_{2}\right) s\, V_p(s) + 9\mu V_p(s) \tag{B.4}$$

$$V_p(s) = \frac{C1\, V_A s}{(s^2 + w^2)(s + C1)} \tag{B.5}$$

$$\text{where, } \mathrm{C1} = \frac{9\mu}{2r^2(\rho_p + {}^{\rho}/_{2})} \tag{B.6}$$

The variation of the velocity of the particle with time is found by taking the Laplace inverse of $V_p(s)$, as shown in Equation B. 7,

$$V_p(t) = \boldsymbol{V_A \cos(wt) * C1^2 + {}^{V_A * w * \sin(wt) * C1}/_{(C1^2 + w^2)}} \tag{B.7}$$

Figure B.1 shows the dimensionless time versus the calculated particle velocity. It was found that $V_p = V_A = 0.187$, where V_A is the piston velocity amplitude that is obtained from the optimum conditions. Thus, it is concluded that the particles from Potters Industries [61] are following the flow very accurately, so the selection of these particles is a good choice for the current experiment.

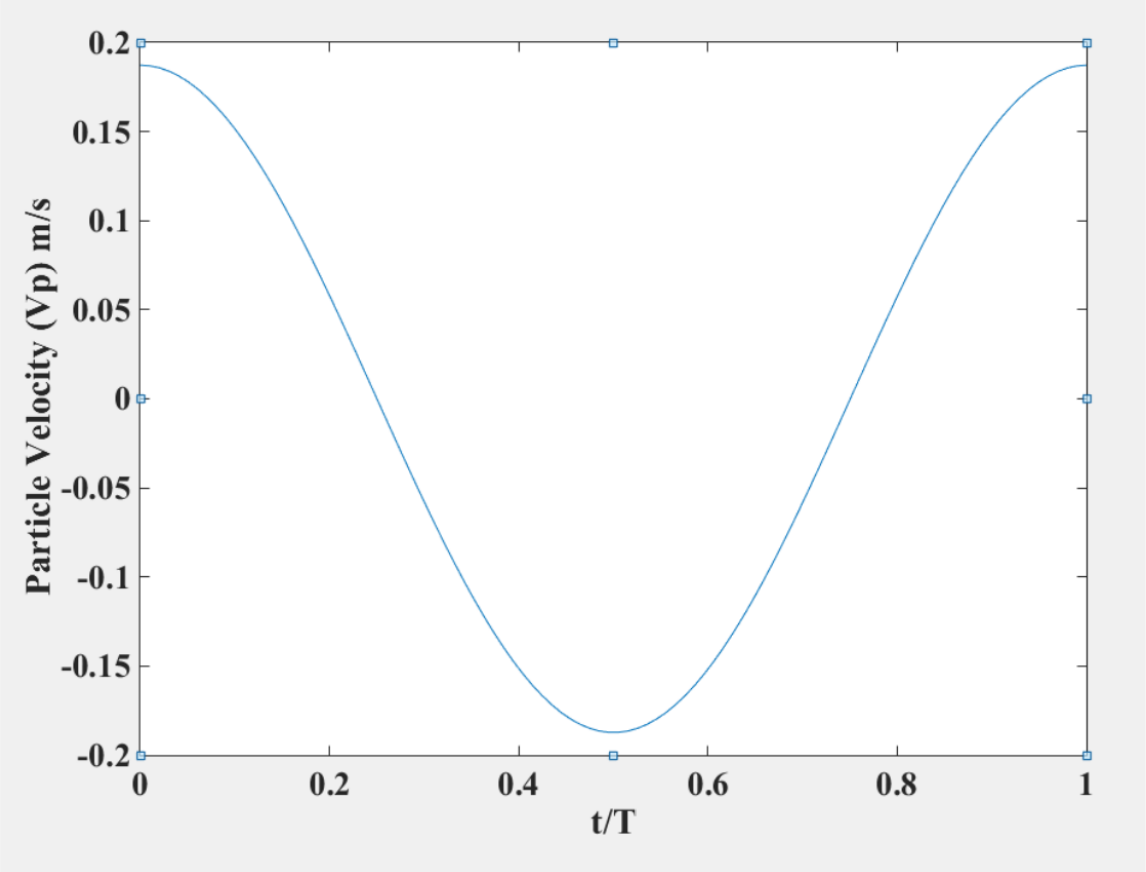

Figure B.1 Dimensionless Time Versus Particle Velocity Results

Appendix C

PIV SOFTWARE SET-UP

TSI Insight 4G v10.1 software [80] is used to control the PIV measurement process. In this section, a brief explanation of the steps involved in capturing images is presented. Initially, a directory in which to save the frames must be created by selecting the Exp Tree on the control panel. By selecting the Capture tab on the control panel, the application for which the image is being captured is selected to be PIV. By selecting the Tools | Component Setup, the hardware component parameters, the synchronizer, laser and camera, can be set-up as shown in Figure C.1.

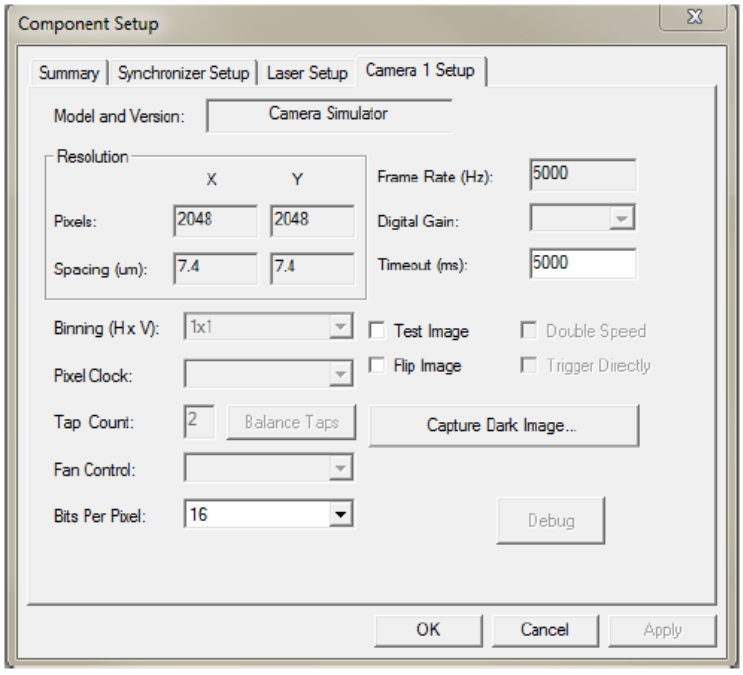

Figure C.1 Component Setup Window from Insight 4G Software by TSI

Also, under the Capture tab, the exposure mode is selected to be Synchronized in order to have the synchronizer trigger to control the camera shutter and the laser pulsing according to the values set in the Timing Setup dialog box. Also, from the Capture tab, the Capture selection mode is chosen to be Sequence. Under the Sequence Setup dialog box, the number of captures is set to be 1500, and the starting file number is selected for each experiment. The Start Number increments automatically based on the last saved file number. Also, under the Sequence Setup dialog box, the Image Save Mode is selected to determine how the files should be saved. The frames are saved to the folder that was initially created in the directory, and the Display While Capturing option is selected to display the images while capturing them. Before starting the experiment, the laser power level is selected from the Laser Energy Setup box under the Capture tab on the control panel. The Laser Energy Setup box opens with the Q-Switch Delay/Pulse Energy default values for High, Medium and Low laser power settings for the two (A and B) lasers. In this section, only the Capture Timing Setup values selected are explained in detail.

Within the Capture Timing Setup window, the straddle PIV frame mode, which enables the camera to acquire two consecutive single-exposure images, is selected, and the PIV exposure time (time that the PIV camera is open) set to be 350 μs. The external triggering option is enabled, and the trigger delay selected based on the desired measuring point within the cycle. The trigger timeout, which is the maximum time that the synchronizer must wait to receive an external trigger input; if no external trigger input is received in the specified time duration, a timeout message appears, is set to 10,000 ms for all the measurements. The laser pulses/trigger, which specifies the number of laser pulses per external trigger, set to be 1 for all the measurements. The Δt parameter, which is the

time interval between the two captured frames, is selected using the process of trial and error, based on the percentage of the good velocity vectors and the mean particle displacement obtained. It is found that a Δt value of 4300 μs resulted in the highest mean particle displacement that results in the highest percentage of acceptable velocity vectors for all the measurements. The highest mean particle displacement was detected to be approximately 4 pixels. The pulse repetition rate and the laser pulse delay settings did not affect the experiments due to the external triggering option being enabled. Figure C.2 shows one example of an Insight 4G capture timing setup window.

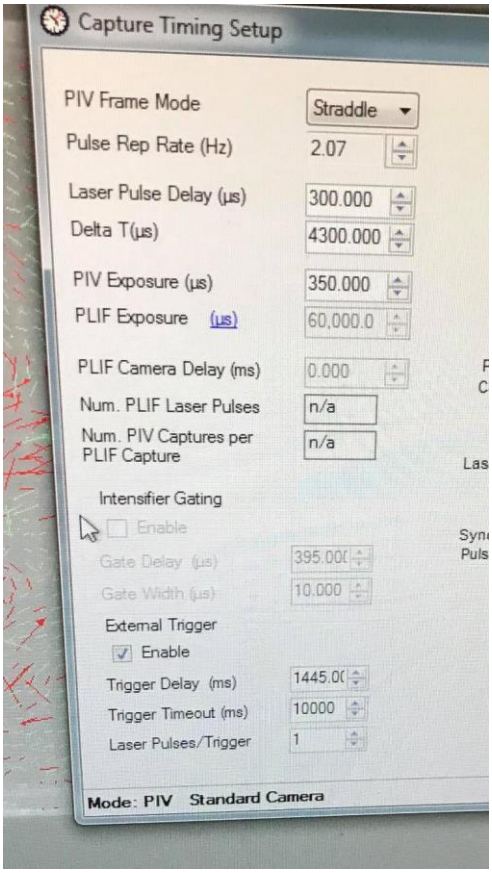

Figure C.2 Capture Timing Setup Window from Insight 4G Software by TSI

Appendix D

PIV UNCERTAINTY MEASUREMENTS

In Section 3.5, it is mentioned that the method used to estimate uncertainties was that proposed by the Visualization Society of Japan (VSJ) [71] as a result of an organized project on PIV standardization (PIV-STD) [72]. A guideline of the estimation of the uncertainty of the PIV dataset was based on this procedure and put forward by the International Towing Tank Conference (ITTC) in 2008 [73]. For this procedure, the FOV at a dimensionless time of 0.2 is arbitrarily selected and the other FOVs are expected to be the same order of magnitude. The PIV measurement of velocity is based on Equation D.1 as given below,

$$u = \alpha\left(\frac{\Delta x}{\Delta t}\right) + \delta u \qquad \textbf{(D.1)}$$

where u is the velocity magnitude, Δx, Δt, and α are the displacement of the particle on the camera image, the time interval between successive images and the magnification factor relating the actual particle displacement to that on the camera image, respectively. The magnification factor is determined based on the calibration procedure performed before the velocity measurements are taken. Since the PIV data analysis process depends on the visualization of the flow field by tracer particles, a lag between the response of the tracer particles and the flow will always exist, and the resulted uncertainties are represented by the parameter, δu.

The sources of uncertainty in each of these four parameters are determined individually and the propagation of the total uncertainty calculated. The symbols $u(x_i), c_i$

and u_c correspond to the typical unit uncertainty of the variable, x_i, the sensitivity coefficient of the uncertainty of that variable and the cumulative uncertainty as a result of the sources, respectively. The sensitivity coefficient c_i for all the error sources is taken directly from the guideline [73]. The sources for each parameter are considered separately below and the uncertainty results obtained from this method are summarized in Table D.1. The sources of the error in the calibrations are as follows:

D.1 Error in Calibration, α

D.1.1 Image Length of the Calibration Target (Ruler)

The length of the calibration target, which is the aluminum ruler glued to a nylon block, is measured on the image plane. If the position of the calibration target is detected from a single point, the typical uncertainty band will be 0.7 pixels. The sensitivity of the uncertainty is given to be 3.84×10^{-4} mm/pixel^2 from the guideline.

D.1.2 Physical Length of the Calibration Target (Ruler)

The uncertainty of the physical length of the calibration target also affects the accuracy of the magnification factor. As mentioned previously, an aluminum ruler glued to a nylon block was used as the calibration target for the current experiment. The maximum uncertainty can be estimated to be approximately 1.5 mm. The sensitivity coefficient is 1.22×10^{-3} /pixel from the guideline.

D.1.3 Image Distortion

The image could be affected by the aberration of the lens and the associated uncertainty. The distortion of the image could be less than 0.5 % of the total image length,

which is $(0.005) \times (2496) \approx 12$ pixels. The sensitivity coefficient can be estimated to be 1.41×10^{-4} mm/pixel^2 from the guideline.

D.1.4 Distortion in the CCD Device

It was assumed that there was no distortion in the CCD device and as a result, it did not contribute towards any uncertainty.

D.1.5 Ruler Position

The position of the light sheet and the calibration ruler can be different. Thus, the maximum uncertainty can be estimated to be 0.5 mm. The sensitivity coefficient is estimated to be 2.87×10^{-4} /pixel from the guideline.

D.1.6 Ruler Parallelism

Ideally, the ruler is perpendicular to the camera axis, however, it is extremely difficult to achieve. The maximum misalignment is assumed to be 5°, and the sensitivity coefficient is estimated to be 0.011 mm/pixel from the guideline.

D.2 Error in Displacement of the Particle Image, Δx

D.2.1 Laser Power Fluctuations

The spatial and temporal fluctuations of the laser sheet affect the detection and computation of the correlation peak in the PIV recordings. Assuming that the experiment is well-controlled, the uncertainty due to this may be 1/10 of the particle diameter which is 0.0017 mm. The sensitivity coefficient is estimated to be about 13.06 pixels/mm.

D.2.2 Optical Distortion by CCD

It is assumed that there is no optical distortion in the CCD device.

D.2.3 Normal Viewing Angle

If the illumination plane is not perpendicular to the camera axis, this could affect the velocity measurement. The angle is estimated to be maximum 5° off the normal and the sensitivity coefficient is 0.011 pixels/mm from the guideline.

D.2.4 Mismatching Error

In the pixel unit analysis, mismatching of the paired particle can take place. The typical uncertainty due to this error can be estimated to be about 0.2 pixels as stated by Okamoto et al [81].

D.2.5 Sub-Pixel Analysis

The uncertainty of the sub-pixel analysis depends on the number of factors, such as the size of the tracer particles, the noise level of the image and the particle concentration. In a conservative way, the maximum uncertainty of this for all the experiments is estimated to be 0.03 pixels as stated by Okamoto et al [81].

D.3 Error in the Time Interval, Δt

D.3.1 Delay Generator

The delay generator controls the pulse timing, and the uncertainty of that is 5×10^{-4} seconds, as found from the manual.

D.3.2 Pulse Timing Accuracy

The laser pulse has some uncertainty associated with it. The typical uncertainty band, as found from the manual is 5×10^{-9} seconds.

D.4 Error in δu

D.4.1 Particle Trajectory

The particle trajectory depends on the local velocity gradient and the acceleration of the flow. When the tracer particles are assumed to follow the flow faithfully, the error due to the particle trajectory is 0.01 % of the total velocity. Assuming the maximum velocity is about 0.88 m/s, the uncertainty is $0.88 \times 1000 \times 0.0001 = 0.088$ mm/s.

D.4.2 Three-Dimensional Effect

The out-of-plane velocity vectors also contributes towards the total uncertainty. When the out-of-plane velocity is assumed to be 1 % of the total flow velocity, the uncertainty can be estimated to be 0.73 mm/s.

Table D.1 summarizes the calculated error sources from the VSJ method. The cumulative uncertainty is found to be about 0.00159 m/s. The values in the last column are calculated by taking the square root of the sum of the squares in each category, or parameter. Also, the cumulative uncertainty is found by plugging the final answer from each parameter into Equation D.1. This would give the absolute worst case where all uncertainties are at their maximum values at the same time.

Table D.1 Summary of the Velocity Uncertainty Estimates from Different Sources

Parameter	Category	Error Source	$u(x_i)$	C_i	Ci u(xi)	u_c
α (mm/Pixel)	Calibration	Reference Image	0.7 (pixel)	3.84×10^{-4} (mm/pixel^2)	2.68×10^{-4}	0.0021
		Physical Distance	1.5 (mm)	1.22×10^{-3} (1/pixel)	2.44×10^{-5}	
		Image Distortion by Lens	12 (pixel)	1.41×10^{-4}	1.69×10^{-3}	
		Image Distortion by CCD	0	0	0	
		Ruler Position	0.5(mm)	2.87×10^{-4} (1/pixel)	1.435×10^{-4}	
		Parallelism	0.087 (rad)	0.011 (mm/pixel)	9.57×10^{-4}	
Δx (pixel)	Acquisition	Laser Power Fluctuation	0.0017 (mm)	13.06 (pixel/mm)	0.0222	0.2031
		Image Distortion by CCD	0	0	0	
		Normal View Angle	0.087 (rad)	0.011 (mm/pixel)	9.57×10^{-4}	
	Reduction	Mismatching Error	0.2 (pixel)	1	0.2	
		Sub-Pixel Analysis	0.03 (pixel)	1	0.03	
Δt (sec)	Acquisition	Delay Generator	5×10^{-4} (sec)	1	5×10^{-4}	0.0005
		Pulse Time	5×10^{-9} (sec)	1	5×10^{-9}	
δu (mm/s)	Experiment	Particle Trajectory	0.088 (mm/s)	1	0.088	0.7353
		Three-Dimensional Effect	0.73 (mm/s)	1	0.73	
		u= α(Δx/Δt)+δu		Cumulative Uncertainty (mm/s)		1.5883

D.5 Dimensionless Axial Velocity (U_u/V_A)

The dimensionless axial velocity, u/V_A, is used to present some of the measurements, where u is the axial velocity and V_A is the piston velocity amplitude. Because the velocity varies in a sinusoidal manner, the piston velocity amplitude is calculated as follows,

$$V = S_a\omega \qquad \textbf{(D.2)}$$

where S_a = 0.05 m and U_{S_a} = 0.0005 m, which is the uncertainty of the piston amplitude displacement. Since $\omega = \frac{2\pi}{T}$, $\frac{U_\omega}{\omega} = \frac{U_T}{T} = \frac{0.1\ s}{1.769\ s}$, where U_ω is the uncertainty of the angular velocity and U_T is the uncertainty of the period. Thus, $\frac{U_\omega}{\omega} \approx 0.05 \approx 5\ \%$. The

uncertainty for the velocity amplitude U_{V_A} depends on the amplitude displacement and the angular velocity. The value of $\frac{U_{V_A}}{V_A}$ is determined as follows,

$$\frac{U_{V_A}}{V_A} = \sqrt{(\frac{U_{S_a}}{S_a})^2 + (\frac{U_\omega}{\omega})^2} = \sqrt{(0.01)^2 + (0.05)^2} = 0.05 \approx 5\ \% \qquad \textbf{(D.3)}$$

In the previous section, the cumulative uncertainty U_u is calculated to be 0.00154 m/s. Thus, $\frac{U_u}{V_A}$ = 0.00824. The relative uncertainty in $\frac{U_u}{V_A}$ can be found as given in Equation D.4,

$$\frac{U_{\frac{u}{V_A}}}{\frac{u}{V_A}} = \sqrt{(\frac{U_u}{u})^2 + (-\frac{U_{V_A}}{V_A})^2} = \sqrt{(\frac{0.00154}{u})^2 + (0.05)^2} \qquad \textbf{(D.4)}$$

Rearranging Equation D.4,

$$\frac{U_u}{u} = \sqrt{(\frac{U_{\frac{u}{V_A}}}{\frac{u}{V_A}})^2 - (-\frac{U_{V_A}}{V_A})^2} \qquad \textbf{(D.5)}$$

Assuming that the acceptable uncertainty of the dimensionless axial velocity ($U_{\frac{u}{V_A}}$) is 10 % of the dimensionless axial velocity ($\frac{u}{V_A}$), u can be calculated as follows,

$$\frac{0.00154}{u} = \sqrt{(0.1)^2 - (0.05)^2} \qquad \textbf{(D.6)}$$

Thus, u is found to equal 0.018 m/s, and the dimensionless axial velocity ($\frac{u}{V_A}$) equals $0.018/0.187 \approx \pm \mathbf{0.1}$. ***If the magnitude of the dimensionless axial velocity ($\frac{u}{V_A}$) is greater than 0.1, the uncertainty is less than 10 % and is acceptable.***

Repeating the same procedure for 20 % uncertainty, the range of the dimensionless axial velocity ($\frac{u}{V_A}$) is found to be around $\pm\ \mathbf{0.043}$.

Repeating the same procedure for 30 % uncertainty, the range of the dimensionless axial velocity ($\frac{u}{V_A}$) is found to be around $\pm \mathbf{0.027}$.

Appendix E

NUMERICAL SOLUTION- FLUENT SET-UP

This appendix shows the configuration of Fluent for all the simulations performed in this study using the improved CFD model. It has been divided into steps, which are presented in the order in which Fluent is setup and run. The geometry and the mesh cases are read using the setup option using ANSYS Workbench 17. The following selections are then made:

1- Load the User Defined Function (UDF)

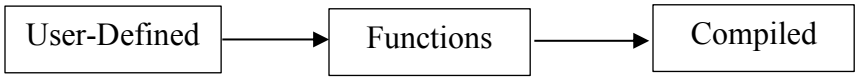

The source file containing the UDF shown in Figure E.1 is then read. The UDF code is written in C Language, and saved as a C Source file, using Microsoft Visual Studio Express 2012.

```
#include "udf.h"
#include "dynamesh_tools.h"
#include "math.h"

#define M_PI 3.14159265358979323846    /* Defining value of PI */

/*This UDF has to be compiled and placed in the folder trial_files\dp0\FFF-1\Fluent */
/* Start Workbench from the Command Prompt Window to successfully compile this UDF */

DEFINE_CG_MOTION(oscillate,dt,vel,omega,time,dtime)       /* DEFINE MACRO for moving the piston */
{
Thread *t;
face_t f; /* define the variables */
t = DT_THREAD(dt);
begin_f_loop(f,t) /* loop over each face in the zone to create an array of data */
{
real ampl,disp,omg;

/* reset velocities */
NV_S (vel, =, 0.0);
NV_S (omega, =, 0.0);

/* motion */
ampl = 0.05 ; /* amplitude of oscillation in m (L/2) */
omg = 2 * M_PI * (1/(0.001*1769)) ; /* 0.565259 Hz, 1.7691s, 1769 time steps */
disp = ampl * ( 1 + sin(omg * time) ); /* resultant displacement */

vel[0] = +1 * ampl * 2 * M_PI *(1/(0.001*1769)) * cos(2*M_PI*(1/(0.001*1769)) * time);
}
end_f_loop(f,t)
}
```

Figure E.1 UDF Used to Move the Dynamic Mesh Periodically

2- Select Solver

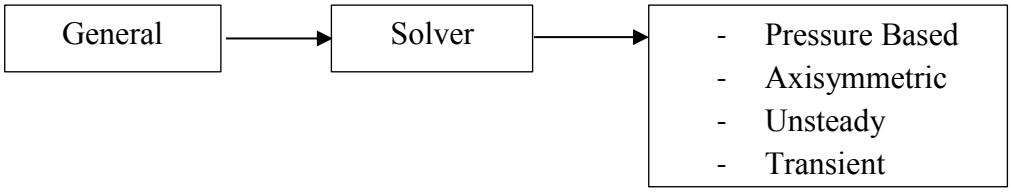

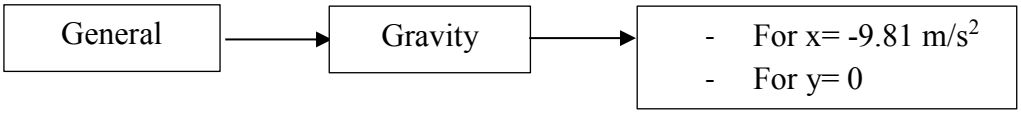

3- Select Models

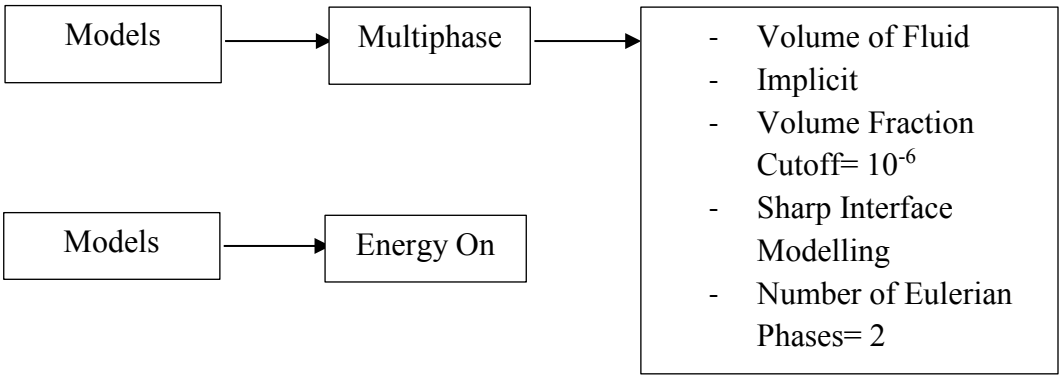

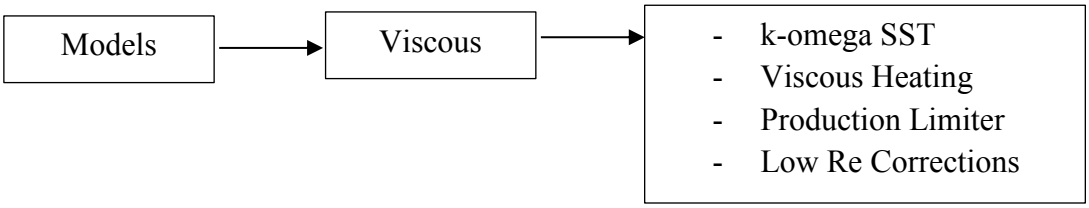

4- Change Material Properties

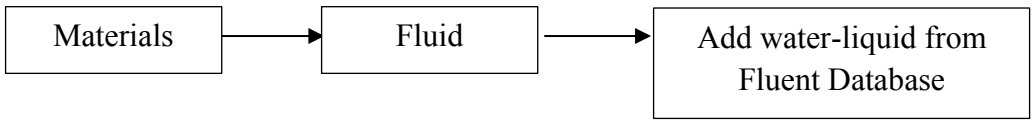

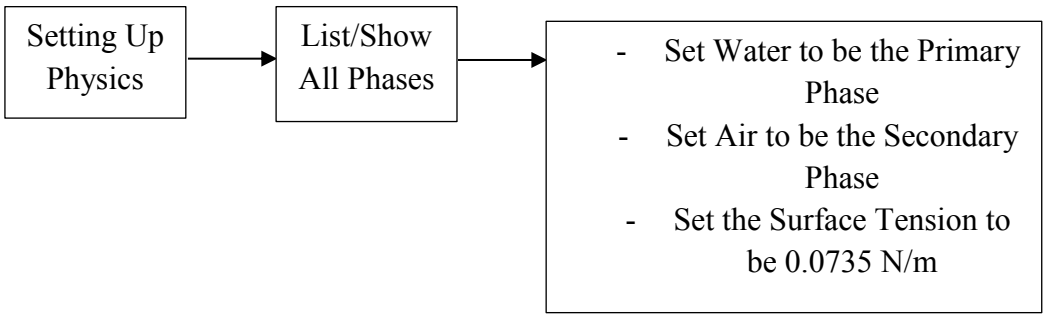

5- Setting the Cell Zone Conditions

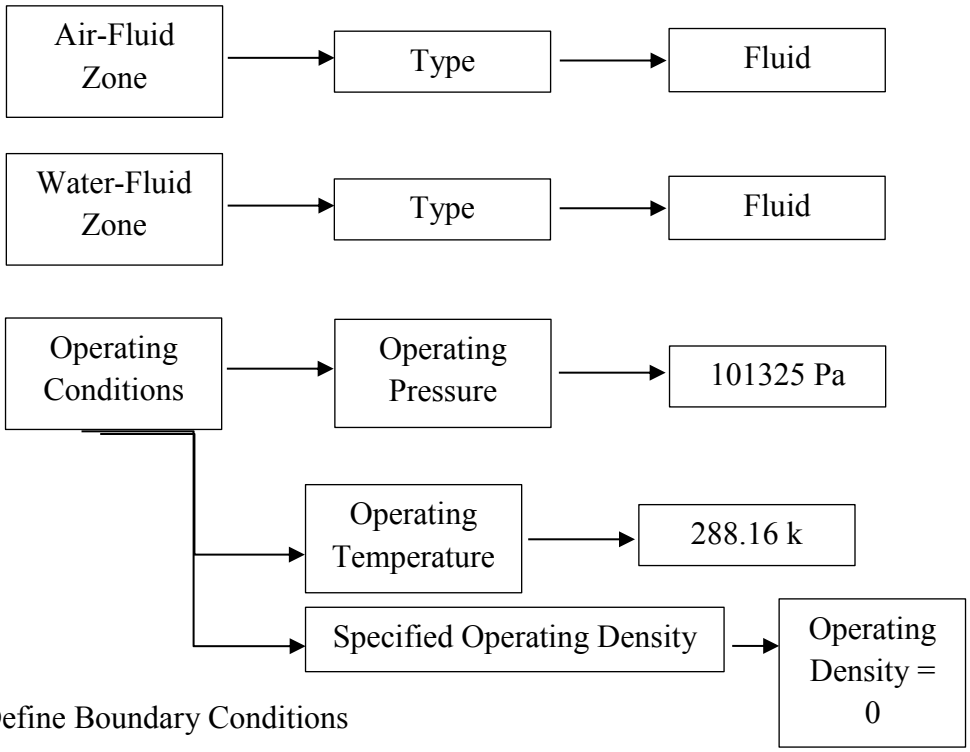

6- Define Boundary Conditions

Before defining the boundary conditions, check that they are defined correctly in the Workbench Meshing.

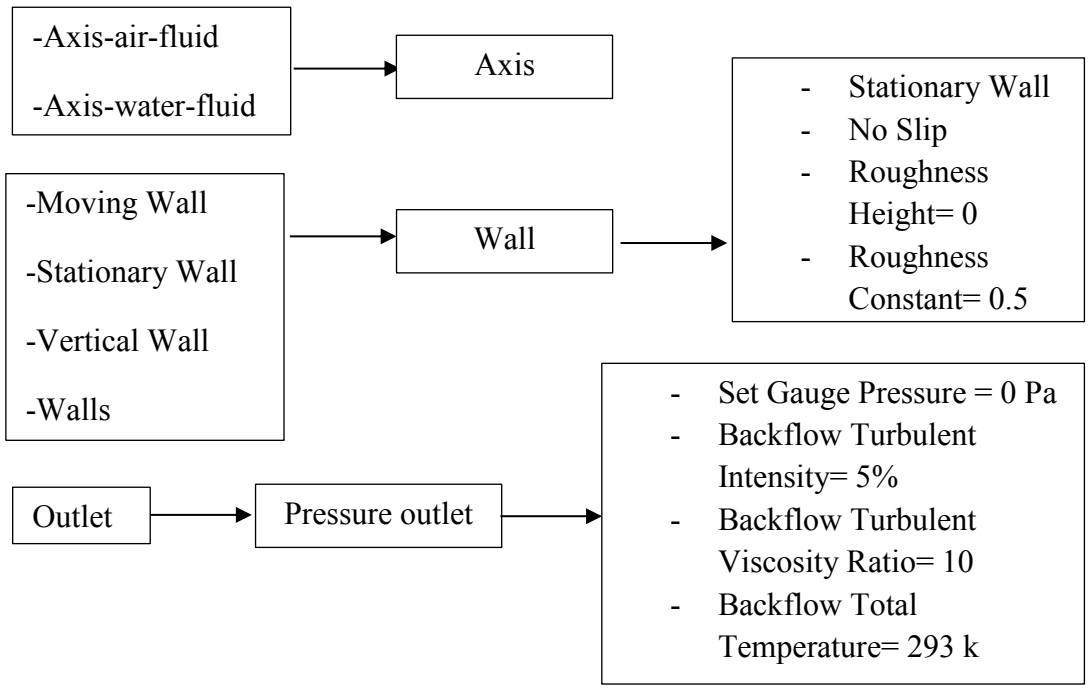

7- Defining the Dynamic Mesh

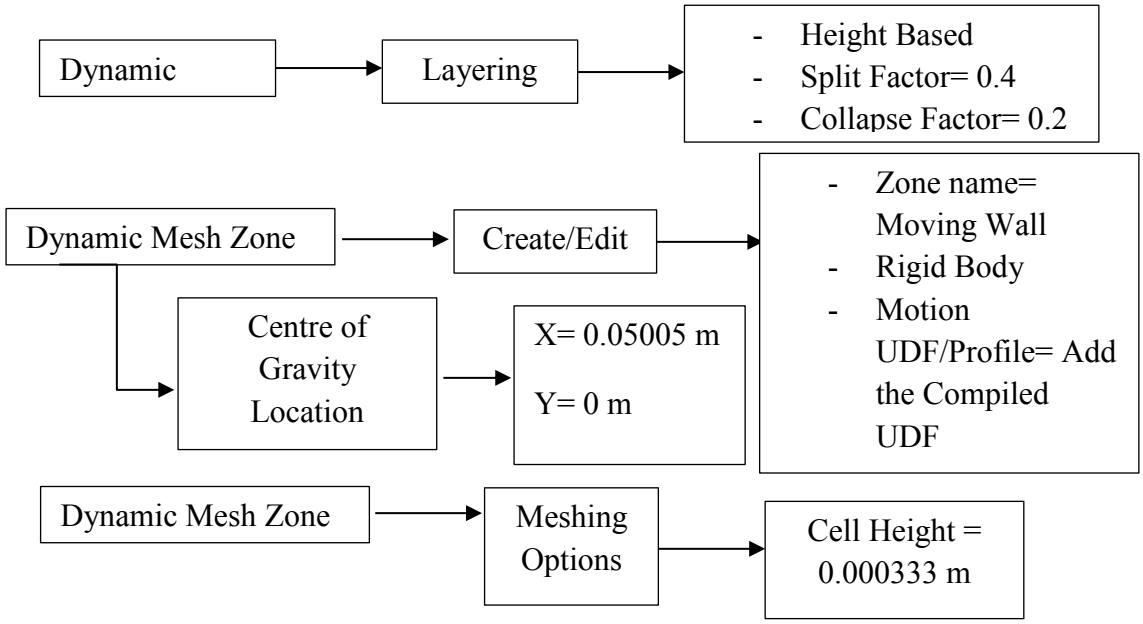

8- Solution Methods

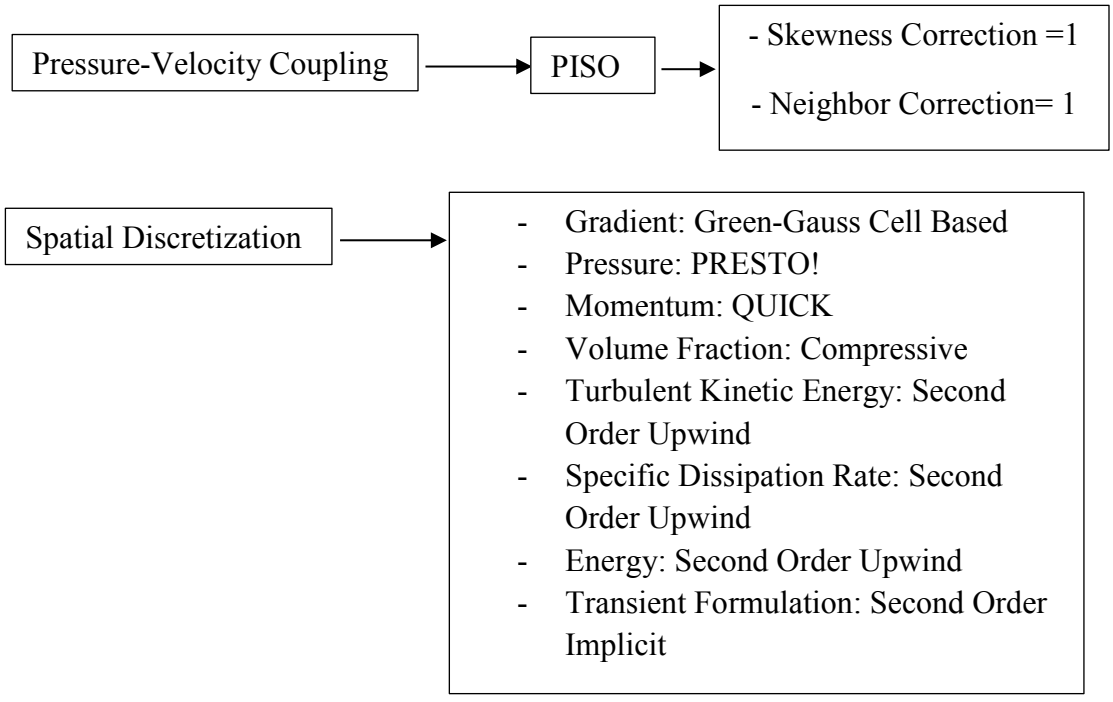

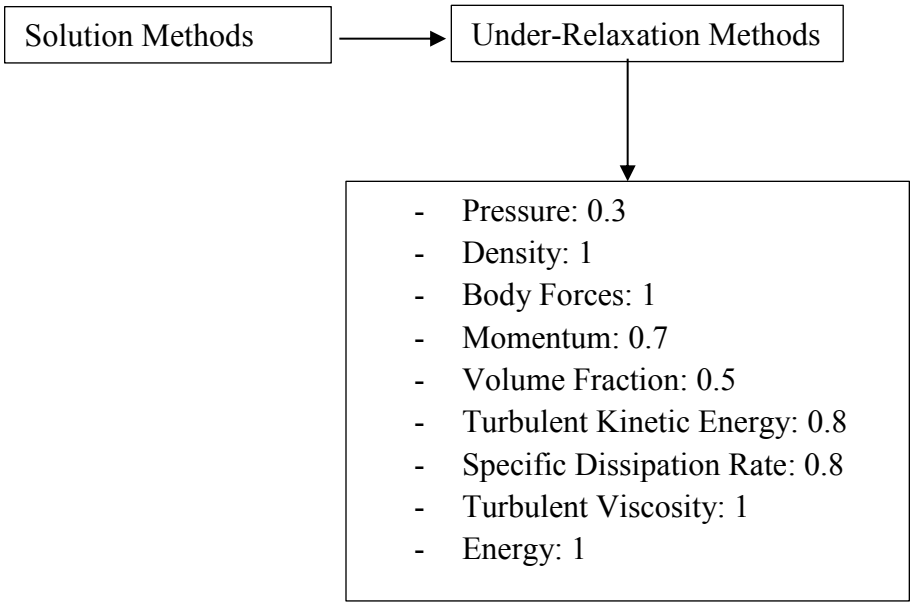

9- Monitors Definition

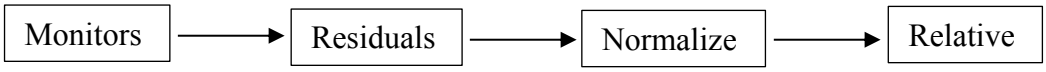

All the Equations are solved using a 10^{-3} Convergence Criteria except Energy which is solved using 10^{-6}.

All the surface monitors are defined as follows:

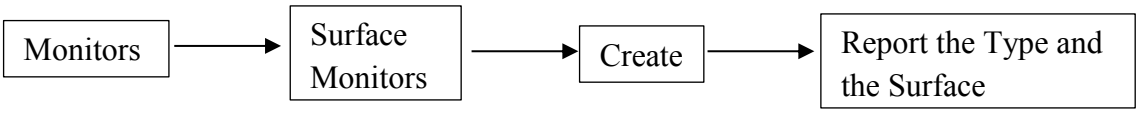

The volume flow rate at the orifice inlet, the secondary inlet and at the shroud outlet are monitored. Also, the axial velocity along the axis at one diameter and one and a half diameters away from the orifice exit are reported. Finally, the axial velocity in the middle of the secondary flow gap at one diameter and one and half diameter away from the orifice are also reported.

10- Solution Initialization

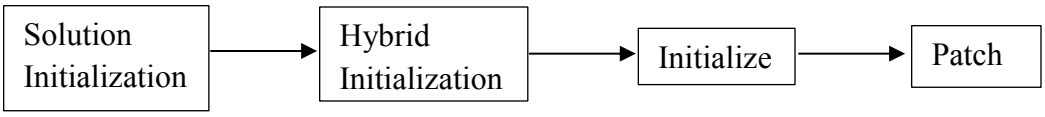

Then, the volume fraction for water and air are specified for each zone. Also, the temperature for both zones are set to be equal to 22℃, which is the room temperature.

11- Save Data and Case File Automatically

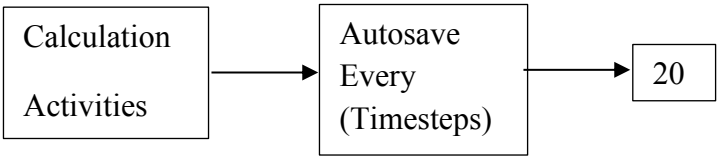

12- Start Iteration

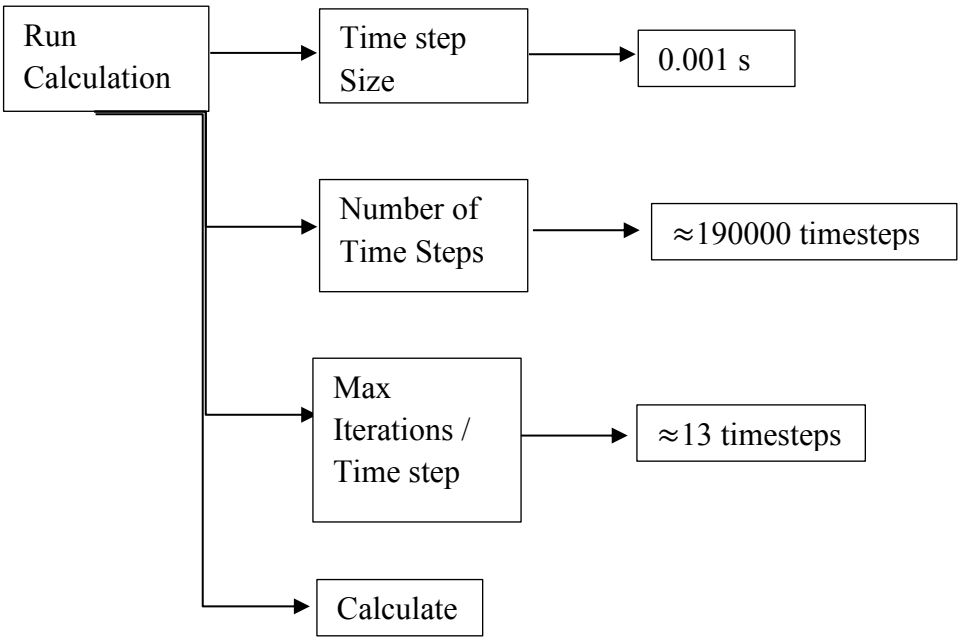

For this simulation, about 300 iterations per timestep are needed to achieve convergence in the beginning of the simulation, then it is reduced to 13 iterations per timestep.

Appendix F

TURBULENCE MODELLING LITERATURE REVIEW

Since the convection and diffusion associated with jets, in general, cause a large difference between the production and the dissipation of turbulence, the mixing length model does not accurately describe the turbulence within jets. Thus, other methods must be used to consider turbulence in jets [82].

F.1 k- ε Model

The k- ε model computes the turbulent kinetic energy explicitly and consists of two governing equations. Equation F.1 describes the turbulent flow kinetic energy (k). It is derived from the Navier-Stokes equation, and is given as follows [83],

$$\frac{\delta k}{\delta t} + U_j \frac{\delta k}{\delta X_j} = [\, \tau_{ij} \frac{\delta U_i}{\delta X_j} - \varepsilon] + \frac{\delta}{\delta X_j} \left[\left(\nu + \frac{\nu_{turb}}{C_k} \right) \frac{\delta k}{\delta X_j} \right] \qquad \textit{(F.1)}$$

The terms on the left-hand side represents the rate of increase of turbulent kinetic energy and the convective transport respectively. The ($\tau_{ij} \frac{\delta U_i}{\delta X_j} - \varepsilon$) term on the right side of the equation represents the rate of destruction of k due to turbulence production. The ($\frac{\delta}{\delta X_j} \nu$) term represents the molecular diffusion of k. The ($\frac{\delta k}{\delta X_j} \frac{\nu_{turb}}{C_k}$) term represents the turbulent diffusion of k. Equation F.2 describes the energy dissipation (ε), and is given as follows,

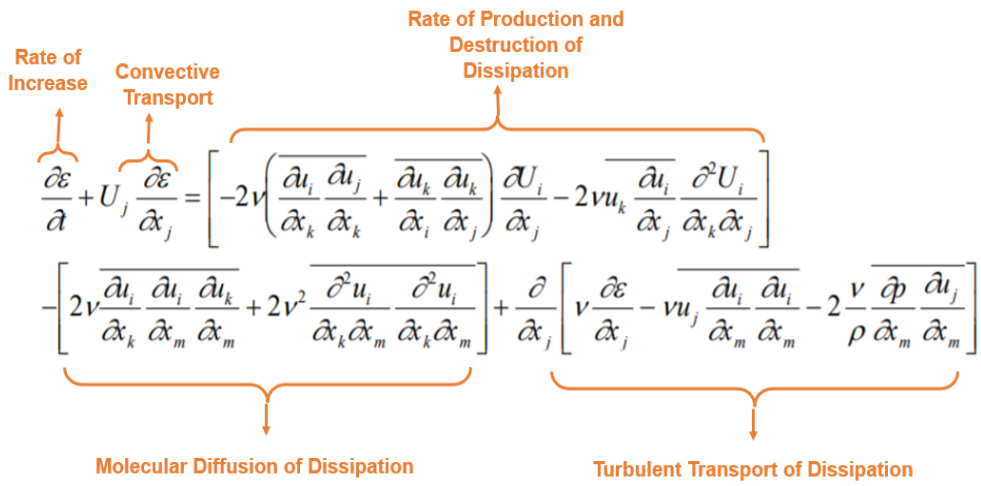

$$\frac{\partial \varepsilon}{\partial t}+U_j\frac{\partial \varepsilon}{\partial x_j}=\left[-2\nu\left(\overline{\frac{\partial u_i}{\partial x_k}\frac{\partial u_j}{\partial x_k}}+\overline{\frac{\partial u_k}{\partial x_i}\frac{\partial u_k}{\partial x_j}}\right)\frac{\partial U_i}{\partial x_j}-2\nu\overline{u_k\frac{\partial u_i}{\partial x_j}\frac{\partial^2 U_i}{\partial x_k\partial x_j}}\right]$$
$$-\left[2\nu\overline{\frac{\partial u_i}{\partial x_k}\frac{\partial u_i}{\partial x_m}\frac{\partial u_k}{\partial x_m}}+2\nu^2\overline{\frac{\partial^2 u_i}{\partial x_k\partial x_m}\frac{\partial^2 u_i}{\partial x_k\partial x_m}}\right]+\frac{\partial}{\partial x_j}\left[\nu\frac{\partial \varepsilon}{\partial x_j}-\nu\overline{u_j\frac{\partial u_i}{\partial x_m}\frac{\partial u_i}{\partial x_m}}-2\frac{\nu}{\rho}\overline{\frac{\partial p}{\partial x_m}\frac{\partial u_j}{\partial x_m}}\right] \quad (F.2)$$

The k- ε model is considered to be one of the simplest and the most used turbulence models in CFD applications. Rodi [84] and Lam et al. [85] claimed that for high Reynolds number, which is the case for wall jet flows, for the standard wall functions, the y+ value of the model must be above 11 in order to satisfy the log-law of the wall. In 1993, Wilcox showed some of the disadvantages of using the k- ε model [86,87]. It was proven that the k- ε model does not perform well for unconfined flows. Furthermore, Chang et al. [88] demonstrated that the k- ε model is unable to accurately predict the formation and development of curved boundary layers, swirling flows and vortex flows.

F.2 k-ω Model

Similar to the k- ε model, this model consists of two governing equations. The first equation is the same turbulent flow kinetic energy (k) as that given in Equation F.1. The second equation describes the specific dissipation rate (ω), given in Equation F.3 as follows,

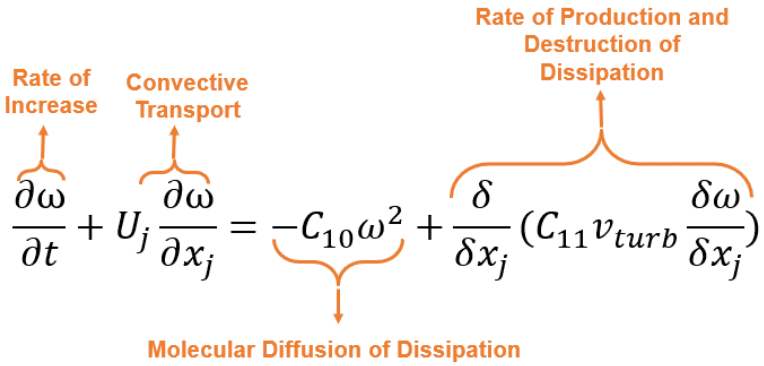

(F.3)

The C_{10} and C_{11} closure coefficients depend on the region, initial and boundary conditions, where the turbulence models are applied. The derivation of those coefficients are explained in detail by Wilcox [86]. It has been proven [89] that the k- ω gives better and more reliable results for the curved flows and the complex wall jet flows than the k- ε model. However, the k- ω is considered to be more computationally intensive and having very large computing costs [90]. Moreover, there is no guarantee that the k- ω model performs better than the k- ε model, particularly for axisymmetric jets and other unconfined recirculating flow applications [91]. There are two main models that were developed based on the k- ω model in order to develop economical methods for the aerospace applications. Wilcox, in 1994, [92] and Menter in 1992 [89] developed the modified k- ω model and the shear stress transport (SST) models respectively. In what follows, only the SST model is discussed in detail.

F.3 SST Model

Generally, the k- ε model gives similar results to the k- ω model except for the flow regions near the walls, where the boundary layers developed. This led to the development of the SST Model, which is a combination of the k- ω and the k- ε model. As described by Menter et al. [75], the standard k- ε model applies far from the wall region,

and the k- ε transforms into a k- ω near the wall region through two blending functions as follows described in Fluent theory guide [93].

The general formula for the SST model is shown in Equation F.4 [75].

$$\frac{\partial(\rho\omega)}{\partial t} + div(\rho\omega U) = div\left[\left(\mu + \frac{\mu_t}{\sigma_{w1}}\right) grad(\omega)\right] + \gamma_2\left(2\rho S_{ij}.S_{ij} - \frac{2}{3}\rho\omega\frac{\partial U_i}{\partial x_j}\delta_{ij}\right) - \beta\rho\omega^2 + 2\frac{\rho\,\partial k\,\partial\omega}{\sigma_{w2}\,\omega\,\partial x_k \partial x_k} \quad \textbf{(F.4)}$$

The constants can be defined as follows:

$$\sigma_{w1} = 1, \quad \sigma_{w2} = 2, \quad \gamma_2 = 0.44, \quad \beta = 0.083$$

One of the main advantages of the SST model is that it includes some limiter functions. These limit the eddy viscosity to give improved performance to flows with adverse pressure gradients and in wake regions. Moreover, it limits the turbulent kinetic energy production to prevent turbulence production and dissipation in stagnation regions [75,90]. The limiting equations are presented and described in Fluent theory guide [93].

Appendix G

COMPLETE SET OF EXPERIMENTAL RESULTS

This section presents the remainder of the results that are not shown in Chapter 5 (at dimensionless times of 0, 0.1, 0.3, 0.4, 0.6, 0.7 and 0.9).

G.1 Period-Averaged Volume Flow Rate Exported from Fluent

This subsection includes the MATLAB code used to extract the period-averaged volume flow rate results from the monitors in Fluent for the improved and the simplified CFD numerical models.

```
clc
clear

A1=importdata('surf-mon-1.out');    %Loads surface monitor file
(actuator-outlet)
A2=importdata('surf-mon-2.out');    %Loads surface monitor file
(secondary-flow)
A3=importdata('surf-mon-3.out');    %Loads surface monitor file (shroud-
outlet)
% A4=importdata('surf-mon-4.out');    %Loads surface monitor file
(Average axial velocity through the actuator)
B1=A1.data(:,:);                    %B1 extracts the numerical data from
A1
B2=A2.data(:,:);                    %B2 extracts the numerical data from
A2
B3=A3.data(:,:);                    %B3 extracts the numerical data from
A3
% B4=A4.data(:,:);                    %B4 extracts the numerical data
from A4
n=1769;                             %n is number of timesteps per cycle
l=(size(B1,1))/n;                   %l is number of cycles completed (in
decimals)
m=floor(l);                         %m is number of full cycles
completed (whole number)
t=n-1;

for i=1:m                           %Creating a matrix for plotting avg
vfr against no. of cycle
    O(i,1)=i;
end
```

```
for j=1:m                          %loop for averaging volume flow
rates over a cycle
    S=0;
    if j==1
        p=1;
    else
        p=n*(j-1) + 1;
    end
    for i=p:p+t
        S = S + B1(i,2);
    end
    C1(j,1) = S / n;               %Matrix C1 contains average volume
flow rates for each cycle
end

for j=1:m
    S=0;
    if j==1
        p=1;
    else
        p=n*(j-1) + 1;
    end
    for i=p:p+t
        S = S + B2(i,2);
    end
    C2(j,1) = S / n;
end

for j=1:m
    S=0;
    if j==1
        p=1;
    else
        p=n*(j-1) + 1;
    end
    for i=p:p+t
        S = S + B3(i,2);
    end
    C3(j,1) = S / n;
end

x=O(:,1);
y1=C1(:,1);
y2=C2(:,1);
y3=C3(:,1);

plot(x,y1);
grid on
hold on

plot(x,y2);
grid on
hold on

plot(x,y3);
grid on
```

```
hold off


legend('vfr-actuator-outlet','vfr-sec-flow','vfr-shroud-outlet')

T=[x,y1,y2,y3]

%{
For plotting instantaneous volume flow rates

x=B1(:,1);
y1=B1(:,2);
y2=B2(:,2);
y3=B3(:,2);

plot(x,y1);
grid on
hold on

plot(x,y2);
grid on
hold on

plot(x,y3);
grid on
hold off
legend('vfr-actuator-outlet','vfr-sec-flow','vfr-shroud-outlet')
%}
```

G.2 Mean Flow Fields

This subsection gives the flow field velocity vector images for both the experimental data, the improved CFD numerical simulation and the U_{rms} contours. Figures G.1, G.2, G.3. G.4, G.5, G.6 and G.7 refer to the results at t/T = 0, 0.1, 0.3, 0.4, 0.6, 0.7, 0.9, respectively.

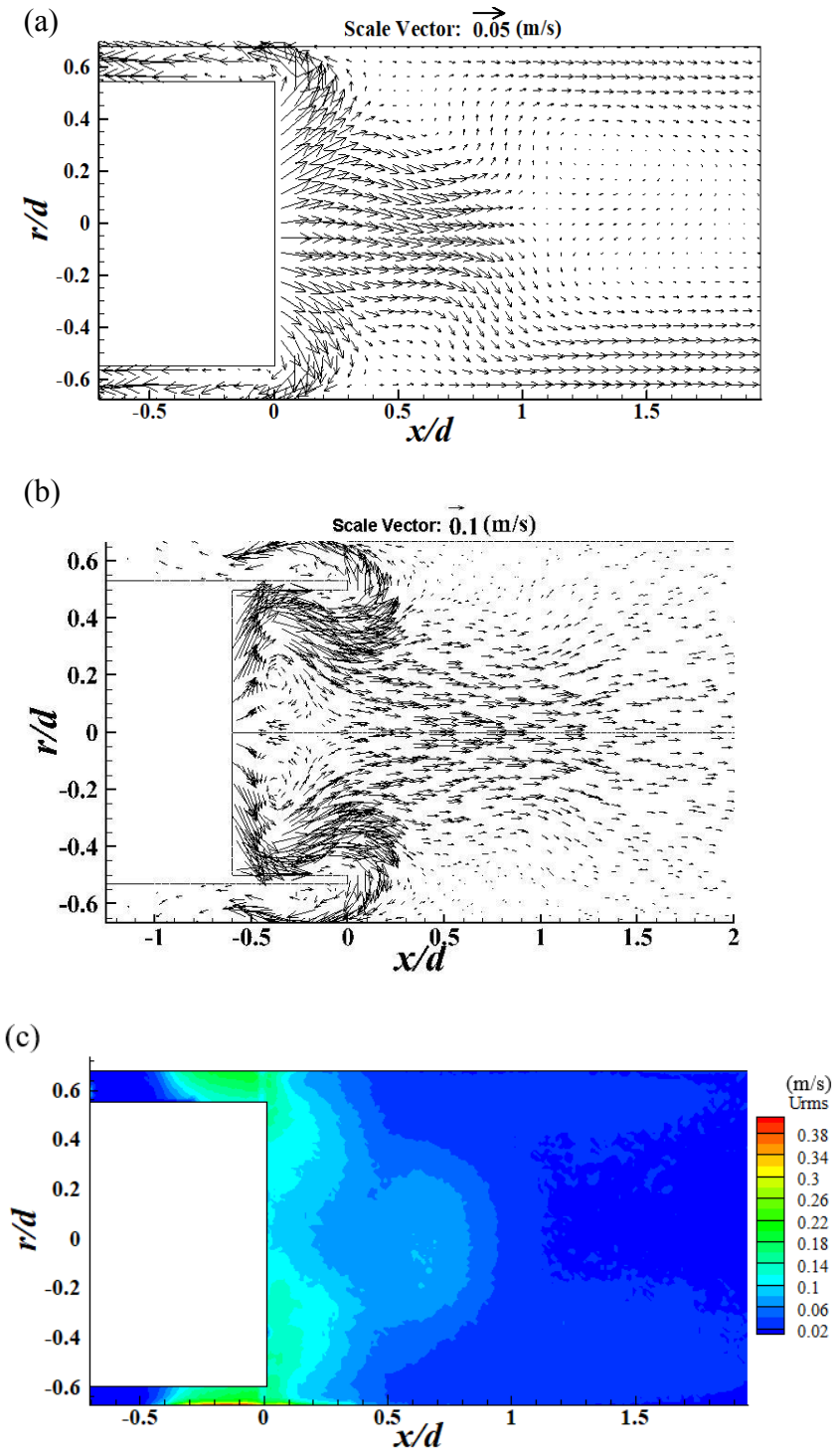

Figure G.1 Velocity Field Vectors Obtained at t/T= 0 from (a) Phase-Averaging, (b) Improved CFD Simulation, (c) U_{rms} Contours

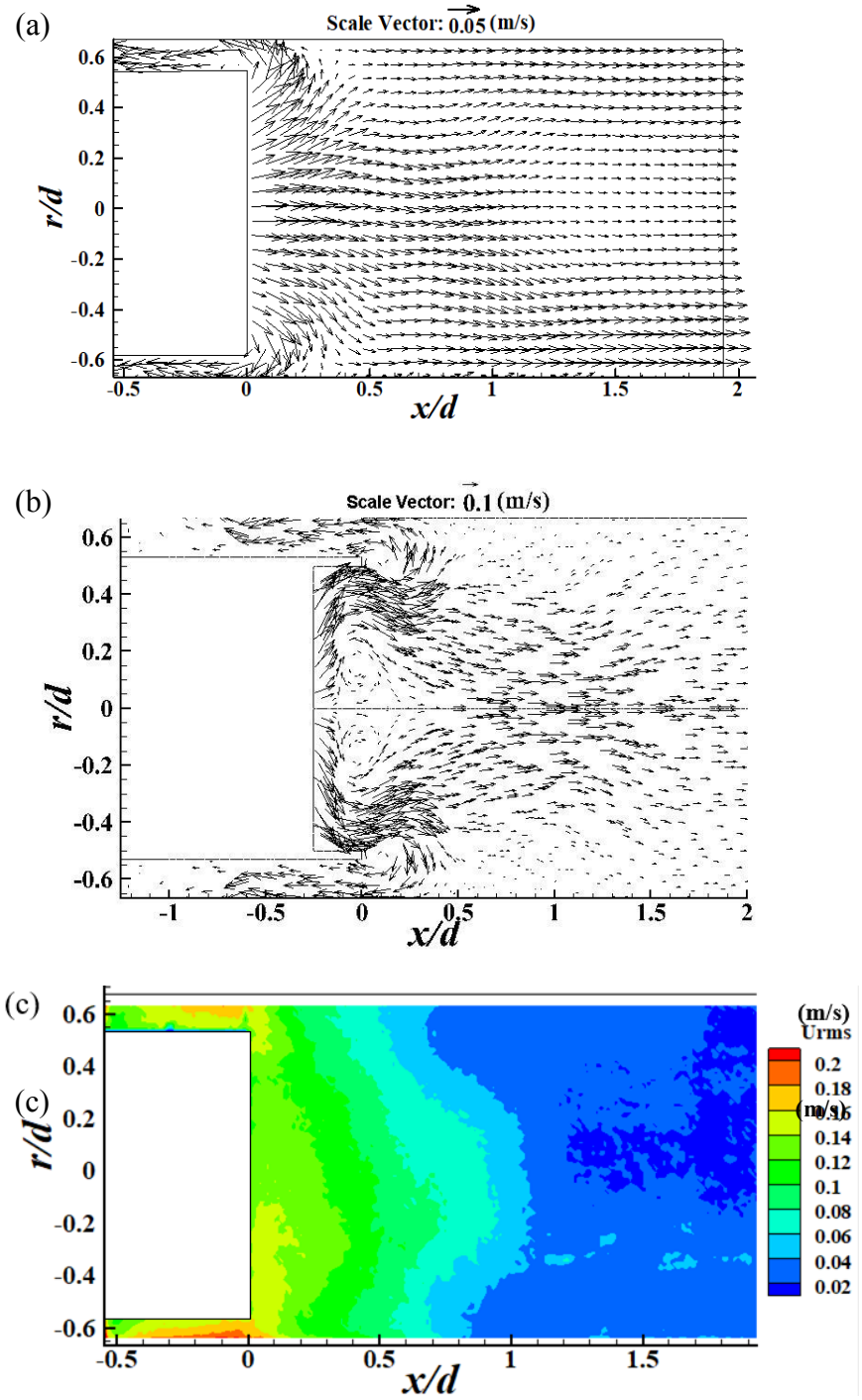

Figure G.2 Velocity Field Vectors Obtained at t/T= 0.1 from (a) Phase-Averaging, (b) Improved CFD Simulation, (c) U_{rms} Contours

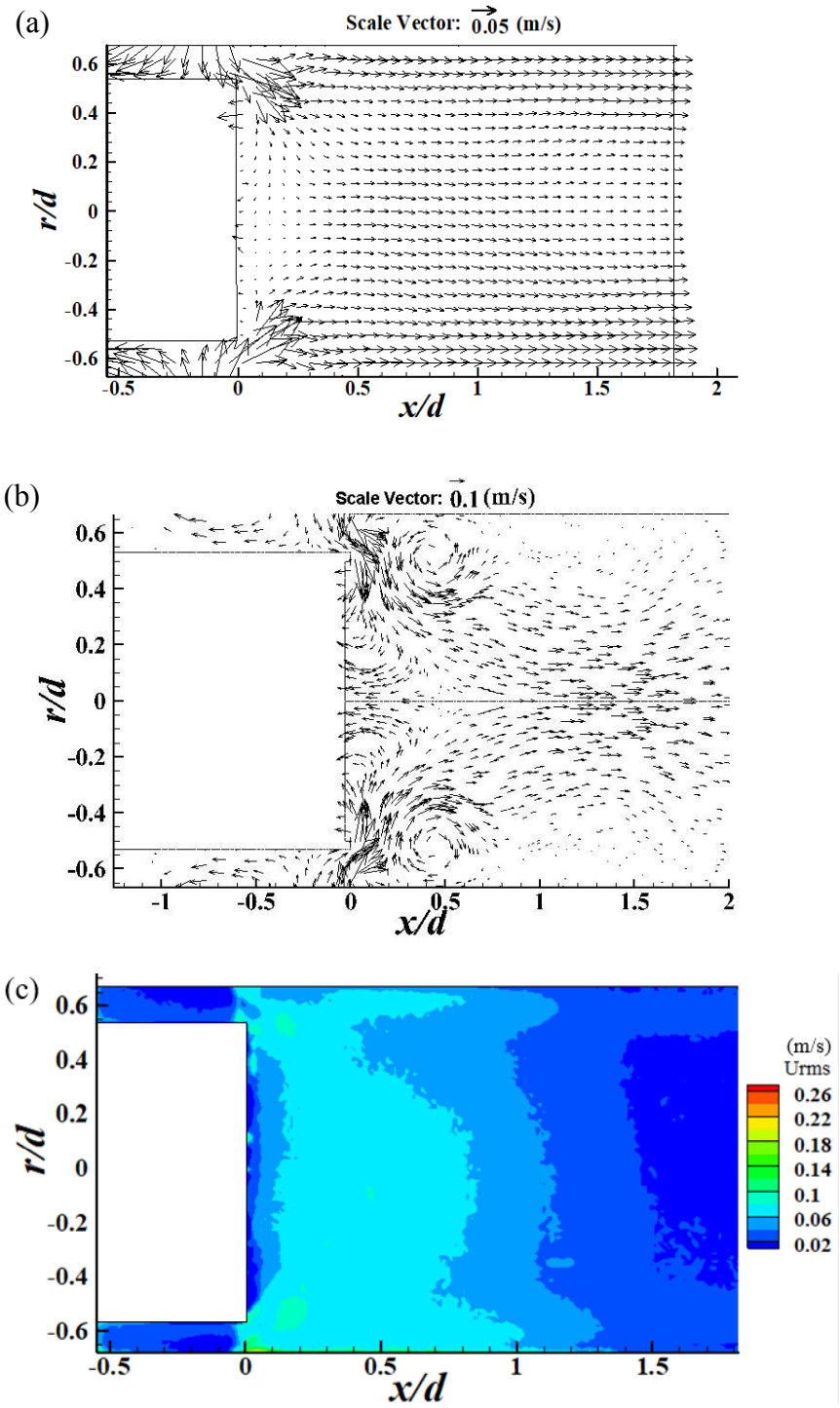

Figure G.3 Velocity Field Vectors Obtained at t/T= 0.3 from (a) Phase-Averaging, (b) Improved CFD Simulation, (c) U_{rms} Contours

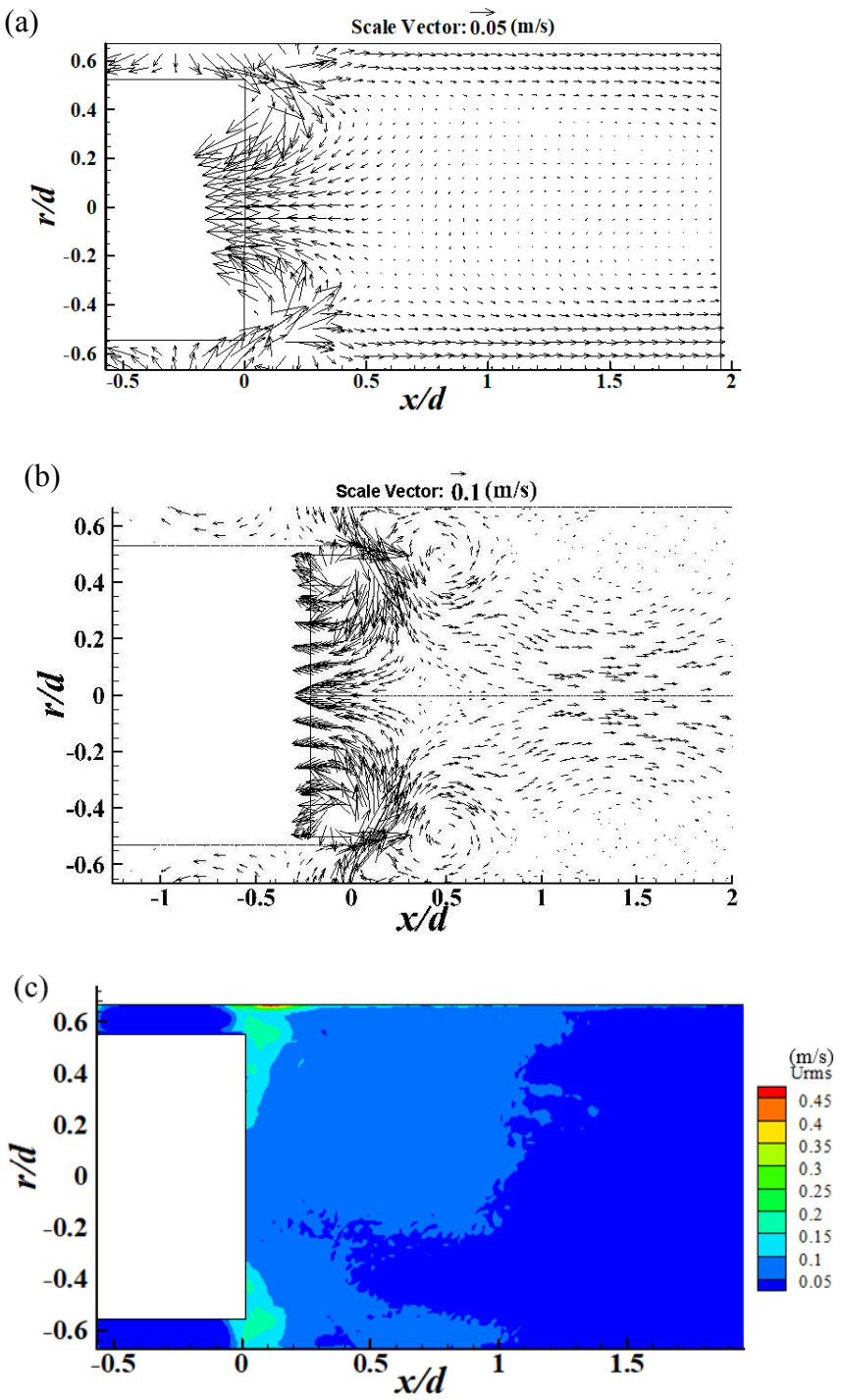

Figure G.4 Velocity Field Vectors Obtained at t/T= 0.4 from (a) Phase-Averaging, (b) Improved CFD Simulation, (c) U_{rms} Contours

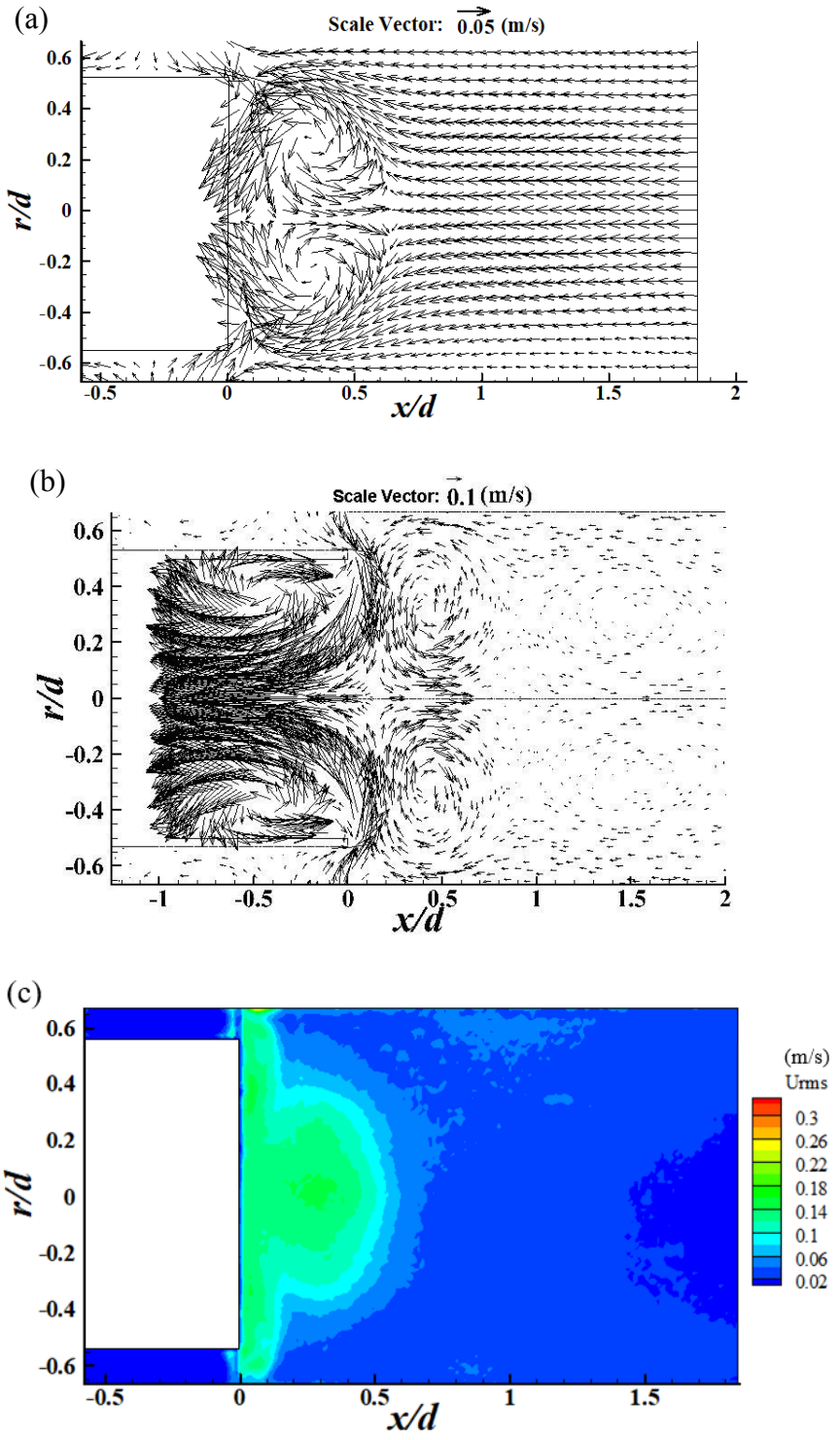

Figure G.5 Velocity Field Vectors Obtained at t/T= 0.6 from (a) Phase-Averaging, (b) Improved CFD Simulation, (c) U_{rms} Contours

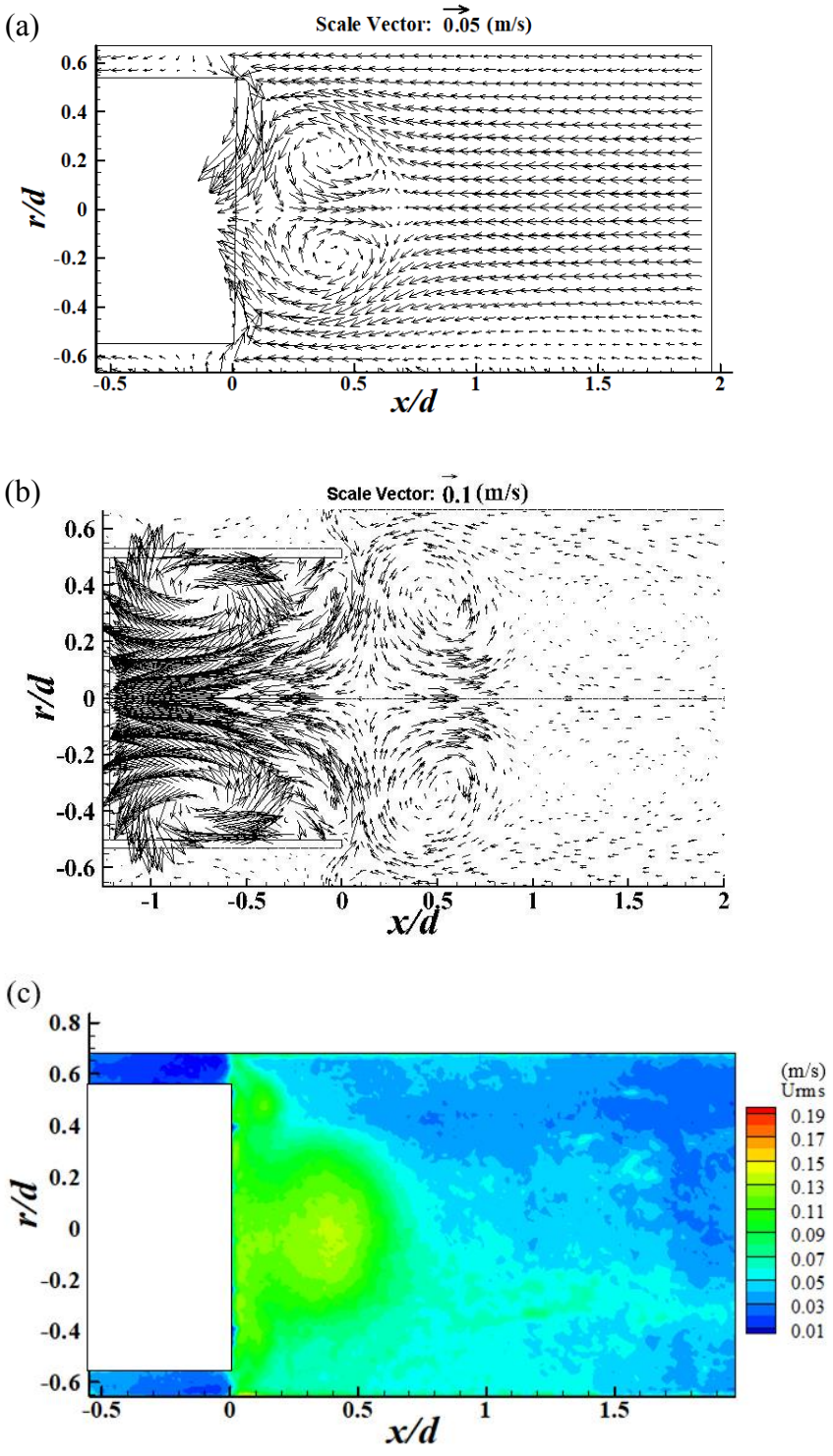

Figure G.6 Velocity Field Vectors Obtained at t/T= 0.7 from (a) Phase-Averaging, (b) Improved CFD Simulation, (c) U_{rms} Contours

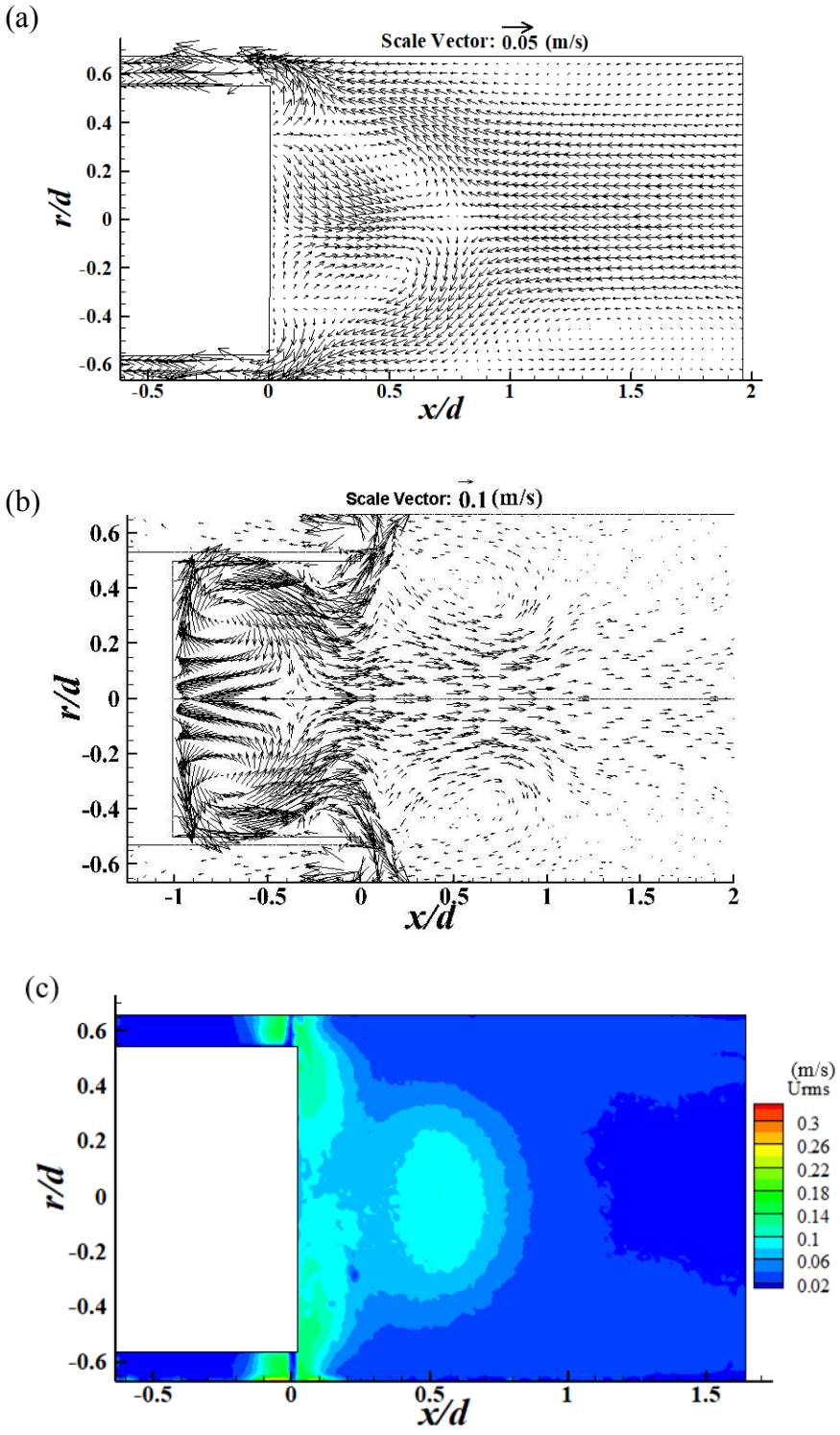

Figure G.7 Velocity Field Vectors Obtained at t/T= 0.9 from (a) Phase-Averaging, (b) Improved CFD Simulation, (c) U_{rms} Contours

G.3 Longitudinal Variation of the Axial Velocity

Figures G.8, G.10, G.12, G.14, G.16, G.18 and G.20 show the longitudinal axial velocity at the points of interest for the experimental results at t/T = 0, 0.1, 0.3, 0.4, 0.6, 0.7, 0.9. While for the improved numerical CFD simulation, Figures G.9, G.11, G.13, G.15, G.17, G.19 and G.21 show the longitudinal axial velocity at the points of interest at t/T = 0, 0.1, 0.3, 0.4, 0.6, 0.7, 0.9.

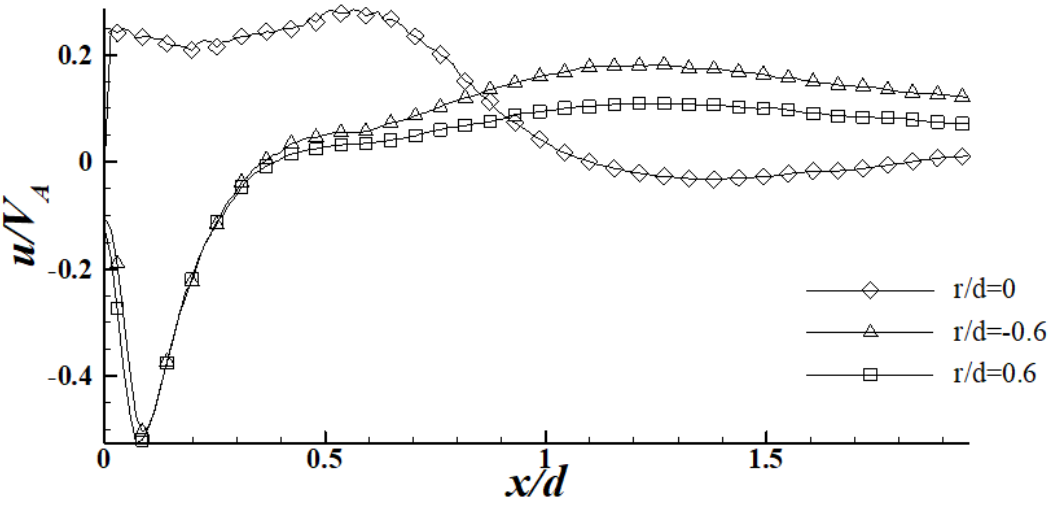

Figure G.8 The Change of the Experimental Dimensionless Axial Velocity Along the Flow Field Downstream at Three Locations at t/T=0

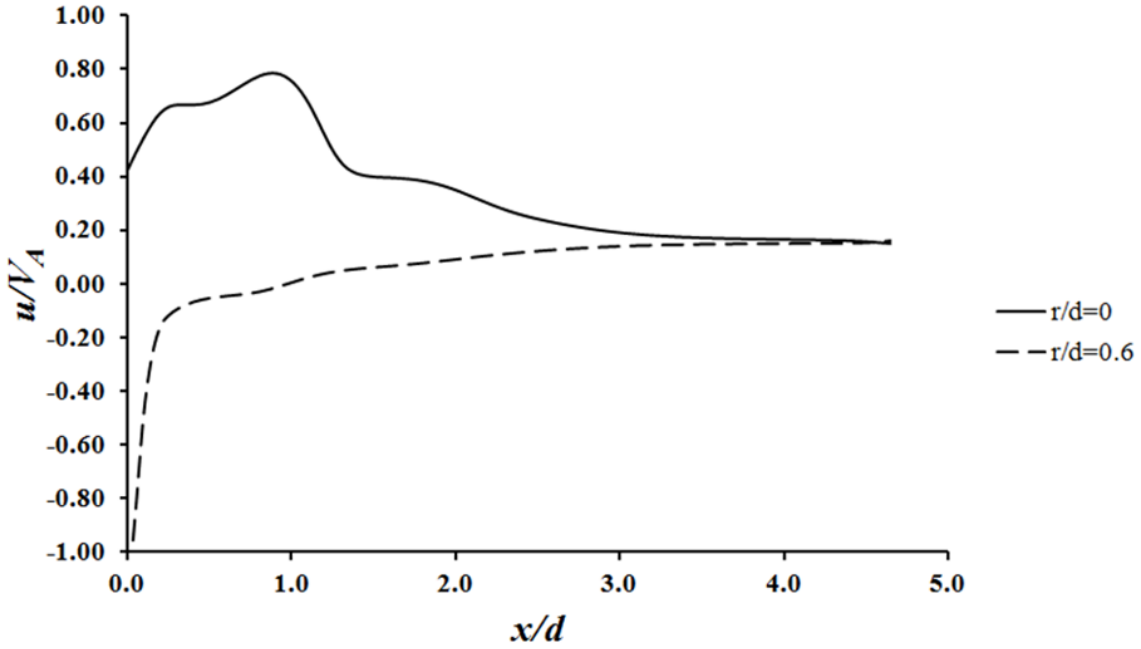

Figure G.9 The Change of the CFD Numerical Dimensionless Axial Velocity Along the Flow Field Downstream at Three Locations at t/T=0

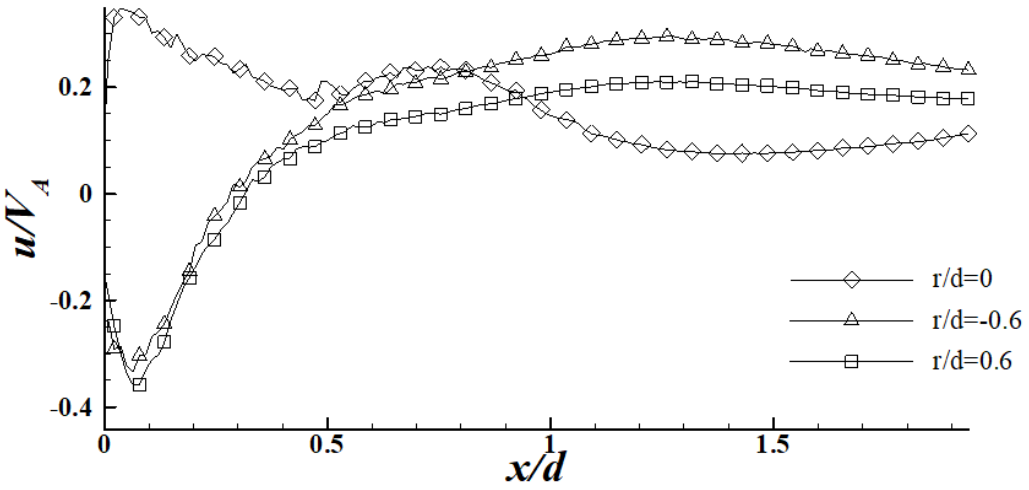

Figure G.10 The Change of the Experimental Dimensionless Axial Velocity Along the Flow Field Downstream at Three Locations at t/T=0.1

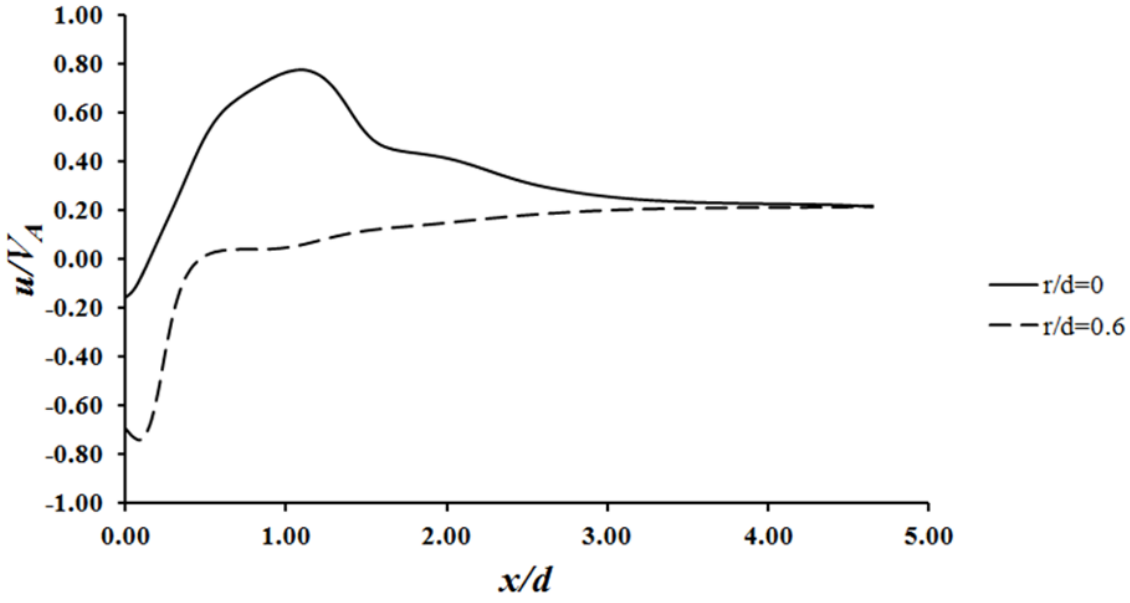

Figure G.11 The Change of the CFD Numerical Dimensionless Axial Velocity Along the Flow Field Downstream at Three Locations at t/T=0.1

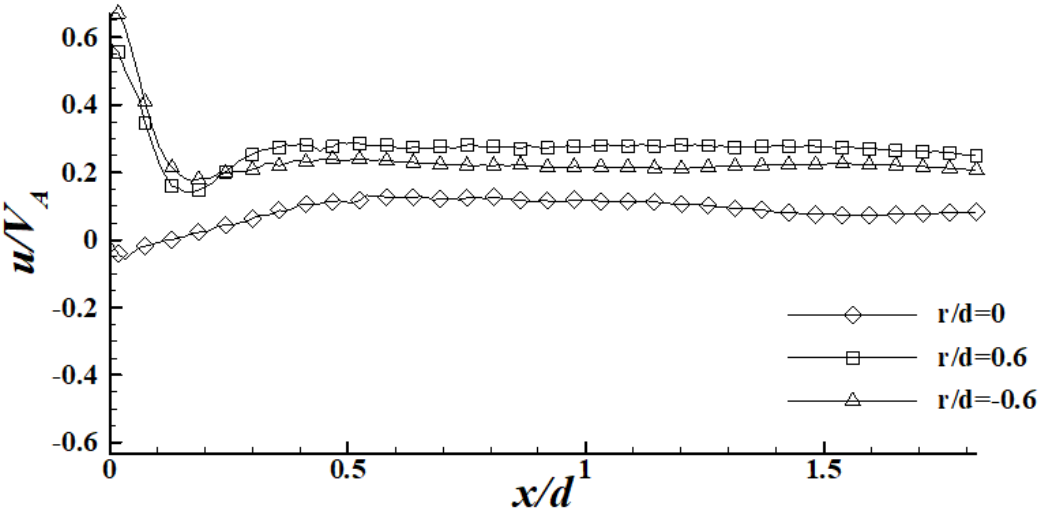

Figure G.12 The Change of the Experimental Dimensionless Axial Velocity Along the Flow Field Downstream at Three Locations at t/T=0.3

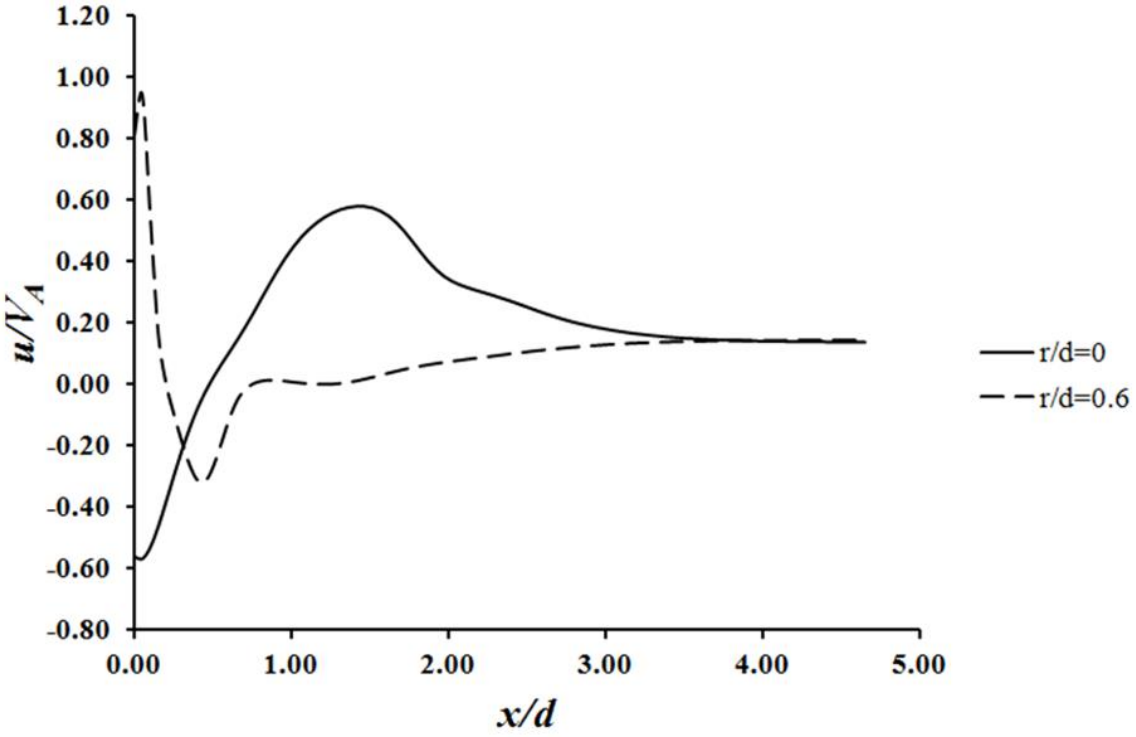

Figure G.13 The Change of the CFD Numerical Dimensionless Axial Velocity Along the Flow Field Downstream at Three Locations at t/T=0.3

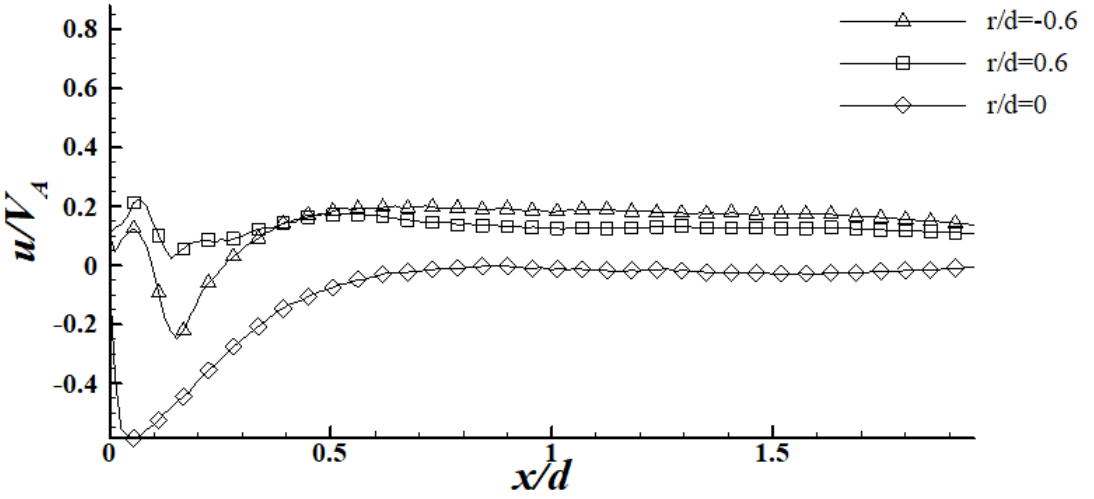

Figure G.14 The Change of the Experimental Dimensionless Axial Velocity Along the Flow Field Downstream at Three Locations at t/T=0.4

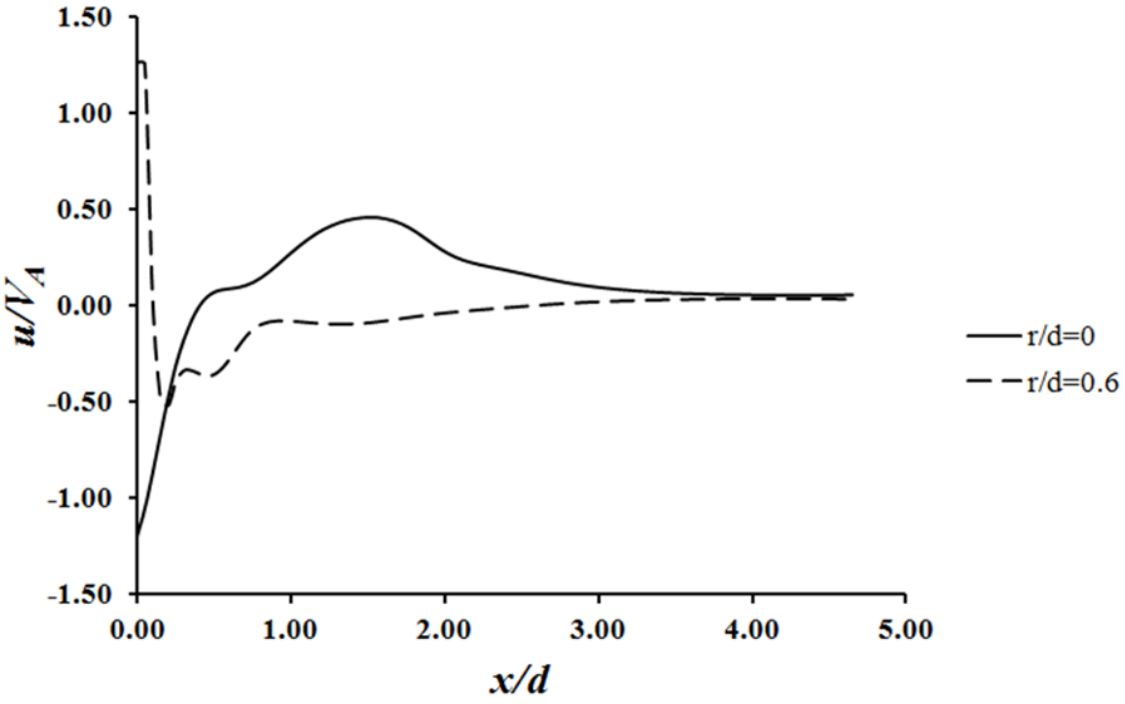

Figure G.15 The Change of the CFD Numerical Dimensionless Axial Velocity Along the Flow Field Downstream at Three Locations at t/T=0.4

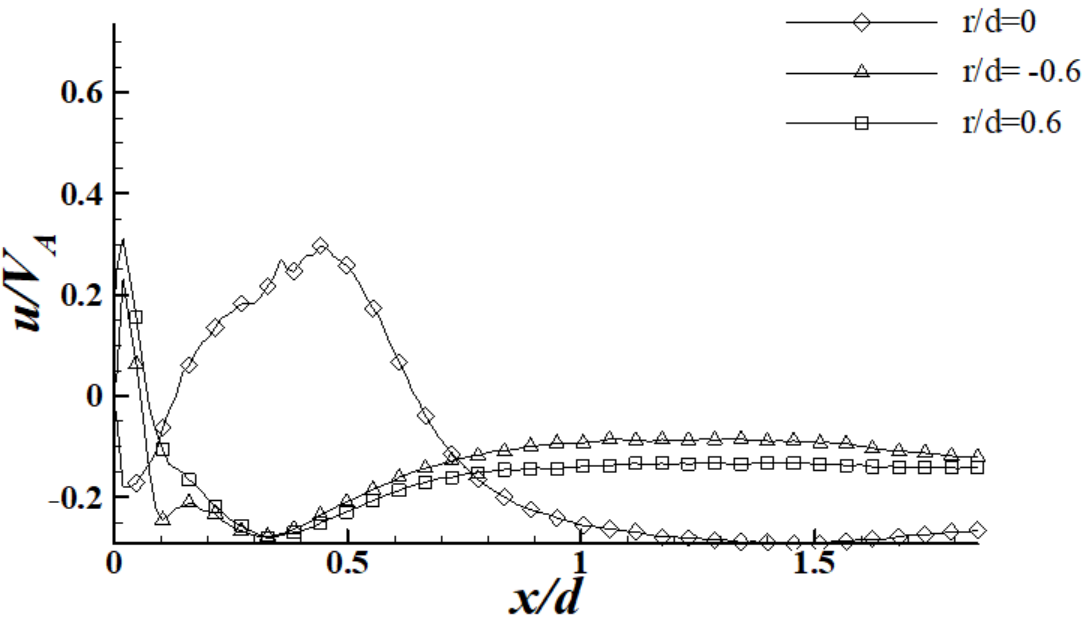

Figure G.16 The Change of the Experimental Dimensionless Axial Velocity Along the Flow Field Downstream at Three Locations at t/T=0.6

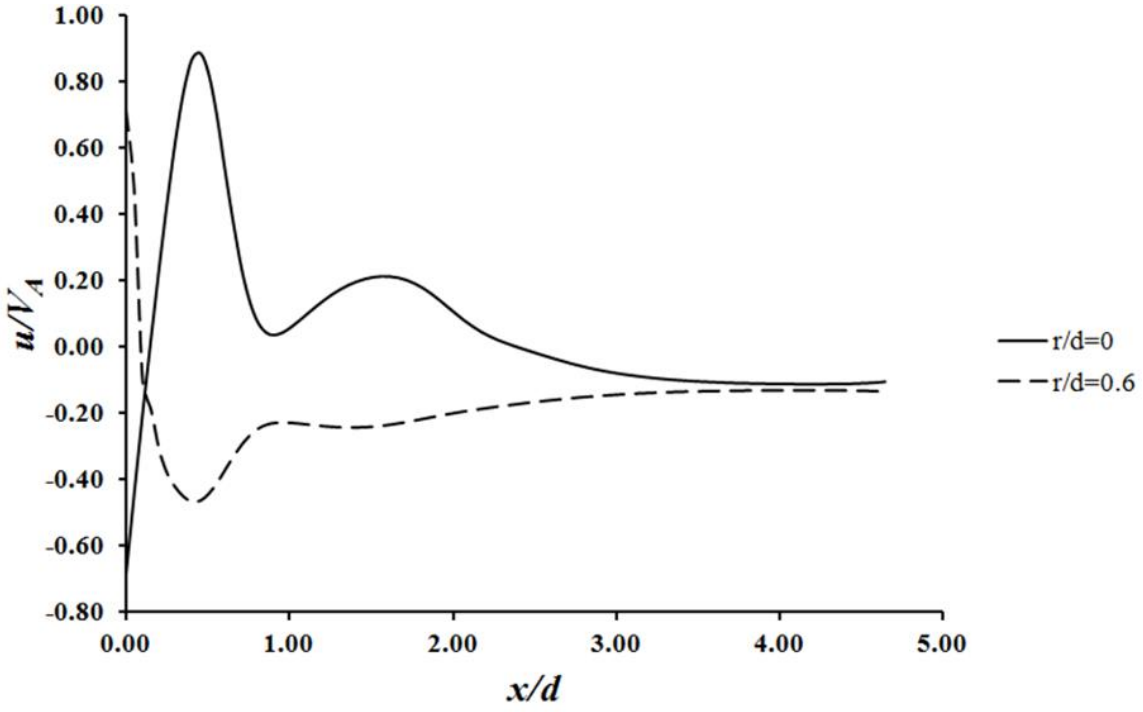

Figure G.17 The Change of the CFD Numerical Dimensionless Axial Velocity Along the Flow Field Downstream at Three Locations at t/T=0.6

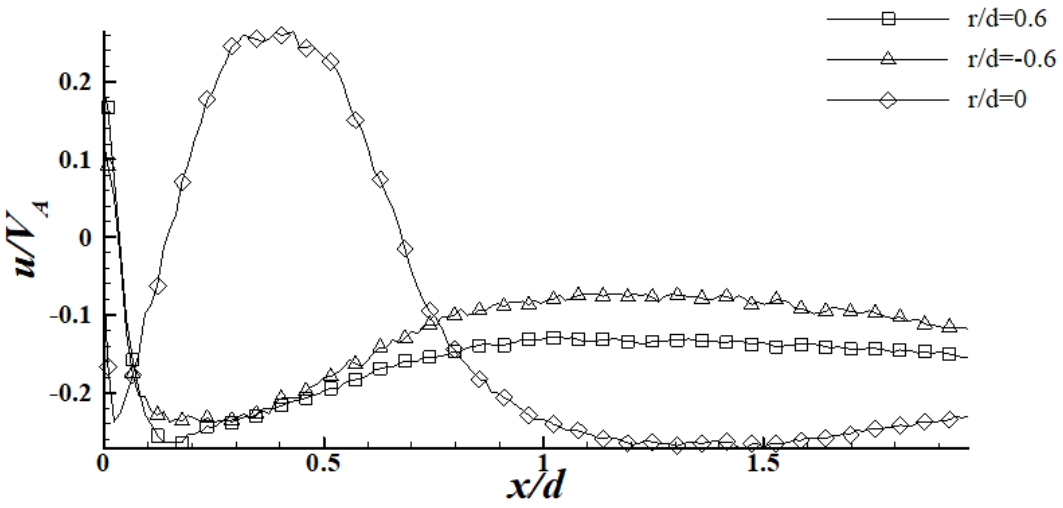

Figure G.18 The Change of the Experimental Dimensionless Axial Velocity Along the Flow Field Downstream at Three Locations at t/T=0.7

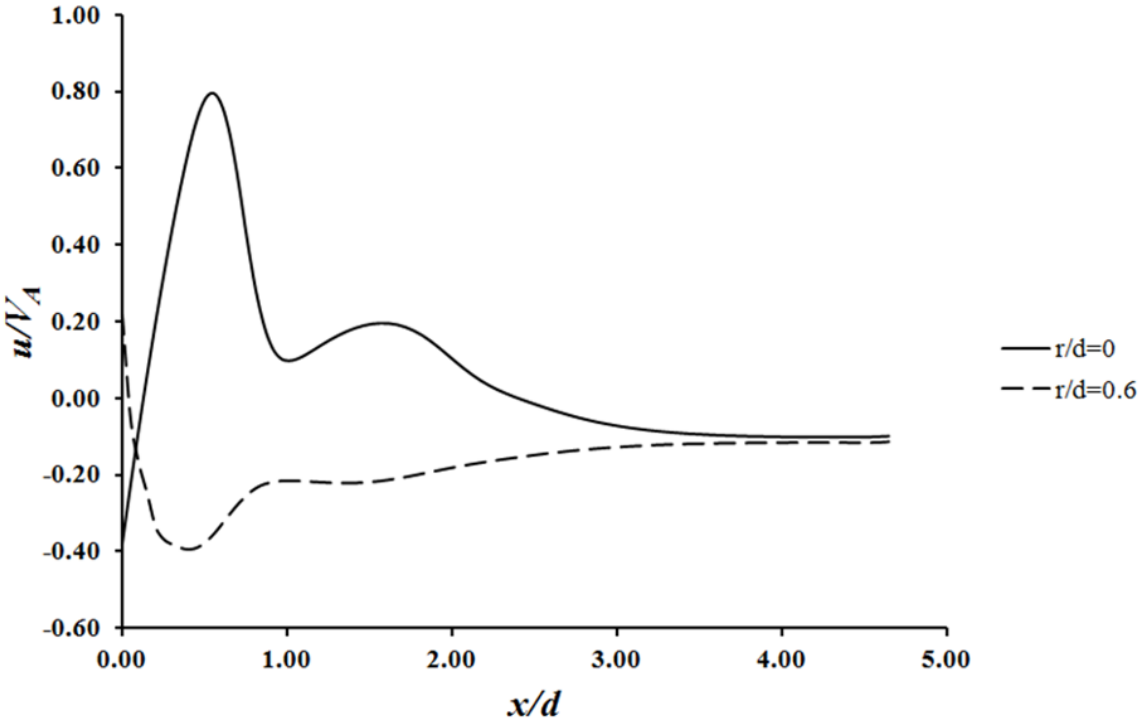

Figure G.19 The Change of the CFD Numerical Dimensionless Axial Velocity Along the Flow Field Downstream at Three Locations at t/T=0.7

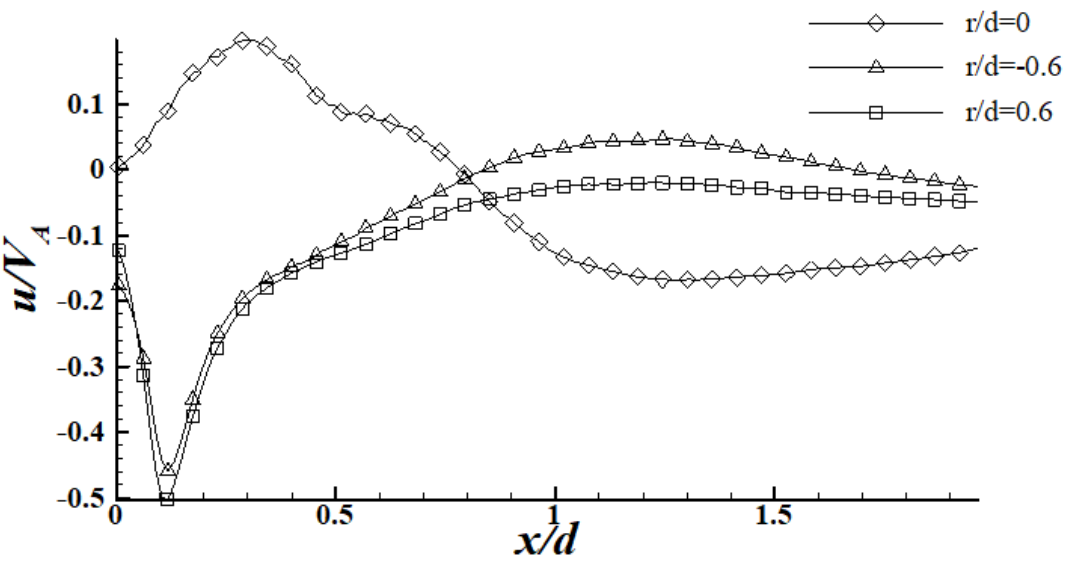

Figure G.20 The Change of the Experimental Dimensionless Axial Velocity Along the Flow Field Downstream at Three Locations at t/T=0.9

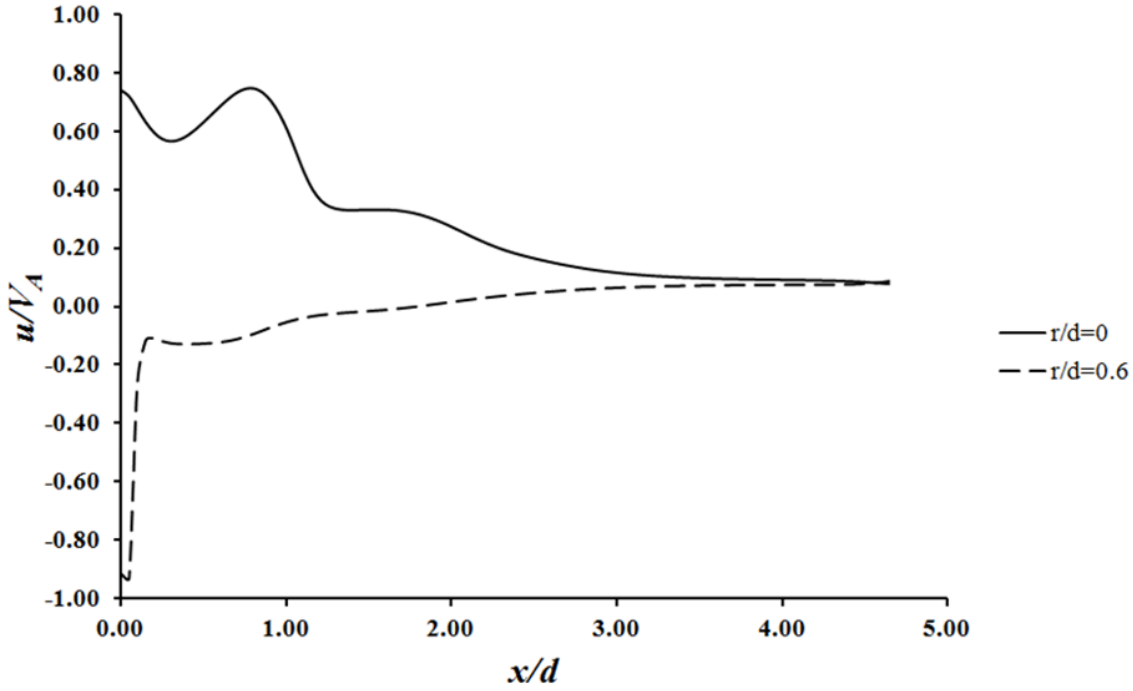

Figure G.21 The Change of the CFD Numerical Dimensionless Axial Velocity Along the Flow Field Downstream at Three Locations at t/T=0.9

G.4 Radial Variation of Axial Velocity

This subsection includes a comparison of the radial axial velocity profiles at x/d = 1.75 for the experimental and the numerical results. Figures G.22, G.23, G.24, G.25, G.26, G.27 and G.28 show the radial variation of the axial velocity for the phase-averaged data and for the improved numerical model data at t/T = 0, 0.1, 0.3, 0.4, 0.6, 0.7, 0.9, respectively. For the phase-averaged results, the uncertainty is found to equal approximately $\pm$ 0.00159 m/s.

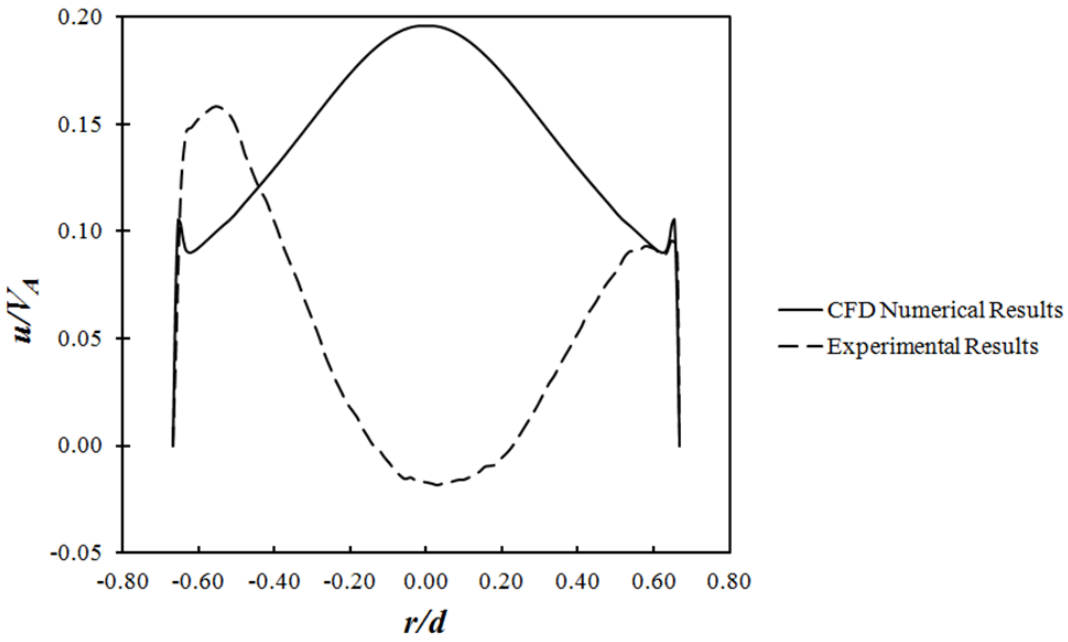

Figure G.22 Velocity Profile Across the Shroud's Diameter at x/d=1.75 for the Experiment and the Numerical Simulation at t/T=0

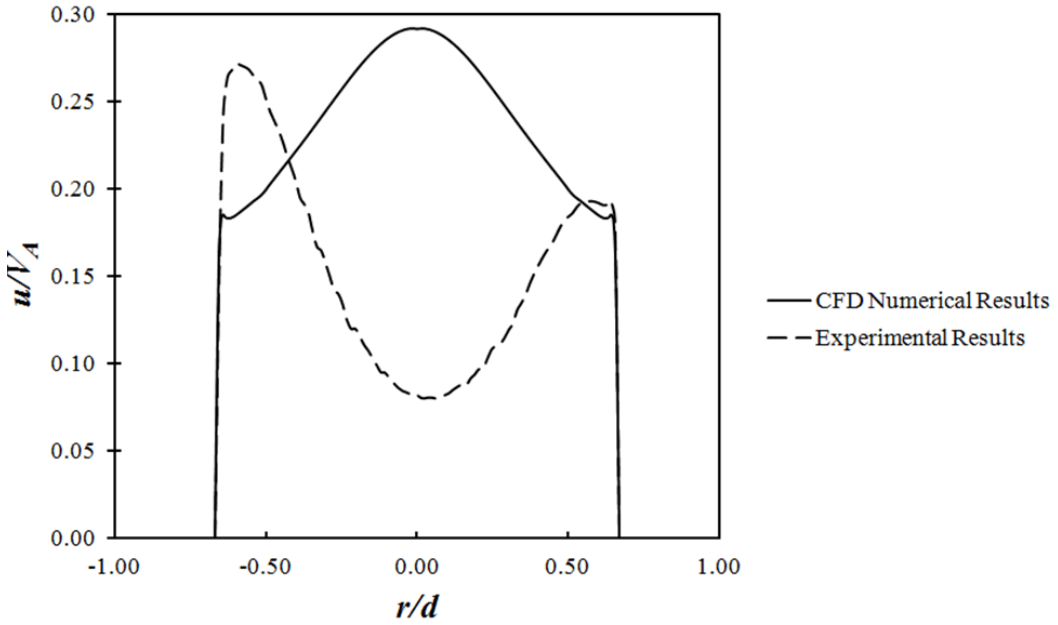

Figure G.23 Velocity Profile Across the Shroud's Diameter at x/d=1.75 for the Experiment and the Numerical Simulation at t/T=0.1

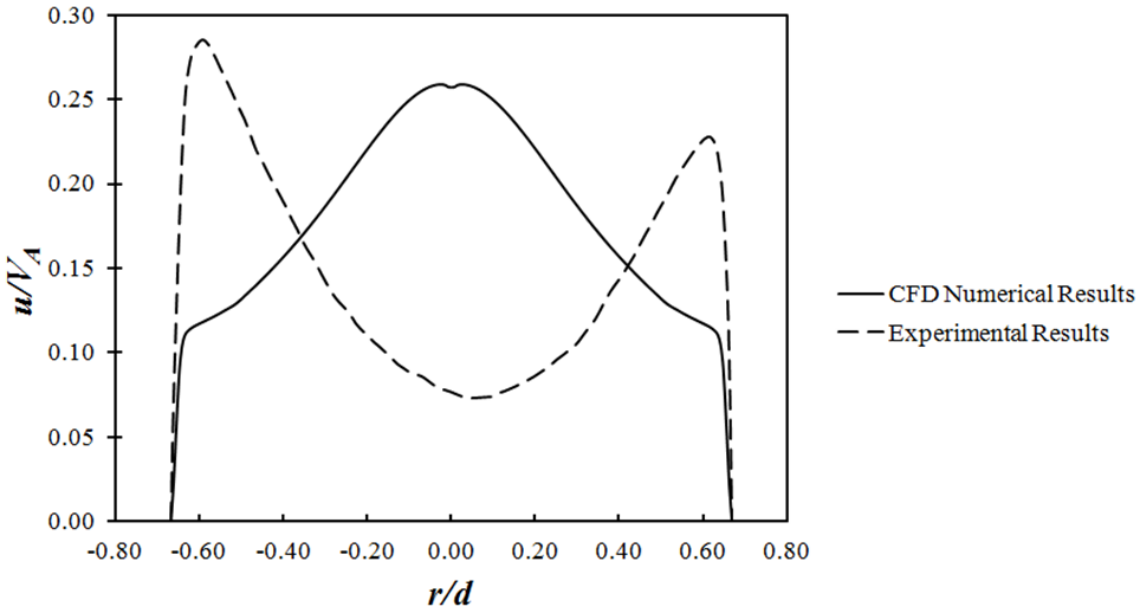

Figure G.24 Velocity Profile Across the Shroud's Diameter at x/d=1.75 for the Experiment and the Numerical Simulation at t/T=0.3

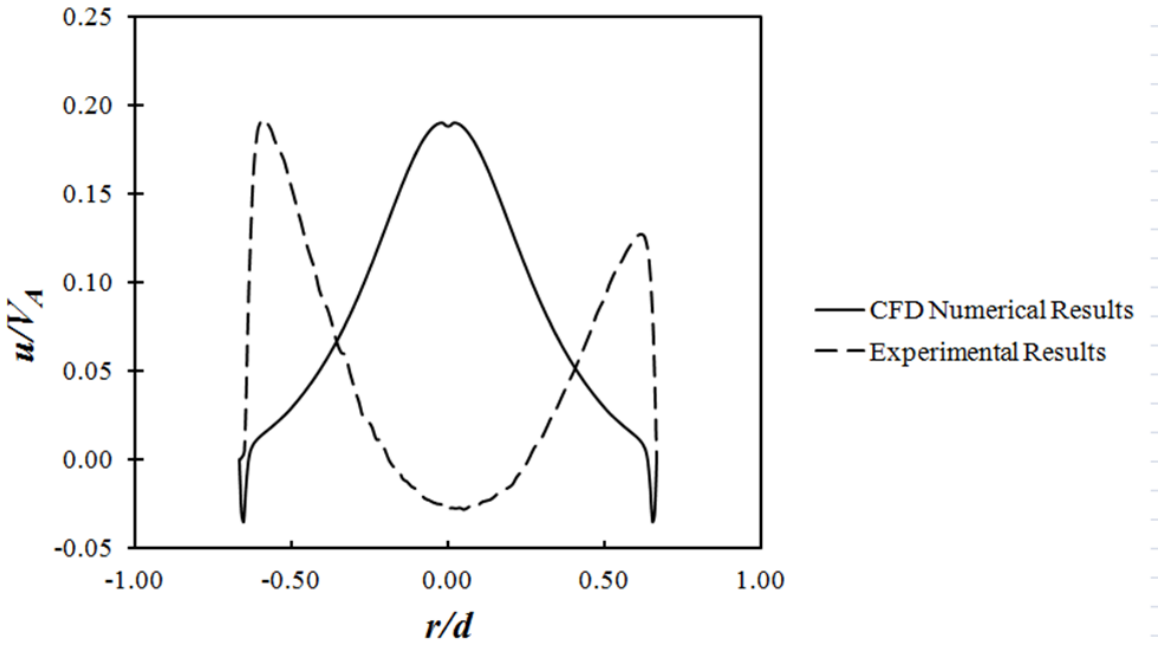

Figure G.25 Velocity Profile Across the Shroud's Diameter at x/d=1.75 for the Experiment and the Numerical Simulation at t/T=0.4

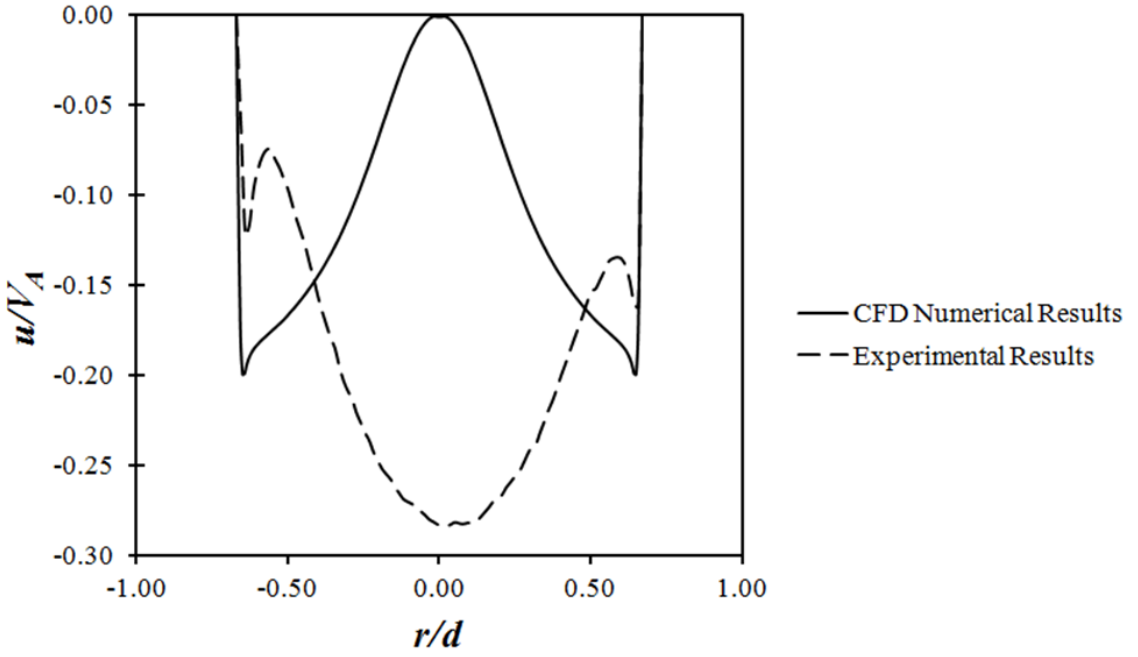

Figure G.26 Velocity Profile Across the Shroud's Diameter at x/d=1.75 for the Experiment and the Numerical Simulation at t/T=0.6

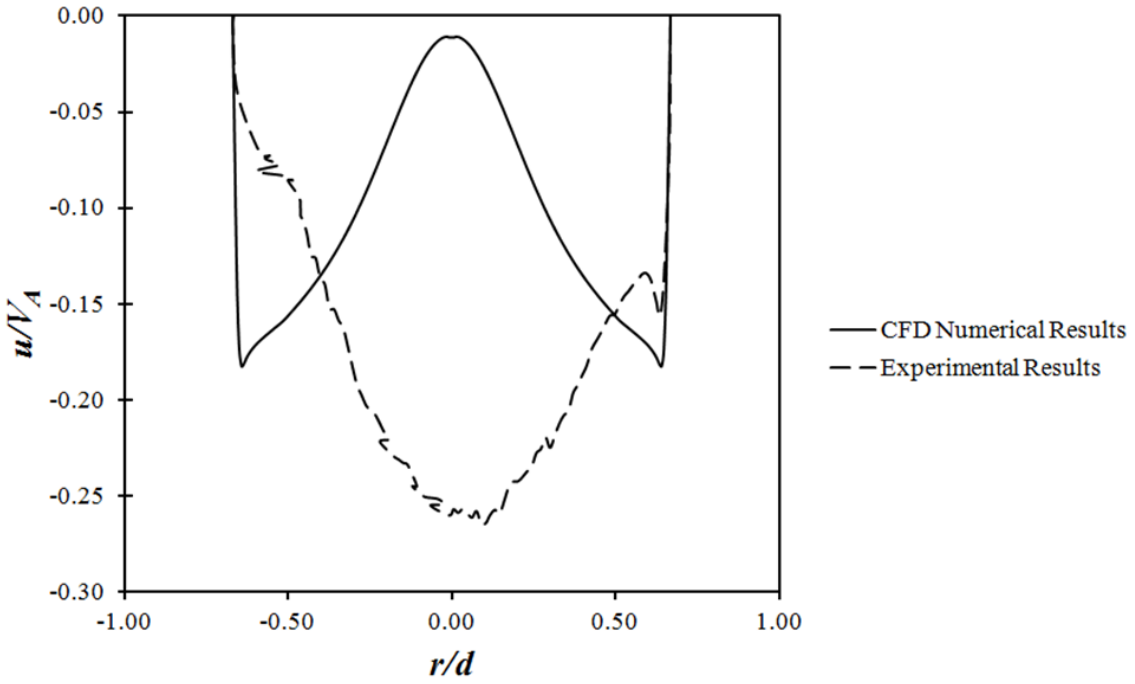

Figure G.27 Velocity Profile Across the Shroud's Diameter at x/d=1.75 for the Experiment and the Numerical Simulation at t/T=0.7

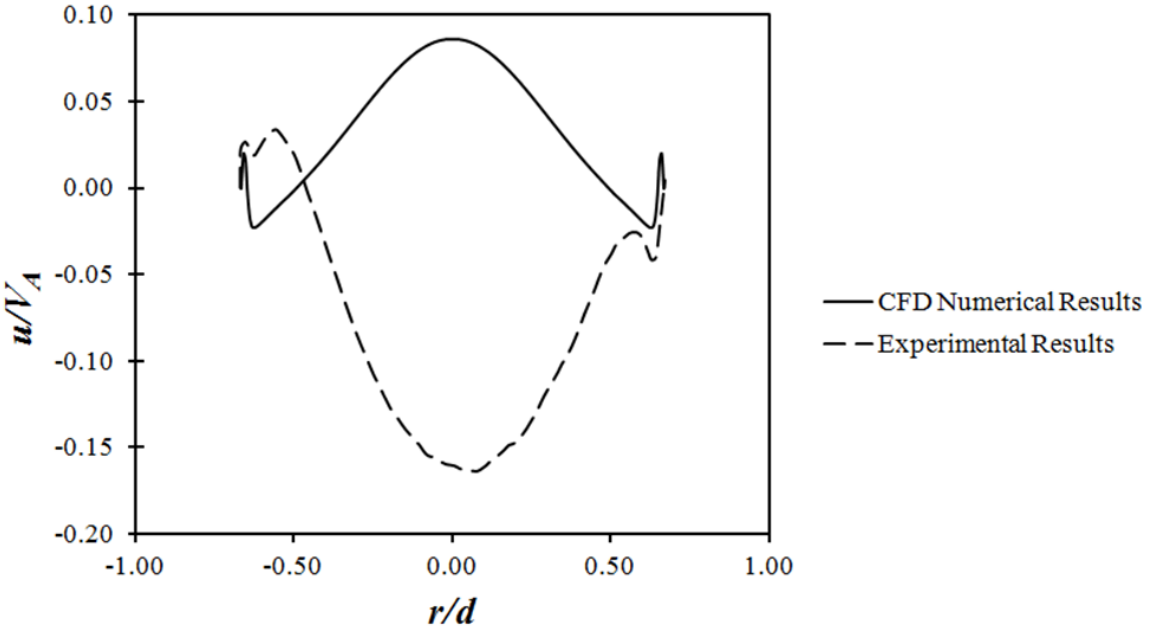

Figure G.28 Velocity Profile Across the Shroud's Diameter at x/d=1.75 for the Experiment and the Numerical Simulation at t/T=0.9

REFERENCES

[1] Gol'dshtik, M. A., and Yavorskii, N. I., 1986, "On Submerged Jets," J. Appl. Math. Mech., **50**(4), pp. 438–445.

[2] Davidson, P., 2015, *Turbulence: An Introduction for Scientists and Engineers*, Oxford University Press.

[3] Hinze, J. O., 1972, "Turbulent Fluid and Particle Interaction- Keynote Lecture," *Proceedings of the International Symposium on Two-Phase Systems*, G. Hetsroni, S. Sideman, and J.P. Harnett, eds., Pergamon, pp. 433–452.

[4] Glezer, A., and Amitay, M., 2002, "Synthetic Jets," Annu. Rev. Fluid Mech., **34**, pp. 503–29.

[5] Garg, J., Arik, M., Weaver, S., Wetzel, T., and Saddoughi, S., 2005, "Meso Scale Pulsating Jets for Electronics Cooling," J. Electron. Packag., **127**(4), pp. 503–511.

[6] Rajaratnam, N., ed., 1976, "Chapter 8 Confined Jets," *Developments in Water Science*, Elsevier, pp. 148–183.

[7] James, R. D., Jacobs, J. W., and Glezer, A., 1996, "A Round Turbulent Jet Produced by an Oscillating Diaphragm," Phys. Fluids, **8**(9), pp. 2484–2495.

[8] Cater, J. E., and Soria, J., 2002, "The Evolution of Round Zero-Net-Mass-Flux Jets," J. Fluid Mech., **472**, pp. 167–200.

[9] Smith, B. L., and Glezer, A., 1998, "The Formation and Evolution of Synthetic Jets," Phys. Fluids, **10**(9), pp. 2281–2297.

[10] Holman, R., Utturkar, Y., Mittal, R., Smith, B. L., and Cattafesta, L., 2005, "Formation Criterion for Synthetic Jets," AIAA J., **43**(10), pp. 2110–2116.

[11] Greco, C. S., Cardone, G., and Soria, J., 2015, "Flow Field Characteristic of High Reynolds Impinging Zero-Net-Mass-Flux Jets," *10th Pacific Symposium on Flow Visualization and Image Processing*, Naples, Italy, p. 16.

[12] Smith, B. L., and Swift, G. W., 2003, "A Comparison between Synthetic Jets and Continuous Jets," Exp. Fluids, **34**(4), pp. 467–472.

[13] Xia, Z., and Luo, Z., 2007, "Physical Factors of Primary Jet Vectoring Control Using Synthetic Jet Actuators," Appl. Math. Mech., **28**(7), pp. 907–920.

[14] Amitay, M., Smith, D. R., Kibens, V., Parekh, D. E., and Glezer, A., 2001, "Aerodynamic Flow Control over an Unconventional Airfoil Using Synthetic Jet Actuators," AIAA J., **39**(3), pp. 361–370.

[15] Pavlova, A., and Amitay, M., 2006, "Electronic Cooling Using Synthetic Jet Impingement," J. Heat Transf., **128**(9), pp. 897–907.

[16] Arik, M., Petroski, J., Bar-Cohen, A., and Demiroglu, M., 2007, "Energy Efficiency of Low Form Factor Cooling Devices," *ASME 2007 International Mechanical Engineering Congress and Exposition*, Seattle, WA, United States, pp. 1347–1354.

[17] Eri, Q., Hong, L., Li, T., Wang, Q., and Wang, M., 2016, "Numerical Simulations of Mixing Enhancement in Subsonic Jet Using High-Momentum Synthetic Jets," J. Propuls. Power, **32**(5), pp. 1095–1103.

[18] Smith, B., and Glezer, A., 2002, "Jet Vectoring Using Synthetic Jets," J Fluid Mech, **458**, pp. 1–34.

[19] Vermeulen, P., Ramesh, V., Meng, G., Miller, D., and Domel, N., 2004, "Air Ejector Pumping Enhancement Through Pulsing Primary Flow," *2nd AIAA Flow*

Control Conference, American Institute of Aeronautics and Astronautics, Portland, Oregon.

[20] Lin, F., 2009, "Numerical Investigation of Synthetic Jet Ejector (SJE) Performance," M.A.Sc., University of Windsor (Canada).

[21] Wu, K., Park, J., and Breuer, K., 2003, "Dynamics of Synthetic Jet Arrays for Closed-Loop Flow Control," *33rd AIAA Fluid Dynamics Conference and Exhibit*, p. 4257.

[22] Kral, L. D., Donovan, J. F., Gain, A. B., and Cary, A. W., 1997, "Numerical Simulation of Synthetic Jet Actuators," *28th AIAA Fluid Dynamics Conference, 4th AIAA Shear Flow Control Conference*, Snowmass Village, CO, USA., p. 15.

[23] Rizzetta, D. P., Visbal, M. R., and Stanek, M. J., 1999, "Numerical Investigation of Synthetic-Jet Flowfields," Am. Inst. Aeronaut. Astronaut. AIAA, **37**, pp. 919–927.

[24] Mallinson, S. G., Hong, G., and Reizes, J. A., 1999, "Some Characteristics of Synthetic Jets," *30th AIAA Fluid Dynamics Conference*, AIAA, Norfolk, VA, USA., p. 11.

[25] Utturkar, Y., Holman, R., Mittal, R., Carrol, B., Sheplak, M., and Cattafesta, L., 2003, "A Jet Formation Criterion for Synthetic Jet Actuators," Am. Inst. Aeronaut. Astronaut. AIAA, p. 10.

[26] Soria, J., and Cater, J., 2002, "The Evolution of Round Zero-Net-Mass-Flux Jets," J Fluid Mech, **472**, pp. 167–200.

[27] Didden, N., 1979, "On the Formation of Vortex Rings: Rolling-up and Production of Circulation," J. Appl. Math. Phys. ZAMP, **30**, pp. 101–116.

[28] Rampunggoon, P., 2001, “Interaction of a Synthetic Jet with a Flat Plate Boundary Layer,” Ph.D. Dissertation, Univerisity of Florida.

[29] Murugan, T., Deyashi, M., Dey, S., Rana, S. C., and Chatterjee, P. K., 2016, “Recent Developments on Synthetic Jets,” Def. Sci. J., **66**(5), pp. 489–498.

[30] Mohseni, K., and Mittal, R., 2014, *Synthetic Jets: Fundamentals and Applications*, CRC Press.

[31] Ricou, F. P., and Spalding, D. B., 1961, “Measurements of Entrainment by Axisymmetrical Turbulent Jets,” J. Fluid Mech., **11**(1), pp. 21–32.

[32] Hill, B. J., 1972, “Measurement of Local Entrainment Rate in the Initial Region of Axisymmetric Turbulent Air Jets,” J. Fluid Mech., **51**(4), pp. 773–779.

[33] Vermeulen, P. J., Rainville, P., and Ramesh, V., 1991, “Measurements of the Entrainment Coefficient of Acoustically Pulsed Axisymmetric Free Air Jets,” *ASME 1991 International Gas Turbine and Aeroengine Congress and Exposition*, American Society of Mechanical Engineers, Orlando, Florida, USA.

[34] Rayleigh, L., 1883, “The Form of Standing Waves on the Surface of Running Water,” Proc. Lond. Math. Soc., **s1-15**(1), pp. 69–78.

[35] Rayleigh, L., and Strutt, J., 1896, *The Theory of Sound*, Macmillan.

[36] Eckart, C., 1948, “Vortices and Streams Caused by Sound Waves,” Phys. Rev., **73**(1), pp. 68–76.

[37] Ingard, U., and Labate, S., “Acoustic Circulation Effects and the Nonlinear Impedance of Orifices,” J. Acoust. Soc. Am., **22**(2).

[38] Coe, D. J., Allen, M. G., Trautman, M. A., and Glezer, A., 1994, "Micromachined Jets for Manipulation of Macro Flows," *Solid-State Sensor and Actuator Workshop*, Transducers Research Foundation, Inc. Hilton Head, pp. 13–16.

[39] James, R., Jacobs, J., and Glezer, A., 1996, "A Round Turbulent Jet Produced By an Oscillating Diaphragm," Phys. Fluids, **8**(9).

[40] Shuster, J. M., and Smith, D. R., 2007, "Experimental Study of the Formation and Scaling of a Round Synthetic Jet," Phys. Fluids, **19**(4), p. 045109.

[41] Agrawal, A., and Verma, G., 2008, "Similarity Analysis of Planar and Axisymmetric Turbulent Synthetic Jets," Int. J. Heat Mass Transf., **51**(25–26), pp. 6194–6198.

[42] Goldstein, D., and Lee, C., 2002, "Two-Dimensional Synthetic Jet Simulation," Am. Inst. Aeronaut. Astronaut. AIAA, **40**(3), pp. 510–516.

[43] Utturkar, Y., Mittal, R., Rampungoon, P., and Cattafesta, L., 2002, "Sensitiviy of Synthetic Jets to the Design of the Jet Cavity," *40th AIAA Aerospace Sciences Meeting and Exhibit*, Reno, NV, USA.

[44] Fugal, S. R., 2004, "A Numerical Study of Oscillating Flow Through a Sudden Expansion," M.A.Sc. Thesis, Utah State University.

[45] Ravi, B. R., and Mittal, R., 2006, "Numerical Study of Large Aspect-Ratio Synthetic Jets," Am. Inst. Aeronaut. Astronaut. AIAA, p. 14.

[46] Jagannatha, D., Narayanaswamy, R., and Chandratilleke, T. T., 2009, "Analysis of a Synthetic Jet-Based Electronic Cooling Module," Numer. Heat Transf. Part Appl., **56**(3), pp. 211–229.

[47] Didden, N., 1979, “On the Formation of Vortex Rings: Rolling-up and Production of Circulation,” Z. Für Angew. Math. Phys. ZAMP, **30**(1), pp. 101–116.

[48] Allen, J. J., and Auvity, B., 2002, “Interaction of a Vortex Ring with a Piston Vortex,” J. Fluid Mech., **465**, pp. 353–378.

[49] Vermeulen, P. J., Ramesh, V., Meng, G., C., Miller, D. N., and Domel, N., 2005, *Air Ejector Pumping Enhancement through Pulsing Primary Flow*, F49620-02-1–0131, Air Force Office of Scientific Research Contract # F49620-02-1-0131, Dayton, OH.

[50] Meng, G. C., 2005, “Air Ejector Pumping Enhancement Using Pulsed Primary Flow,” Ph.D. Dissertation, University of Calgary.

[51] Lin, F., and Rankin, G. W., 2011, “An Efficient Numerical Model to Determine Synthetic Jet Ejector Performance,” AIP Conf. Proc., **1389**(1), pp. 139–142.

[52] Mahalingam, R., and Glezer, A., 2005, “Design and Thermal Characteristics of a Synthetic Jet Ejector Heat Sink,” J. Electron. Packag., **127**(2), pp. 172–177.

[53] Mahalingam, R., and Glezer, A., 2005, “Forced Air Cooling with Synthetic Jet Ejectors,” *Proceedings of the ASME/Pacific Rim Technical Conference and Exhibition on Integration and Packaging of MEMS, NEMS, and Electronic Systems: Advances in Electronic Packaging*, San Francisco, California, USA, pp. 59–64.

[54] Mahalingam, R., Heffington, S., Jones, L., and Schwickert, M., 2006, “Newisys Server Processor Cooling Augmentation Using Synthetic Jet Ejectors,” *Thermal and Thermomechanical Proceedings 10th Intersociety Conference on Phenomena in Electronics Systems, 2006. ITHERM 2006.*, pp. 705–709.

[55] Di Cicca, G., and Iuso, G., 2007, "On the near Field of an Axisymmetric Synthetic Jet," Fluid Dyn. Res., **39**(9–10), p. 673.

[56] Broučková, Z., and Trávníček, Z., 2015, "Visualization Study of Hybrid Synthetic Jets," J. Vis., **18**(4), pp. 581–593.

[57] Organ, A. J., and Finkelstein, T., 2009, "Air Engines: The History, Science, and Reality of the Perfect Engine," ASME N. Y.

[58] Mabie, Hamilton. H., 1987, *Mechanisms and Dynamics of Machinery*, Wiley.

[59] Lee, G. J., Kim, J., and Lee, T. S., 2014, "The Rolling Scotch Yoke Mechanism Applied to a Small Air Compressor for Oil-Free Operations," Int. J. Precis. Eng. Manuf., **15**(1), pp. 97–103.

[60] Alaswad, Z., 2017, *Experimental Facility for Synthetic Jet Ejector Study, Internal Report*, University of Windsor, Windsor, Ontario.

[61] "Potters Industries LLC," Cary Co. [Online]. Available: https://www.thecarycompany.com/raw-materials/principals/potters. [Accessed: 10-Apr-2019].

[62] Huang, H., Dabiri, D., and Gharib, M., 1997, "On Errors of Digital Particle Image Velocimetry," Meas. Sci. Technol., **8**(12), p. 1427.

[63] Thielicke, W., and Stamhuis, E. J., 2014, "PIVlab-towards User-Friendly, Affordable and Accurate Digital Particle Image Velocimetry in MATLAB," J. Open Res. Softw., **2**.

[64] Raffel, M., Willert, C. E., Scarano, F., Kähler, C. J., Wereley, S. T., and Kompenhans, J., 2018, *Particle Image Velocimetry: A Practical Guide*, Springer.

[65] Keane, R. D., and Adrian, R. J., 1990, "Optimization of Particle Image Velocimeters. I. Double Pulsed Systems," Meas. Sci. Technol., **1**(11), p. 1202.

[66] Coleman, H. W., and Steele, W. G., 2009, "Errors and Uncertainties in a Measured Variable," Exp. Valid. Uncertain. Anal. Eng. 3rd Ed John Wiley Sons Hoboken NJ USA, pp. 29–60.

[67] Willert, C. E., and Gharib, M., 1991, "Digital Particle Image Velocimetry," Exp. Fluids, **10**(4), pp. 181–193.

[68] Prasad, A. K., Adrian, R. J., Landreth, C. C., and Offutt, P. W., 1992, "Effect of Resolution on the Speed and Accuracy of Particle Image Velocimetry Interrogation," Exp. Fluids, **13**(2–3), pp. 105–116.

[69] Forliti, D. J., Strykowski, P. J., and Debatin, K., 2000, "Bias and Precision Errors of Digital Particle Image Velocimetry," Exp. Fluids, **28**(5), pp. 436–447.

[70] Sciacchitano, A., Neal, D. R., Smith, B. L., Warner, S. O., Vlachos, P. P., Wieneke, B., and Scarano, F., 2015, "Collaborative Framework for PIV Uncertainty Quantification: Comparative Assessment of Methods," Meas. Sci. Technol., **26**(7), p. 074004.

[71] Visualization Society of Japan, 2002, *Handbook of Particle Image Velocimetry*, Morikita.

[72] Nishio, S., Okamoto, K., Kobayashi, T., and Saga, T., 1999, "Evaluation of System Performance and Uncertainty Analysis of PIV (PIV-STD Project)," *Proceedings of the 3rd International Workshop on Particle Image Velocimetry,* Kobe University, Kobe, Japan, pp. 465-470.

[73] ITTC, 2008, "Uncertainty Analysis: Particle Image Velocimetry," *Recommended Procedures and Guidelines; Uncertainty Analysis - An Example for PIV Measurement Specialist Committee on Uncertainty Analysis, 25th International Towing Tank Conference (ITTC)*, Leipzig, Germany.

[74] ANSYS, I., 2015, "Ansys R17. 2 Help (Manual)," Ansys Corp [Online]. Available: http://research.me.udel.edu/~lwang/teaching/MEx81/ansys56manual.pdf. [Accessed: 10-Jun-2019].

[75] Menter, F. R., Kuntz, M., and Langtry, R., 2003, "Ten Years of Industrial Experience with the SST Turbulence Model," Turbul. Heat Mass Transf., **4**(1), pp. 625–632.

[76] Gatski, T., and Rumsey, C., 2004, "CFD Validation of Synthetic Jets and Turbulent Separation Control," *Langley Research Center Workshop, Williamsburg, VA, USA, March*, pp. 29–31.

[77] ANSYS, I., 2010, "ANSYS FLUENT 13.0 User's Guide" [Online]. Available: http://www.afs.enea.it/project/neptunius/docs/fluent/html/ug/main_pre.htm. [Accessed: 10-Jun-2019].

[78] Versteeg, H. K., and Malalasekera, W., 2007, *An Introduction to Computational Fluid Dynamics: The Finite Volume Method*, Pearson education.

[79] Techet, A., and Epps, B., "Derivation of Added Mass around a Sphere" [Online]. Available: http://web.mit.edu/2.016/www/handouts/Added_Mass_Derivation_050916.pdf.

[80] TSI, "TSI Insight 4G Software" [Online]. Available: https://www.tsi.com/products/_product-accessories/insight-4g%E2%84%A2-global-imaging,-acquisition,-analysis-and-display-software.aspx. [Accessed: 21-May-2019].

[81] Okamoto, K., Nishio, S., Saga, T., and Kobayashi, T., 2000, "Standard Images for Particle-Image Velocimetry," Meas. Sci. Technol., **11**(6), p. 685.

[82] Gutmark, E., and Wygnanski, I., 1976, "The Planar Turbulent Jet," J. Fluid Mech., **73**(3), pp. 465–495.

[83] Ting, D., 2016, *Basics of Engineering Turbulence*, Academic Press.

[84] Rodi, W., 1991, "Experience with Two-Layer Models Combining the k-Epsilon Model with a One-Equation Model near the Wall," *29th Aerospace Sciences Meeting*, American Institute of Aeronautics and Astronautics, Reno, NV, USA.

[85] Lam, C. K. G., and Bremhorst, K., 1981, "A Modified Form of the K-ε Model for Predicting Wall Turbulence," J. Fluids Eng., **103**(3), pp. 456–460.

[86] Wilcox, D. C., 1998, *Turbulence Modeling for CFD*, DCW Industries, Inc., La Canada, California.

[87] Wilcox, D., 1993, "Comparison of Two-Equation Turbulence Models for Boundary Layers with Pressure Gradient," AIAA J., **31**(8), pp. 1414–1421.

[88] Chang, K., and Chen, S., 1993, "Development of a Hybrid K-ε Turbulence Model for Swirling Recirculating Flows under Moderate to Strong Swirl Intensities," Int. J. Numer. Methods Fluids, **16**(5), pp. 421–443.

[89] Menter, F. R., 1992, *Improved Two-Equation k-Omega Turbulence Models for Aerodynamic Flows*, NASA-TM-103975, NASA, CA, USA.

[90] Versteeg, H. K., and Malalasekera, W., 2007, *An Introduction to Computational Fluid Dynamics: The Finite Volume Method*, Pearson education.

[91] Hanjalic, K., 2004, "Closure Models for Incompressible Turbulent Flows" [Online].Available: https://www.researchgate.net/file.PostFileLoader.html?assetKey=AS:273543839846420@1442229341759&id=53898c5fd039b1bd3a8b45c0. [Accessed: 10-Jun-2019].

[92] Wilcox, D., 1994, "Simulation of Transition with a Two-Equation Turbulence Model," AIAA J., **32**(2), pp. 247–255.

[93] "ANSYS FLUENT 12.0 Theory Guide" [Online]. Available: http://www.afs.enea.it/project/neptunius/docs/fluent/html/th/main_pre.htm. [Accessed: 04-May-2019].

VITA AUCTORIS

NAME:	Ziad Alaswad
PLACE OF BIRTH:	Kuwait City, Kuwait
YEAR OF BIRTH:	1994
EDUCATION:	Alnajat high school, Salmiya, Kuwait, 2012
	University of Windsor, B.Sc., Windsor, ON, 2017
	University of Windsor, M.Sc., Windsor, ON, 2019